NORTHEASTERN UNIVERSITY

Graduate School of Engineering

Thesis Title: Computational Model of Photothermal Microscopy in Tissue

Author: Jason M. Kellicker

Department: Electrical and Computer Engineering

Approved for Thesis Requirements of the Master of Science Degree:

Charles A DiMarzio — 19 Aug 2010

Thesis Adviser: Charles A. DiMarzio — Date

Gregory J Kowalski — 8/13/10

Thesis Adviser: Gregory J. Kowalski

(Department of Mechanical and Industrial Engineering — Date

8/13/10

Thesis Reader: Carey M. Rappaport — Date

Ali Abur — 8/19/10

Department Chair: — Date

Graduate School Notified of Acceptance:

Sara Wadia-Fascetti — 8/19/10

Director of the Graduate School of Engineering: Sara Wadia–Fascetti — Date

COMPUTATIONAL MODEL OF PHOTOTHERMAL MICROSCOPY IN TISSUE

A Thesis Presented

by

Jason M. Kellicker

to

The Department of Electrical and Computer Engineering

in partial fulfillment of the requirements

for the degree of

Master of Science

in the field of

Electrical Engineering

Northeastern University

Boston, Massachusetts

August 2010

Abstract

This research, through a rigorous optical, thermal and mechanical computational analysis, demonstrates the use of Photothermal Microscopy to tag light from the focus, and thereby improve contrast and depth of imaging limited by out–of–plane scatter.

The photothermal effect produced by the conversion of optical energy to heat within a dielectric medium provides a basis for investigation of the optical absorption and thermal characteristics of a sample. Through application of Photo-acoustic spectroscopy, measurements can be made of the acoustic pressure wave resulting from the absorption within the medium from a heating laser. This technique is commonly employed in biomedical imaging, however, it lacks the resolution necessary to image human skin at a cellular level.

To improve the resolving power and achieve adequate depth, this research demonstrates, computationally, the implementation of a coherent confocal microscope into the photo-acoustic system. The high accuracy of the interferometer in the confocal microscope allows for detection of small changes in position of scattering particles within the skin. Information about the optical phase of the particles can be obtained from measurement of the Doppler shift from these displacements due to the thermoelastic expansion of the sample by the photothermal process. This technique resembles the Doppler Laser Radar, an inherent concept implemented into the coherent confocal microscope.

The results of the computational analysis of this research are compared to analytical and theoretical expectations and are found to be in good agreement.

Acknowledgements

I would like to express my sincere gratitude to Professor Charles A. DiMarzio for his continuous encouragement, support and inspiration, not only throughout this research, but throughout my graduate career. As an advisor, Professor DiMarzio has given the greatly appreciated and necessary guidance and patience to make this accomplishment possible.

I would like to extend a great thanks to Professor Gregory J. Kowalski for the professional help and understanding he provided regarding the mechanical and thermal aspects of this research. Additionally, Professor Kowalski provided support and guidance as a committee member for this paper.

Additionally, I would like to thank Professor Carey M. Rappaport for serving as a member of committee for this paper.

Finally, I would like to thank my parents William and Denise Kellicker, my sibling, Michelle Kellicker, my good friend Professor David B. Massey, and Stacia Langille for all of their moral support, encouragement and inspiration through the rigors of this project.

Nomenclature

A	Area.
A_p	Amplitude of a Scattering Particle, p.
A_s	Amplitude of a Scattering Particle.
$\mathbf{B}$	Magnetic Flux Density.
CND	Conduction Array.
c	Speed of Light in Vacuum.
c_p	Specific Heat of the Material.
c_x	Center of The Irradiated Area On Sample Surface for x.
c_y	Center of The Irradiated Area On Sample Surface for y.
c_z	Center of The Irradiated Area On Sample Surface for z.
$\mathbf{c_1}$	Center Position of Node Containing Scattering Particle.
$\mathbf{c_2}$	Center Position of Nearest Adjacent Node to the Node Containing Scattering Particle.
d_0	Beam Diameter.
$\mathbf{D}$	Electric Displacement.
E_m	Young's Modulus.
E_s	Signal Field.

E_t Transmitted Field.

E^*_{LO} Back Propagated Local Oscillator (BPLO) Field.

$\mathbf{E}$ Electric Field.

e Electron Charge.

F_i Indentation Force.

f Focal Length of Input Lens.

f_d Doppler Frequency.

f_l Corrected Focal Length.

f_o Frequency.

$\mathbf{H}$ Magnetic Field.

h Convective Coefficient.

$\hbar$ Planck's Constant.

I Irradiance.

$ICONN$ Interconnection Array.

I_0 Peak Irradiance.

I_B Black Body Emitted Intensity.

I_{abs} Absorbed Intensity.

I_g Irradiance at Input Lens to System.

I_{emitt} Emitted Intensity.

I_{mix} Mixing Irradiance.

$I_{scatt_{in}}$ Internally Scattered Intensity.

$I_{scatt_{out}}$ Outward Scattered Intensity.

i Current.

i_{exp} Expected Current.

$\mathbf{J}$ Current Density.

K_t Thermal Conductivity of the Material.

K_{air} Conductivity of Air.

k Wave Number.

$\mathbf{k}$ Propagation Vector.

L Sample Length in the z Direction.

L_c Length of the Sample.

L_x Length of the Sample in the x Direction.

L_y Length of the Sample in the y Direction.

L_z Length of the Sample in the z Direction.

ℓ Length Along the Ray.

N Node.

NA Numerical Aperture.

Nu Nusselt Number.

n Index of Refraction.

n_0 Index of Refraction in Air.

n_1 Index of Refraction of Medium 1.

n_2 Index of Refraction of Medium 2.

$\bar{n}_1$ Linear Index of Refraction of Material.

$\bar{n}_2$ Nonlinear Index of Refraction of Material.

OPL Optical Path Length.

OZ *Optical Zone*

P Power.

PPL Physical Path Length.

P_{LO} Power from the Local Oscillator Beam.

P_{mix} Mixing Power at the Detector.

P_{sig} Power Received at the Detector.

P_t Power Delivered to the Target.

p Pressure Within the Material.

$\mathbf{p}$ Scattering Particle Position Vector.

Q Normalized Absorption.

QVL Volumetric Absorption.

q Heat Flux Vector.

q_0'' Incident Heat Flux.

q_{abs}'' Absorbed Radiation per Unit Volume.

q_{BR}'' Back Reflected Energy.

q_{cond} Energy Conducted.

q_{conv} Energy Convected.

q_{plane} Energy Transfer to a Plane Surface.

q_s'' Surface Heat Flux.

q_{trans}'' Transmitted Energy.

q_{surf} Energy Transfer to a Surface.

$R(z)$ radius of Curvature of Gaussian Beam.

r Radial Distance.

r' Radial Distance Between Nodes for Thermoelastic Potential.

r_1 Radial Component of the Transmitted Field.

r_2 Radial Component of the Signal Field at the Detector.

r_{dist} Distance to Node Center from Scattering Particle.

r_{eff} Effective Radius of a Sphere Representing a Node Volume.

r_{ix1} Location in the x Direction to Maximum Corner of the Irradiated Area.

r_{ix2} Location in the x Direction to Minimum Corner of the Irradiated Area.

r_{iy1} Location in the y Direction to Maximum Corner of the Irradiated Area.

r_{iy2} Location in the y Direction to Minimum Corner of the Irradiated Area.

r_{iz1} Location in the z Direction to Maximum Corner of the Irradiated Area.

r_{iz2} Location in the z Direction to Minimum Corner of the Irradiated Area.

$\mathbf{r}$ Position Vector.

$\mathbf{r_1}$ Position of Ray Entrance into Node Containing Scattering Particle.

$\mathbf{r_2}$ Position of Ray Exit from Node Containing Scattering Particle.

S Signal from Sum of Scattering Particles.

S_p Signal from a Scattering Particle, p.

s A Surface.

s_p Complex Scattering Parameter.

T Temperature.

T_0 Ambient Temperature.

T^F Future Temporal Temperature Value.

T^P Present Temporal Temperature Value.

$\bar{T}$ Normalized Temperature.

T_{ch} Characteristic Temperature.

TE Transverse Electric Mode.

TM Transverse Magnetic Mode.

t Time.

Δt Critical Time Step.

$\bar{t}$ Normalized Time.

t_p Pulse Duration of Laser.

u Integrated Nodal Displacement in the x Direction.

V Volume.

v Integrated Nodal Displacement in the y Direction.

v_0 Specific Volume of the Material, Specific Case.

$v_{parallel}$ Parallel Velocity Component.

v_{sp} Specific Volume of the Material, General Case.

$\mathbf{v}$ Velocity Vector.

w Integrated Nodal Displacement in the z Direction.

Δx Node length in the x direction.

δx Local Nodal Displacement in the x Direction.

$\bar{x}$ Normalized x Direction Parameter.

Δy Node length in the y direction.

δy Local Nodal Displacement in the y Direction.

$\bar{y}$ Normalized y Direction Parameter.

Δz Node length in the z direction.

δz Local Nodal Displacement in the z Direction.

$\bar{z}$ Normalized z Direction Parameter.

Z_R Rayleigh Length.

$zlsl$ Distance from the Input Lens to the Sample.

$*$ Represents the Complex Conjugate Notation.

Greek Letters

α Absorption Coefficient of the Material.

α_0 Linear Absorption Coefficient of Material.

α_2 Nonlinear Absorption Coefficient of Material.

α_r Absorption Coefficient.

α_s Distribution of Randomly Scattering Particles.

α_s Scattering Coefficient.

α_λ Ratio of Absorbed Energy to Absorbed Black Body Energy.

β Coefficient of Isobaric Volume Expansion.

ϵ_0 Electrical Permittivity in Free Space.

ϵ Electrical Permittivity in Medium.

ε Complete Strain, Normal and Shear.

ε_λ Ratio of Emitted Energy to Emitted Black Body Energy.

Γ Field Reflection Coefficient.

Γ_I Irradiance Reflection Coefficient.

γ Shear Strains.

γ_{eff} Quantum Efficiency.

κ Isothermal Compressibility Factor.

κ_{ext} Extinction Coefficient.

λ Wavelength.

$\bar{\lambda}$ Mean Wavelength.

η Impedance of the Medium.

θ Half Angle Formed by the Objective.

θ_1 Angle of Incidence to Medium 1.

θ_2 Angle of Incidence to Medium 2.

θ_c Complex Angle of Incidence.

Ψ Thermoelastic Potential.

ψ Optical Phase.

ρ Density of the Material.

ρ_i Current Responsivity.

ρ_p Charge Density.

σ Complete Stress, Normal and Shear.

σ_{sb} Stefan-Boltzman Constant.

τ Shear Stresses.

τ_r Relaxation Time.

μ_0 Magnetic Permeability in Free Space.

μ Magnetic Permeability in Medium.

ν Poisson's Ratio.

Ω Steradian Angle.

ω_0 Gaussian Beam Radius at the Focus.

$\omega(z)$ Gaussian Beam Radius at Distance z from the Focus.

$\hat{\chi}$ Direction Cosine term for x, y and z.

Contents

Abstract **iv**

Acknowledgements **v**

Nomenclature **vi**

1 Introduction **1**

1.1 Photo-acoustic Spectroscopy 3

1.2 Optical Coherence Tomography 6

1.3 Confocal Microscopy 9

1.4 Opto-Photo-Thermo-Elastic Displacement 14

2 Thermal Displacement Simulation **16**

2.1 Pre-processor 17

2.2 Model Geometry 21

2.3 Thermal Transport Models 23

2.3.1 Parabolic One Step Model 25

2.3.2 Hyperbolic One Step 32

2.3.3 Parabolic One Step Model Verification 33

2.4 Radiation Model 38

2.5 Index of Refraction 47

2.6 Refraction and Raytrace Model 51

2.7 Boundary Conditions 57

3 Phase Amplitude Analysis **62**

3.1 Thermal Stress and Displacement 64

3.1.1 Discussion of Thermal Stress and the Young's Modulus 65

3.1.2 Thermal Stress Calculation 69

3.1.3 Thermal Displacement 73

3.2 Coherent Detection 77

3.2.1 Optical Quadrature 80

3.2.2 Doppler Laser Radar 86

3.3 Development 95

3.3.1 Displacement Interpolation 98

3.3.2 Phase Interpolation 101

3.3.2.1 Displacement–Dependent Optical Phase 102

3.3.2.2 Refractive–Index–Dependent Optical Phase 104

4 Results **110**

4.1 Comparison to Theoretical Assumptions. 111

4.2 Operational Parameters. 115

4.3 Optical Path Length Measurement. 116

4.4 Localization Discussion. 118

5 Conclusions and Future Research **122**

A Pre-processor File Definitions **124**

Bibliography **136**

List of Figures

1.1 Light in Tissue. Light entering tissue can be refracted, reflected, scattered and absorbed. 6

1.2 Layout for Optical Coherence Tomography. 8

1.3 Example of the Basic Layout for a Confocal Microscope. 10

1.4 Layout for a Scanning Confocal Microscope. 11

1.5 Layout for a Coherent Confocal Microscope Using a Michelson Interferometer. 13

1.6 Photothermal Microscope Using a Quadrature Coherent Confocal Microscope. 15

2.1 Flow Diagram of the Code with Emphasis on the Pre-Processor. . . . 19

2.2 Model Geometry. The irradiated area is with respect to this research on the positive $x - y$ face. 22

2.3 Flow Chart for the Predictor-Corrector Algorithm 31

2.4 Comparison of the Instantaneous Transmittance Over Time of the POS and HOS Models. 34

2.5 Flow Diagram of the Code with Emphasis on the Main-Processor. . . 39

2.6 Geometry of the Gaussian beam. 41

2.7 Geometry of Rays at $t = 0$ as They Propagate Through the Sample. . 46

2.8 Ray Refraction at Meduim. 47

2.9 Example of a Multilayer System with Incident, Reflected and Transmitted Fields for Layers with Different Temperatures. 55

2.10 Temperature Gradient for $z \approx 26$ μm at $t = 5$ μs. 58

2.11 Conduction and Convection at the $z = L_z$ Surface. 59

2.12 Temperature Gradient for $z \approx 26$ μm at $t = 5\mu$ s. Boundary condition at $z = 0$ is 4695.67 $\frac{\mathrm{W}}{\mathrm{m}^2 \cdot \mathrm{K}}$ and at $z = L_z$ is 56739.32 $\frac{\mathrm{W}}{\mathrm{m}^2 \cdot \mathrm{K}}$. 61

3.1 Flow Diagram of the Code with Emphasis on the Post–Processor. . . 63

3.2 Coherent Addition of two Waves Incident on a 45 Degree Dielectric Interface. 79

3.3 Coherent Addition of two Waves from the Same Source. 80

3.4 The Mach–Zhender Interferometer. 81

3.5 Optical Quadrature Detection. 85

3.6 Doppler Laser Radar. 86

3.7 Geometry for the Fresnel Integral. 90

3.8 Geometry for Equation 3.65, the Displacement Interpolation. 100

3.9 Geometry for Equation 3.68, the Direction Cosine, OPL Due to the Change in Index of Refraction and PPL Interpolation. 103

3.10 Ray 1 Path Through the System at $t = 25$ ns, and $t = 5$ μs at the Focus. 107

3.11 Ray 1 Path Through the System at $t = 25$ ns, and $t = 5$ μs for $z = L_z = 60$ μm 108

4.1 Theoretical Temperature Profile for the Fourier Conduction Law. . . 112

4.2 (A) Computational Temperature Gradient Over Time for Tissue. (B) Computational Index of Refraction Over Time for Tissue. 114

4.3 Real vs. Imaginary Plot for the $n\delta\ell$ Component of the Optical Phase. 118

4.4 Plot of the Unwrapped $n\delta\ell$ Component of the Optical Phase. 119

4.5 Plot of the Unwrapped $\ell\delta n$ Component of the Optical Phase. 120

List of Tables

2.1 "pre_txt" File Used for This Research. 18

2.2 Output Files Generated by the Pre-processor. 20

2.3 Conduction Array. n is the last node number of the system. 28

2.4 Linear Optical Material POS Verification Parameters 36

2.5 Analytical versus Numerical Values for a Material with Linear Absorption with no Reflections 37

2.6 Analytical versus Numerical Values for a Material with Linear Absorption and Reflections 38

2.7 Output Files Generated by the Main-Processor. 40

2.8 Gaussian Beam Parameters. 42

3.1 Output Files Generated by the Post–processor. 64

3.2 Relative Power Level Magnitudes of Laser Radar. 88

3.3 MATLAB Post–processor Files. 96

4.1 Parameters for the Theoretical Fourier Conduction Law Comparison. 112

Chapter 1

Introduction

The primary non–ionizing techniques employed in biomedical imaging are characterized by their abilities to resolve images within tissue with high contrast while achieving deep penetration within the tissue. Preserving these characteristics while delivering real-time, high-speed measurements drives the research in the biomedical industry.

The common techniques for imaging skin are Ultrasonography, Photo-acoustic Spectroscopy, Confocal Microscopy and Optical Coherence Tomography (OCT). Each has its advantages and drawbacks regarding penetration and resolution. Ultrasonography, commonly referred to as Ultrasound, offers penetration into the body of tens of centimeters, however, it suffers from poor resolution, 800 μm-80 μm, and a lack of contrast in soft tissue. High frequency ultrasound provides better resolution, but still has poor contrast. Photo-acoustic Spectroscopy provides penetration depths to 10 mm with resolution up to 80 μm. OCT achieves a penetration depth of 1 mm-2 mm with a resolution of $<$15 μm. Confocal Microscopy produces significantly better resolution ($<$3 μm), but has poor penetration resulting from clutter produced by light

scattered from outside the focal plane.

An improvement upon these techniques is to tag the light at the focal plane by utilizing a pulsed focused heating laser to cause tissue expansion. A coherent confocal microscope can then be implemented, acting as a laser vibrometer, to measure this expansion. This method of optical detection of changes in elastic displacement due to the photothermal process, introduced by Eliyahu *et al.* [1] for a simple case, will be evaluated in this research.

The following sections highlight the techniques pertinent to this research. Section 1.1 will discuss the method employed by Photo-acoustic Spectroscopy. Optical Coherence Tomography will be presented, Section 1.2. Confocal Microscopy will be explained in Section 1.3. Finally, Opto-Photo-Thermo-Elastic Displacement will be discussed in Section 1.4 to tie the previous sections together to form the basis for this research.

In the remaining chapters of this paper, a computational model will be defined which performs the rigorous optical, thermal and mechanical analysis necessary to gather information about the optical phase of scattering particles in tissue. Chapter 2 will develop the thermal model to calculate the displacement and optical path length, OPL, of the light scattered from particles through thermoelastic expansion. Chapter 3 will use the displacement and OPL information to calculate the optical phase change from each particle over each time step for the entire pulse duration of the heating source. The results of the computational analysis will be discussed in Chapter 4 and conclusions presented in Chapter 5 regarding the validity of Photothermal Microscopy as an imaging tool for biological tissue.

An abstract based on this work has been accepted for presentation to the Annual

Meeting of the Optical Society of America in October 2010 [2].

1.1 Photo-acoustic Spectroscopy

Utilization of Photo-thermal techniques allows for the measure of optical properties of materials through excitation of the electrons within the material by heating. This heat is generated by the absorption of the optical energy within the material. The photothermal effect then allows analysis of the absorption properties of the material through direct measure of the heat, or observation of the effect on the material resultant from the heating [3].

If a laser beam is focused within a material, the energy of the beam will be absorbed as heat and will diffuse through the material. This creates 2 conditions:

1. Thermal Confinement: All the energy is confined to within an *Optical Zone*.
2. Stress Confinement: All the mechanical stress resultant from thermoelastic expansion from the heating resides within an *Optical Zone*.

To elaborate upon these conditions, the *Optical Zone* must be defined as the illuminated volume. It is the depth at which the irradiance drops to a value of $\frac{1}{e}$ of the incident value [3] according to

$$OZ = \frac{1}{\alpha} \tag{1.1}$$

where α is the absorption coefficient of the material. A broad beam that has a

diameter at the focus, $d_0 > \frac{1}{\alpha}$, defines an *Optical Zone* according to

$$d_0 > \frac{1}{\alpha}. \tag{1.2}$$

Similarly, for a narrow beam,

$$d_0 < \frac{1}{\alpha}. \tag{1.3}$$

The energy from the laser within the sample will contribute to the heating, and over time this heating will diffuse through the sample. If the pulse duration of the laser, t_p is kept short,

$$t_p \leq \frac{OZ^2 \rho c_p}{K_t}, \tag{1.4}$$

the material will be in thermal confinement. In Equation 1.4, K_t is the thermal conductivity, ρ is the density and c_p is the specific heat. These parameters will be further explained in Chapter 2.

As the temperature increases in the material, stresses will be introduced due to thermoelastic expansion. The stress will dissipate through the medium according the velocity of sound, v_s, of that medium [3]. When the pulse duration fits the criterion

$$t_p < \frac{OZ}{v_s}, \tag{1.5}$$

the material is in stress confinement. The principles governing the thermal diffusion and stress are discussed in detail throughout this paper. This section serves only as an introduction to these concepts.

Photo-acoustic Spectroscopy, also referred to as Photo-Thermo-Acoustic (PTA) or Optoacoustic, employs the Photo-thermal techniques listed above to generate within the material an acoustic pressure wave resultant from the heating. This concept was first discovered by Alexander Graham Bell [4] while attempting to modulate a light beam with voice; he observed that selenium exposed to a modulated beam of light produced an audible signal.

Photo-acoustic Tomography (PAT) employs PTA through non-invasive, two-dimensional sections to produce *in vivo* imaging via ultrasound detection. The two-dimensional images can be captured and by using a time resolved technique with an array of ultrasound transducers, a three-dimensional image can be constructed [3]. This has been demonstrated on a rat's brain by Wang *et al.* [5].

The image obtained is based upon the absorbed rather then the scattered light which proves to be a problem in conventional imaging. However, the scattering in concert with the absorption determines the penetration depth of the heating laser and limits the effectiveness of PAT. Additionally, the attenuation of the propagating pressure wave limits the ability of the ultrasound detection system. As a result, PTA proves a useful non-invasive *in vivo* imaging technique for applications which do not require resolutions of a cellular level, such as skin does.

1.2 Optical Coherence Tomography

Optical Coherence Tomography, OCT, is an optical signal acquisition and processing method proven useful in imaging retina, lung, walls of coronary arteries, and other tissues to depths of near a millimeter. The technique uses interferometry with a light source that has a short coherence length [6]. Interferometry and interferometric techniques implemented in this research are explained in Section 3.2.2.

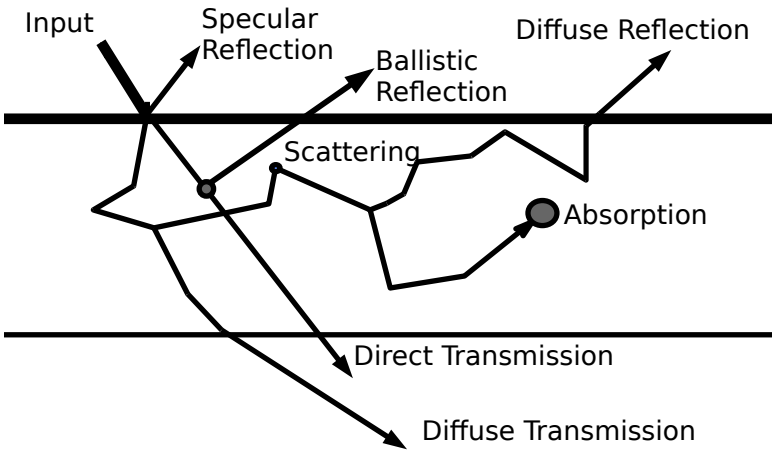

Figure 1.1: Light in Tissue. Light entering tissue can be refracted, reflected, scattered and absorbed.

Within biological tissue, light undergoes scattering, absorption and refraction in complicated ways as shown in Figure 1.1, due to heterogeneities with the tissue. When the heterogeneities are similar in size, or smaller then the wavelength of the incident light entering the tissue, they will cause scattering of the light over a large range of angles. This scattering is strong near the surface, but becomes increasingly weaker with depth into the tissue and can take place many times before the light exits the tissue as either diffuse transmission or diffuse reflection. These are shown in Figure 1.1.

The result of this is degradation to the high resolution promise that optics offers [6].

Ideal for this imaging technique is near infrared light since it will penetrate further then the highly diffusive visible, specifically red, light within tissue. Several centimeters of depth can be achieved with near infrared light. However, to preserve micrometer resolution, the imaging depth is restricted to not more then a millimeter.

The OCT provides a two dimensional map of the reflection of points within a sample by taking longitudinal scans for a series of lateral locations [3]. The optical lateral resolving power is proportional to

$$\frac{\lambda}{NA}, \tag{1.6}$$

where $NA = n \sin\theta$ is the numerical aperture, n is the index of refraction, λ is the wavelength of the source beam and θ, the cone of the half angle formed by the objective, shown in Figure 1.2, onto the sample.

The source beam is split by the beamsplitter into reference and signal beams. The reference beam is reflected by a mirror that can move along the longitudinal axis to provide the longitudinal scan of the sample. The signal beam is reflected back from the sample and the two beams are combined at the beamsplitter. The movement of the mirror produces interference modulation at the Doppler frequency, f_d, [3],

$$f_d = 2v_m\sqrt{\bar{\lambda}} \tag{1.7}$$

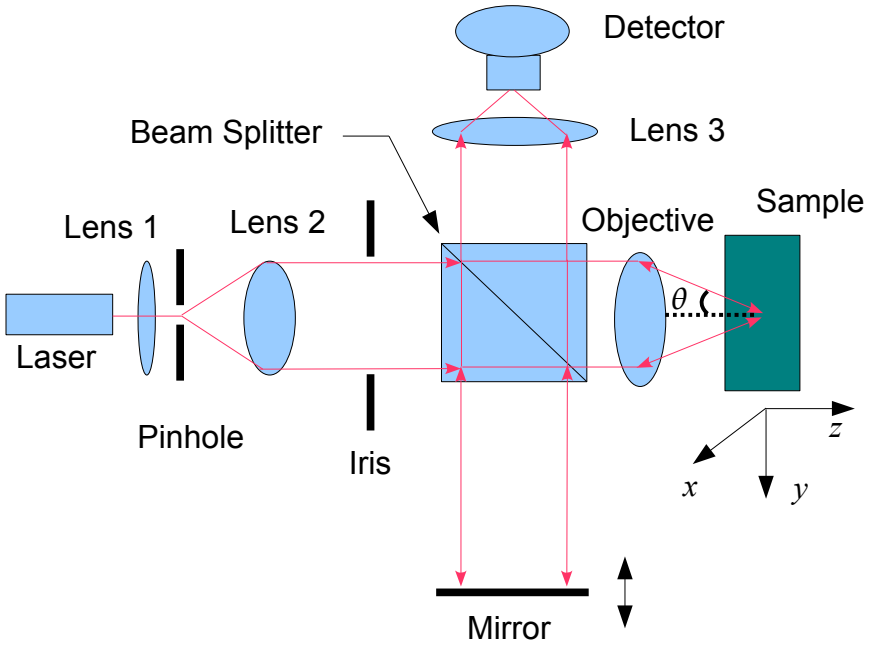

Figure 1.2: Layout for Optical Coherence Tomography.

where $\bar{\lambda}$ is the mean wavelength and v_m is the velocity of the mirror in the reference beam path.

The optical longitudinal resolving power, in contrast to the optical lateral resolution, is limited by the coherence length of the light source. The coherence length of the light is the distance the light can travel and still maintain a predictable optical phase. This is characterized by the coherence time; the length of time it takes to travel said distance. Physically, interference can only be achieved if the difference in path lengths in an interferometer is less than the coherence length.

In OCT only the lateral resolution can be determined by the NA of the objective lens. The longitudinal axis is scanned fast by moving the reference mirror which requires a long depth of field and a low NA. This limits the resolution of OCT. To improve upon this, the Confocal Microscope will be discussed in Section 1.3.

1.3 Confocal Microscopy

Confocal microscopy presents an imaging system that allows for a high-contrast image of a single plane within an optically transparent or translucent material. This is achieved by blocking the majority of the out-of-focus light that acts to degrade the quality of the image in conventional microscopy. The light source and detector are in optically conjugate focal planes, thus the name "confocal" [7].

The concept of the confocal microscope was first introduced by Minsky in 1957 [8] and later demonstrated by Eggar and Petran nearly ten years later. It wasn't until the late seventies that major breakthroughs occurred due to the advancement of lasers, electronic computers and image processing [3]. The basic concept of the confocal microscope is shown in Figure 1.3.

The point light source is usually a laser diverged by the pinhole, sometimes a lens, and focused onto the sample as a diffraction limited spot by the objective lens. The pinhole in front of the detector rejects the out-of-focus scattered light, shown by the colored, dashed lines, but allows the in-focus scattered light, solid black line, through. This eliminates the majority of out-of-focus scattered light from degrading the received signal. This allows the detector to comprise a single pixel light power detector such as a PIN photodiode, photomultiplier tube or an avalanche photodiode.

A two-dimensional image can be created by scanning the sample with the focused beam of light. This can be achieved be either moving the target with a motorized stage while the focused spot remains stationary, or by implementing optical elements, such as a scanning mirror to move along the target in one axis, and then the other. This is shown in Figure 1.4.

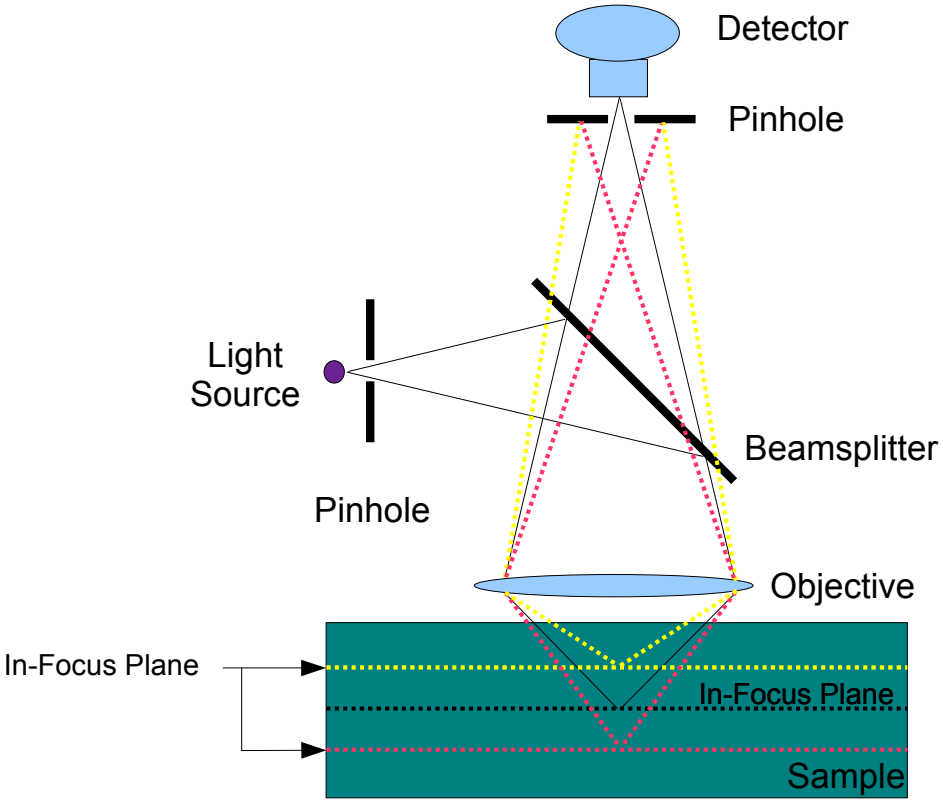

Figure 1.3: Example of the Basic Layout for a Confocal Microscope.

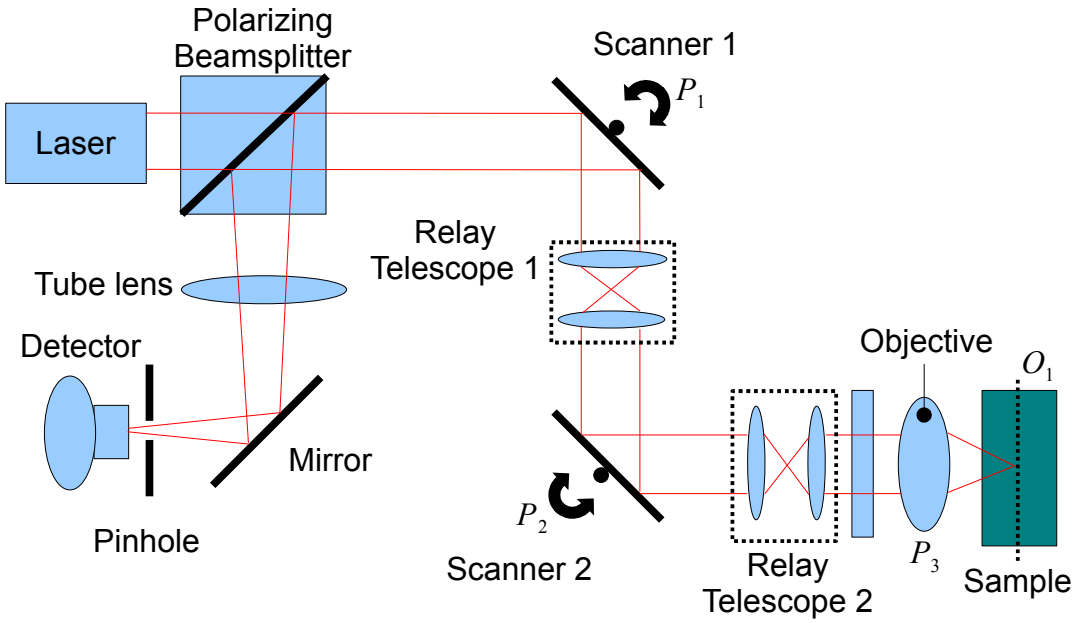

Figure 1.4: Layout for a Scanning Confocal Microscope.

This scanning confocal microscope incorporates two scanners to scan the focused spot in the object plane, O_1. Two optically conjugate pupil planes, P_1 and P_2, are produced by the two relay telescopes. These allow for two one-dimensional scanners to scan the beam in the inaccessible pupil plane of the objective [7].

The resolution of the confocal microscope in the optical lateral axis is determined similarly to that of the OCT by Equation 1.6. Differing from the OCT, the confocal microscope requires axial resolution. This is acheived, through approximation by Webb [9], by

$$\Delta z = 1.5\frac{\lambda n}{NA^2} \tag{1.8}$$

and is discussed further in Section 2.5. Webb also approximates the lateral resolution to be

$$\Delta x = \Delta y = 0.4\frac{\lambda}{NA}. \tag{1.9}$$

These equations demonstrate a need for a large numerical aperture to achieve high resolution in both directions.

The confocal microscope is capable of achieving penetration depths to nearly 350 μm in human skin *in vivo* with lateral resolution of 0.5-1.0 μm and axial resolution of 3-5 μm. This was achieved by developing a restraint for the forearm to laterally stabilize the imaging site to within ± 25 μm. The results showed good correlation to histology with near-infrared imaging of the epidermis, papillary dermis and superficial reticular dermis [10].

Expanding the functionality of the confocal microscope is the experimentation performed by Dwyer and DiMarzio [11] and Dwyer *et al.* [12] to develop a confocal theta line-scanning microscope. Scanning becomes much simpler since it is only required in one direction because detection is performed with a line detector. The results show a lateral resolution of 1.0 ± 0.1 μm and axial resolution of 1.7 ± 0.1 μm. While proving a much faster method, the theta-line scanning microscope is nonconfocal in the dimension parallel to the scanning line and in deeper, more strongly scattering epidermis, the resolution suffers greatly compared to point scanned images.

Confocal microscopy can be implemented similarly to OCT in a way that provides interferometric images of the tissue called Coherent Confocal Microscopy. Figure 1.5 shows the layout for a coherent confocal microscope using a Michelson Interferometer [3].

The source beam is split into a signal beam that is propagated to the sample and a local oscillator, LO, that is reflected from the second mirror. The two beams are recombined at the beamsplitter and the optical phase difference between them can be measured at the detector. The coherent confocal microscope relies on a coherence length that is longer then the optical path difference between the interferometer arms of the signal and LO paths.

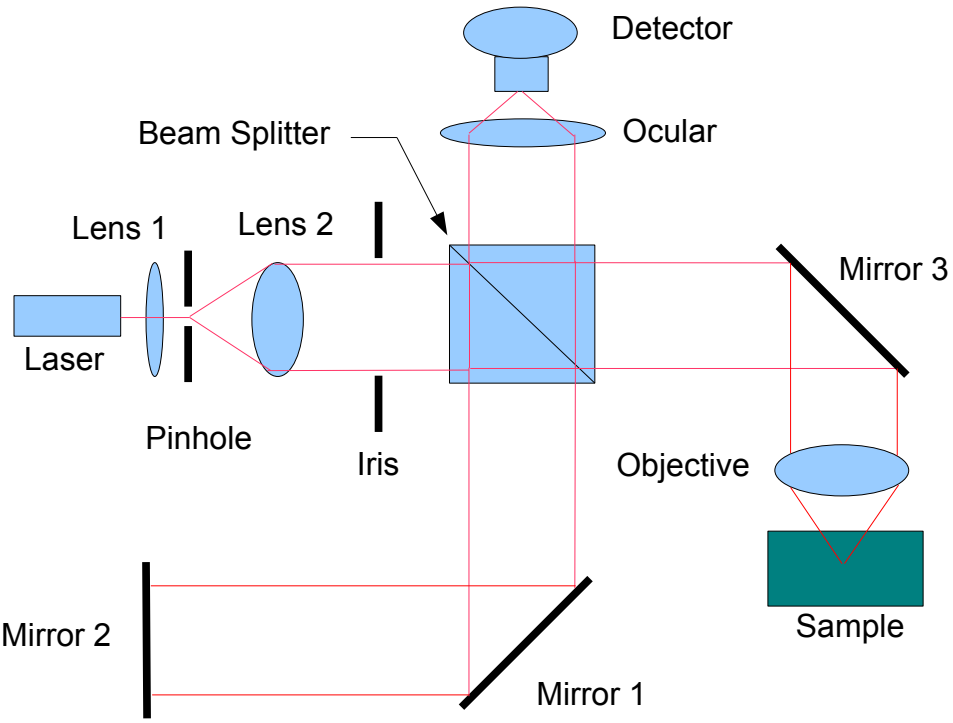

Figure 1.5: Layout for a Coherent Confocal Microscope Using a Michelson Interferometer.

Interferometry and coherence will be discussed in detail in Section 3.2.2 with respect to the Mach–Zehnder Interferometer [13, 14] and optical quadrature detection. These will be the proposed techniques implemented into the Photothermal Microscope.

1.4 Opto-Photo-Thermo-Elastic Displacement

Interferometric measurements have been proven to provide angstrom-level resolution spatially and nanosecond resolution temporally via photoacoustic tomography [15]. The drawback, however, is penetration depth within turbid media such as human skin. A possible solution is to combine the techniques mentioned in the previous sections to achieve both the necessary penetration depth and resolution within the skin to image to the blood vessel level.

First conceived by Nieva *et al.* [16] is the concept of using optical coherent detection of the Doppler shifts generated by an ultrasound field positioned at the optical focus of a confocal microscope to obtain information about the amplitude and phase of the scattered field. The photoacoustic signal is produced by a focused, pulsed heterodyne laser and detected by the confocal microscope. The results are presented analytically for scattering phantoms which showed promise for follow-up laboratory experimentation.

The experimentation was conducted by Eliyahu *et al.* [1] on Polyvinyl-Chloride Plastisol (PVCP) and was compared with an approximate analytical model. The PVCP phantoms were constructed with different absorbing coefficients and the results of the experimentation were in good qualitative agreement with the analytical results. Figure 1.6 shows a conceptual design for the photothermal microscope, similar to that used in the experimentation.

The optical elements will be discussed in Section 3.2.2 when the imaging techniques implemented into the development of this microscope are discussed.

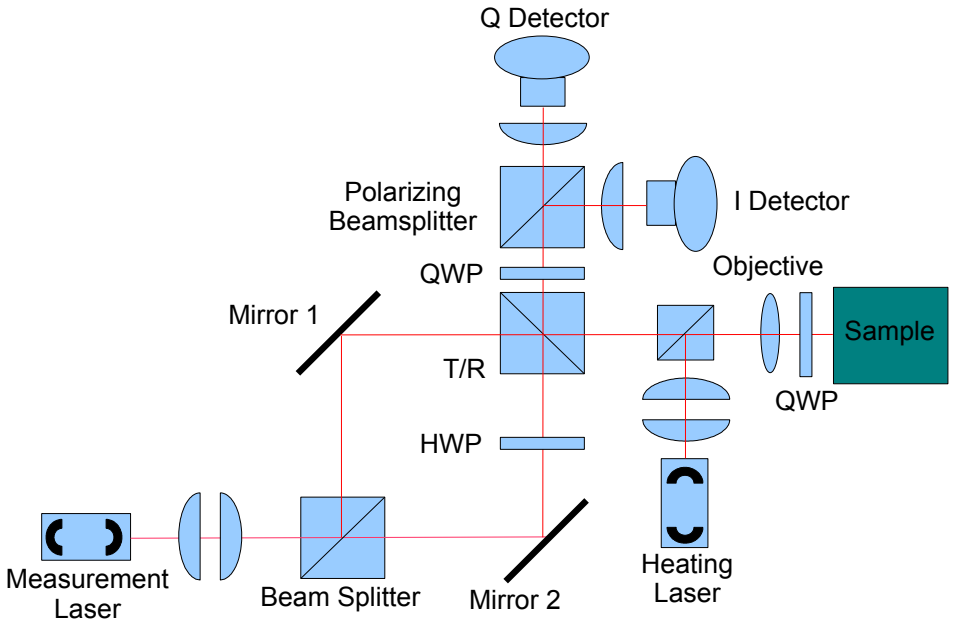

Figure 1.6: Photothermal Microscope Using a Quadrature Coherent Confocal Microscope.

The correlation of these preliminary experiments to the analytical approximations provides a basis for the research presented in this thesis. This research will provide a rigorous computational analysis of the thermal, mechanical and optical effects within human skin to obtain information about the displacement of scattering particles resultant from the changes in index of refraction and stresses incurred from the thermal effects. The photothermal effect will thus be measured directly from the displacement and not from the acoustic pressure wave generated similarly to the current imaging techniques of PTA.

Chapter 2

Thermal Displacement Simulation

The thermal model is a well-established numerical analysis described by Kowalski *et al.* [17], Kowalski [18], Kowalski and Whalen [19] [20], Wahl [21] and Whalen [22] that combines a transient finite difference thermal response model with an electromagnetic wave model and a refraction and reflection model to calculate the absorbed and internally reflected radiation within a material system [23]. This model is written in Fortran and comprises three processors; the pre-processor, main processor and post-processor.

The pre-processor, as discussed in Section 2.1, defines all parameters required for analysis as in input file named "pre_txt". The main processor takes data generated by the pre-processor and performs the rigorous computational analysis, using a finite difference method based upon a thermal transport model, Section 2.3, a radiation model to track the electromagnetic wave as rays through the system, including refraction and reflection, Sections 2.4 and 2.6, and a calculation along each ray for the change in index of refraction, optical path length and optical phase due to the

temperature change, Section 2.5.

2.1 Pre-processor

The pre-processor input file, "pre_txt", contains the necessary geometric, thermal, mechanical and optical parameters for the main processor to execute. These are defined in detail in Appendix A. This section will demonstrate a sample of "pre_txt" as it was used for this research in Table 2.1. The file, "pre_txt", is an extension-less text file of a specific format that can be read by the Fortran pre-processor one line at a time. Each parameter is input into "pre_txt" preceded by a line number, as seen in column one of Table 2.1.

The lines are read in sequentially to the pre-processor and the nodal system parameters, thermal and optical parameters, and boundary conditions are established. Each set of values is separated by commas and each line can have a variable number of parameters depending on what the pre-processor expects to see on each line. As with any configuration input file, it is critical that caution and care are taken in the construction of the file as a misplaced parameter would result in potential catastrophic errors in the numerical model.

The flow of the code is according to Figure 2.1. This figure places emphasis on the pre-processor portion and as each subsequent analysis phase is discussed throughout this paper, this figure will be updated accordingly.

The pre-processor takes in parameters from "pre_txt" and generates output files that

'line 1 :',	0,1,1,0,0,0,0,0	
'line 2 :',	0.01, 'set to this value'	
'line 3 :',	1	
'line 4 :',	1	
'line 5 :',	6.4e-06,1.1e-6,1.1e-6,	'general =length/(node)'
'line 5a:',	0.0,0.0,0.0,	'velocity for our case always zero'
'line 6 :',	992.2,4181.3,0.58,0.0,1759,0.0	
'line 7 :',	60e-6,20e-6,20e-6,0.0,0.0,0.0	
'line 8 :',	1.00786e-3,207e-6,0.495,4.54e-10,1e-4,34307	
'line 9 :',	0,	'usually zero'
'line 10:',	1.4,3.4e-37	
'line 11:',	660,	'expect this to be a noncritical input'
'line 12:',	5.001e-6,1	
'line 13:',	5.001e-6,2.5e-8	
'line 14:',	1,1,	'fixed inputs'
'line 15:',	0.0,0.0,0.0,	'give an example of a temporal pulse'
'line 16:',	1e-9s	
'line 17:',	0.10	
'line 18:',	0	
'line 19:',	1,0.0,4908.73,	'1.,0. are fixed values'
'line 20:',	1	
'line 21:',	0.0,14.11e-6,14.11e-6,0.0,5.88e-6,5.88e-6	
'line 22:',	15.97e-03,0.0, 10e-6,10e-6	
'line 23:',	2.545e-3,15.99142e-3,	'not critical if plane wave'
'line 24:',	4908.73,2.14286e-6,1.5e-6,	'except for zig not used because plane wave'
'line 25:',	1.0,0.0,0.0,	'usually normally incident beam use these values'
'line 26:',	0.5,0.5,	'the code includes the polarization of th eincident laser, this input assumes unpolarized'
'line 27:',	2.5e-04,	'this is the spatial step size for refraction model, half node'
'line 28:',	7.0,7.0,0.0,	heat transfer boundary conditions'
'line 29:',	0.0,0.0,0.0	
'line 30:',	0.0,0.0,0.0	
'line 31:',	0.0,0.0,0.0	
'line 32:',	1,	node number of const. temp'
'line 33:',	1.0,	'cycle fraction on, usually leave at 1'
'line 34:',	37.0,1.0,	'ambient temp. and index'
'line 35:',	37.0,	'initial temp'
'line 36:',	0,0,	'control parameters, leave at this value'
'line 37:',	0,1,	'control paramters for post process'
'line 38:',	0.25,3.979e-2,	'far field detector'
'line 39:',	30,20,1,	'post process beam division'
'line 40:',	1.0	
'line 41:',	90000.,1.0,1.0,1.0,0.03,1.0,	'phase change variables'

Table 2.1: "pre_txt" File Used for This Research.

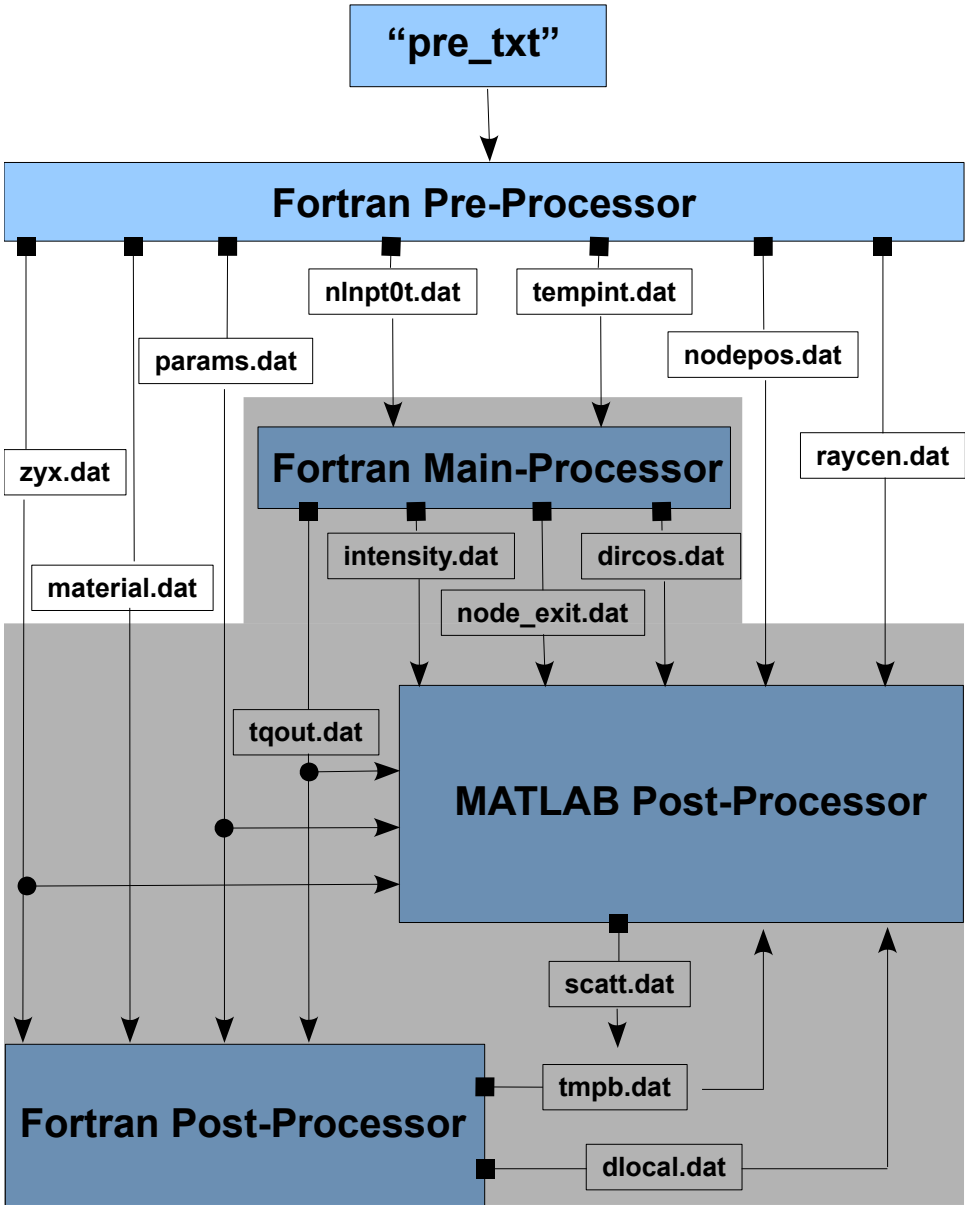

Figure 2.1: Flow Diagram of the Code with Emphasis on the Pre-Processor.

get called by the main and post-processors. The information in these files is summarized in Table 2.2 and relates to thermal, geometric and optical properties and parameters of the system under analysis. These will be discussed in the appropriate sections as needed to understand the methodology employed by this research.

"nlnpt0t.dat"	This file contains all the necessary input parameters into the main processor. Some of these are broken out as separate files for ease of use in the post processing phase.
"tempint.dat"	All the initial temperature data is stored here and is only used in the main processor.
"params.dat"	This file contains specific parameters from "nlnpt0t.dat" that are used in the post-processing phase.
"zyx.dat"	This file contains the node center positions for all node volumes. It is used in the Post-processor for both the Fortran and MATLAB stage.
"material.dat"	This file contains all the information about the material. It is used in the displacement calculation by both the Fortran and MATLAB stage.
"nodepos.dat"	This is a separate file from "nlnpt0t.dat" containing just the node positions at all corners. It is used in the MATLAB post-processor.
"raycen.dat"	This is a separate file from "nlnpt0t.dat" that includes the center location of all the incident rays . It is used in the MATLAB post-rocessor.

Table 2.2: Output Files Generated by the Pre-processor.

Some parameters in "pre_txt" are used only in specific models and post-processing

codes not part of this research. These will not be discussed aside from a high-level explanation in Appendix A. Additionally, there are thermal model output files that are not included in Figure 2.1 or in Table 2.2 as they are also used in other post-processing codes that are were not used for this research.

2.2 Model Geometry

The computational model comprises a grid of 18×18×9 (x, y, z) voxels (nodes) within a volume of 20 μm×20 μm×60 μm. These parameters are defined on Lines 5 and 7 of "pre_txt". Line 5 establishes a minimum node length for z, y and x, $\Delta z, \Delta y$ and Δx in meters, respectively, and Line 7, the dimensions of the sample, also with respect to z, y and x. From these, the pre-processor then computes the number of nodes for each coordinate direction.

The node numbering starts with an ambient node, 1, representing the volume surrounding the sample. Node number 2 starts at the $x, y = 0$, and z =60 μm corner and increments sequentially along the x-axis, then the y-axis, and finally the z-axis until the $z = 0$ layer is reached. In the present case the dimensions are 20 μm×20 μm×60 μm which produces 9 slices in the z direction of 324 nodes.

An irradiated surface is chosen by defining the x, y and z coordinates on Line 21 as a maximum corner and minimum corner on one of the six faces of the sample. The pre-processor then determines which nodes are inscribed by the irradiated area and assigns a ray for each node representing the portion of the incident beam for that node. The ray is then traced through the sample using a geometrical optics technique and information is gathered for the intensity, optical path length (OPL),

physical path length (PPL), reflection and transmission at each node interface. These calculations will be discussed in more detail in Section 2.6.

The model geometry is shown in Figure 2.2. This image is not exact to the sample used in this research and is only representative of the nodal arrangement. The irradiated surface, however, does coincide with this research and is centered on the positive $x - y$ surface. Node 2 is labeled for clarity.

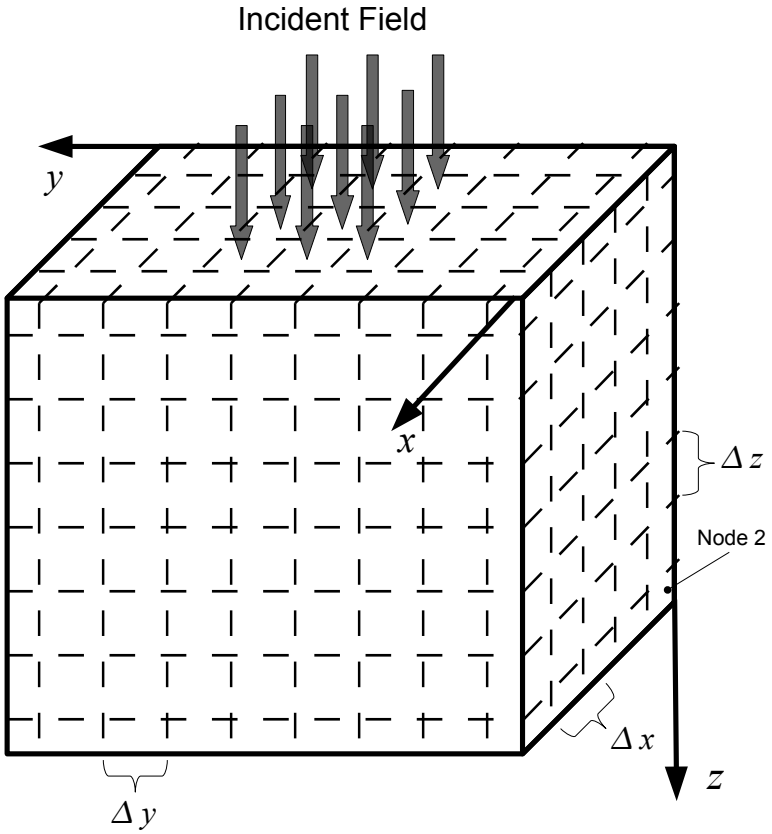

Figure 2.2: Model Geometry. The irradiated area is with respect to this research on the positive $x - y$ face.

It can be observed from the figure that the corner nodes are of one eighth the volume, the edge nodes are one quarter the volume and the surface nodes are one half the

volume of an expected node of dimension $\Delta x \times \Delta y \times \Delta z$. The nodes that meet this volume expectation are located within the sample. This realization is critical in the thermal stress calculation, discussed in Section 3.1.2, for the calculation of the effective radius using a spherical approximation of the node.

The numerical analysis via the raytrace model takes each ray to start at the center of the incident surface and values are taken for parameters such as displacement and temperature to be at the centers of the nodes the ray passes through. To allow for incidence upon any surface x, y or z of the source beam, all surfaces nodes must have their centers at the surface, all edge nodes must have their centers at the surface-to-surface interface and all corner nodes must have their centers at the corner.

2.3 Thermal Transport Models

The thermal response of a material is governed by the differential energy balance

$$\nabla q = \left(\frac{\rho c_p}{K_t}\right) \frac{\partial T}{\partial t} - \frac{q''_{abs}}{K_t}. \tag{2.1}$$

where T is the temperature, t is time, q''_{abs} is the absorbed radiation per unit volume and q is the heat flux vector at a location [23]. By defining q appropriately, four different heat transfer mechanisms can be applied to solve the differential energy balance for materials with different thermal characteristics. These are the Parabolic One Step (POS), Hyperbolic One Step (HOS), Parabolic Two Step (PTS) and Hyperbolic Two Step (HTS) models. The focus of this paper will be on the POS model, also known as the Fourier Conduction Law model, as it was the mechanism chosen for this

research. The small size and long time period were the considerations for choosing this model. These mechanisms form the foundation for the main processor and are solved through a finite difference iterative algorithm.

It is important to select the correct thermal transport model in "pre_txt" because the objective of each is to predict the temperature response of the medium. The determination of the index of refraction within the medium, according to the refraction model discussed in Section 2.6 is coupled to the thermal response of the medium. This variation in the medium's index of refraction determines the medium's response to the incident laser radiation which is linked back to the thermal model via radiation absorption by the radiation model, Section 2.4 [22].

Both the POS and HOS models are used for analysis of dielectric materials where as the PTS and HTS are primarily used in analysis of metals. The two-step process inherent to the PTS and HTS requires short heating time on the order of magnitude of picoseconds. This is referred to as microscale heat transfer, and is due to the dominant heat carrier of metals being the electrons. The PTS and HTS models will not be discussed in this paper since the parameters discussed in Section 2.3.1 refer to heating that is not microscale and the sample medium is tissue, a dielectric material. The HOS will be discussed in brief in Section 2.3.2 because of its similarities to the POS model with explanation for why it was not the proper choice for this research.

The thermal transport model is selected in Line 1 of "pre_txt" using the second column, "model." The choices are illustrated in Appendix A. In addition to defining the correct model, it is necessary to select the correct type of conduction using the first column of Line 1, "nfmodel", non-Fourier (1), or Fourier (0).

2.3.1 Parabolic One Step Model

The description of the heat flux for the medium's temperature gradient, by the Fourier Conduction Law, is written as

$$q = -K_t \nabla T \tag{2.2}$$

which when substituted into Equation 2.1 , yields the parabolic differential equation:

$$\rho c_p \frac{\partial T}{\partial t} = -\nabla \left(K_t T \right) + \frac{q''_{abs}}{K_t}. \tag{2.3}$$

The term $\frac{q''_{abs}}{K_t}$ is the absorbed laser radiation per volume and will be discussed in more detail in Section 2.4. After the absorbed laser radiation per volume is calculated by the radiation model, the transient temperature field is calculated by solving Equation 2.3 using a modified Euler Technique. This technique applies a predictor-corrector method for the temporal derivatives with which a future value is predicted for a specific time step over the entire computational grid, then a current value is calculated, similarly, and compared to the future value. A flow chart for the predictor-corrector can be seen following this section in Figure 2.3. Once the difference between future and current values lies within a convergence criterion, Line 2, the solution is satisfied and the next time step is evaluated. The spatial derivatives are determined using a finite difference method as part of the discretized solution to Equation 2.3 shown below as Equation 2.5.

This method allows for a second order solution rather then the first order limitation of

the finite difference method. This is seen in the relationship between the absorption and the index of refraction: the absorption in a node is dependent on the ray's path length through the node and the path length is dependent on the index of refraction of the node. The predictor-corrector makes a prediction of the future absorption from the current temperature of each node, then it uses this absorption to calculate the future temperature. With the new temperature, a new absorption is then calculated and compared to the predicted value. This is repeated until the convergence criterion is met.

For the finite difference method to work correctly, it is assumed that the nodes are small enough to approximate the temperature accurately between each pair of nodes according to a linear profile. Additionally, it is assumed that the heat flow between the nodes can be approximated linearly and that the node point temperature and the average temperature of the node are the same [21].

To derive the finite difference equation used for the predictor stage, Equation 2.3 must be expanded according to

$$\frac{\partial T}{\partial t} = K_t \left[\frac{\partial}{\partial x}\left(\frac{\partial T}{\partial x}\right) + \frac{\partial}{\partial y}\left(\frac{\partial T}{\partial y}\right) + \frac{\partial}{\partial z}\left(\frac{\partial T}{\partial z}\right) \right] + Q \tag{2.4}$$

where the following non-dimensional parameters have been defined as

$$\bar{T} = \frac{T - T_0}{q''_{ch}}, \quad \bar{t} = \frac{t}{\rho c L_c}, \quad Q = \frac{q''_{abs} L_c}{q''_{ch} K_t}$$
$$\bar{x} = \frac{x}{L_c}, \qquad \bar{y} = \frac{y}{L_c}, \qquad \bar{z} = \frac{z}{L_c}$$

where L_c is the length of the sample in the z direction and q_{ch} is the characteristic heat flux [21, 22]. By dropping the bar notation, substituting into Equation 2.3 then multiplying through by the differential volume, $\Delta x \Delta y \Delta z$, and integrating spatially, the resultant difference equation is

$$T^F = T^P + \Delta t \frac{K_t}{L_c \Delta x}\left[\left(\frac{\partial T}{\partial x}\right)_{x^+} - \left(\frac{\partial T}{\partial x}\right)_{x^-}\right] + \Delta t \frac{K_t}{L_c \Delta y}\left[\left(\frac{\partial T}{\partial y}\right)_{y^+} - \left(\frac{\partial T}{\partial y}\right)_{y^-}\right] + \Delta t \frac{K_t}{L_c \Delta z}\left[\left(\frac{\partial T}{\partial z}\right)_{z^+} - \left(\frac{\partial T}{\partial z}\right)_{z^-}\right] - \Delta t \frac{QVL}{\Delta x \Delta y \Delta z} \quad (2.5)$$

where T^F is the future temporal temperature value, T^P is the present temporal temperature value, $QVL = \iiint Q \, \mathrm{d}x \, \mathrm{d}y \, \mathrm{d}z$ and the forward and backward difference methods for the spatial derivatives in terms of the temperature are

$$\left(\frac{\partial T}{\partial x}\right)_{x^+} = \frac{T_{i+1} - T_i}{\Delta x}; \quad \left(\frac{\partial T}{\partial x}\right)_{x^-} = \frac{T_i - T_{i-1}}{\Delta x} \quad (2.6a)$$

$$\left(\frac{\partial T}{\partial y}\right)_{y^+} = \frac{T_{j+1} - T_j}{\Delta y}; \quad \left(\frac{\partial T}{\partial y}\right)_{y^-} = \frac{T_j - T_{j-1}}{\Delta y} \quad (2.6b)$$

$$\left(\frac{\partial T}{\partial z}\right)_{z^+} = \frac{T_{k+1} - T_k}{\Delta z}; \quad \left(\frac{\partial T}{\partial z}\right)_{z^-} = \frac{T_k - T_{k-1}}{\Delta z}. \quad (2.6c)$$

For the POS model to calculate the temperature properly at each node, it requires a built-in mechanism that tracks the conductance between adjacent nodes. This is described as a conductance array that contains each node of interest and each adjacent node to the node of interest. This is summarized by Table 2.3 and is represented by the nomenclature $CND\,(n, m)$ where n is the node number of interest and m

is the direction of the adjacent node. To access the conductance value for the node adjacent to node 10, for example, in the $+x$ direction one would use the array location, $CND\,(10, 5)$.

Node	$+z$	$-z$	$+y$	$-y$	$+x$	$-x$
2	1	2	3	4	5	6
3	1	2	3	4	5	6
$\vdots$	1	2	3	4	5	6
n	1	2	3	4	5	6

Table 2.3: Conduction Array. n is the last node number of the system.

Similarly, there is also an interconnection array, $ICONN\,(n, m)$, which keeps track of the adjacent node numbers with respect to the node of interest. This uses the same setup as seen for the conduction array in Table 2.3. These arrays are constructed by the pre-processor and the data is stored in the output file "zyx.dat". Using $ICONN\,(n, m)$ in concert with $CND\,(n, m)$ and substituting into Equation 2.5 yields the final expression used in the POS predictor step,

$$T_n^F \;=\; T_n^P \;+\; \frac{\Delta t}{\Delta x \Delta y \Delta z}\left[\sum_{m=1}^{6} \frac{CND\,(n, m)}{L_c}\left(T^P_{(ICONN(n,m))} - T_n^P\right) + QVL_n^P\right] \quad (2.7)$$

where i, j and k are the indices of the x, y and z coordinates, respectively. This equation can be iterated and the future temperature can be calculated at each time

step because all the right-hand terms are known.

The corrector stage of the POS model takes the average of the present and future temporal derivatives according to

$$T_n^F = T_n^P + \frac{\Delta t}{\Delta x \Delta y \Delta z}\left[\sum_{m=1}^{6} PRE\,(n,m) + CORR\,(n,m)\right] \tag{2.8a}$$

$$PRE\,(n,m) = \frac{CND\,(n,m)}{L_c}\left(T^P_{(ICONN(n,m))} - T_n^P\right) + QVL_n^P \tag{2.8b}$$

$$CORR\,(n,m) = \frac{CND\,(n,m)}{L_c}\left(T^F_{(ICONN(n,m))} - T_n^F\right) + QVL_n^F \tag{2.8c}$$

where the superscript P represents the present time step, the superscript F represents the future time step and n is the node of interest. The predictor-corrector is repeated until the convergence criterion is met. This criterion ensures stability and is calculated with respect to the temporal integrations as presented below in terms of Δt, the critical time step. This situation must be satisfied to achieve accuracy in the approximation.

$$\Delta t \leqq \frac{(\rho c_p)}{\sum CND\,(i,j)}. \tag{2.9}$$

The code allows for boundary conditions to be imposed that are convective, insulated or a surface heat flux, the latter of which can be in the form of an scalar, pulses or a cosine function. The boundary condition comes from the energy balance on the system's surface governed by the equation

$$q_s'' A = -AK_t \frac{\partial T}{\partial x} + hA\left(T_l - T_0\right) \tag{2.10}$$

where h is the convective coefficient and q_s'' is the surface heat flux. which when normalized by the non-dimensional parameters described previously and solved for the spatial derivative takes the form of Equation 2.11, shown here for the x coordinate. This is then substituted into Equation 2.8 for the conductance terms at the systems boundaries [21]. For this research, the convective boundary conditions are applied only to the positive and negative z-oriented boundaries. The boundary conditions on the remaining surfaces are discussed later and are considered to be adiabatic. The values, as seen on Line 28 of "pre_txt", are explained in Section 2.7

$$\frac{K_t}{L_c}\frac{\partial T}{\partial x^*} = -q_s^* + hT_{ch}\bar{T} \tag{2.11}$$

where T_{ch} is the characteristic temperature and $*$ is the normalized value.

The POS model is utilized for materials under long heating periods and with large spatial scales. The alternative methods, the HOS, HTS and PTS are categorized as microscale heat transfer models. To determine which microscale heat transfer model to employ, it must be established whether the dominant heat carrier is by free electrons or phonons and the time and length scales of the problem [22]. Additionally, materials similar to water that are nanometer scale in size and under heating for time periods in the nanosecond regime qualify for microscale treatment. This will be addressed, if briefly, for the HOS model and as mentioned previously, will not be discussed for the PTS and HTS models as they apply to metals.

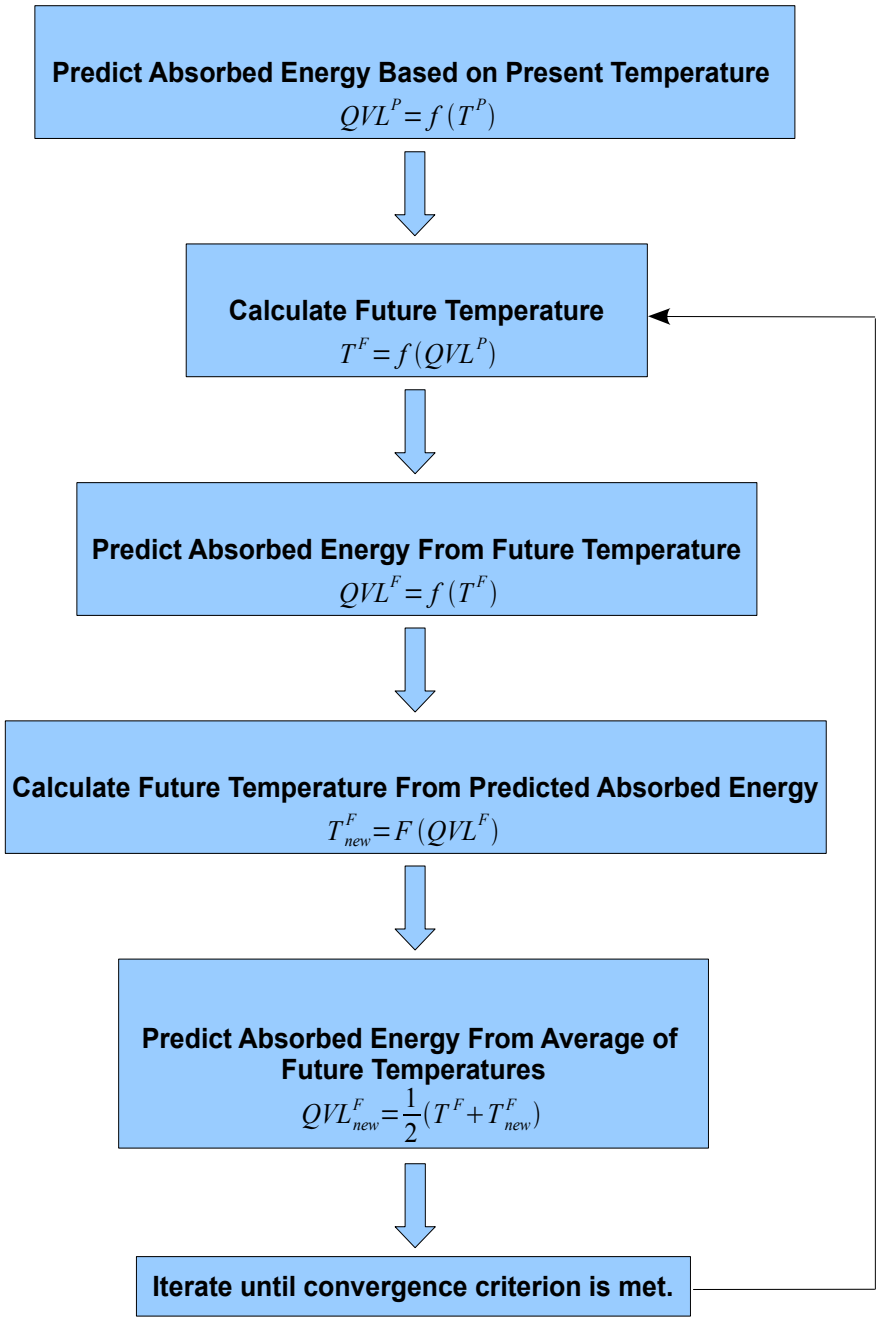

Figure 2.3: Flow Chart for the Predictor-Corrector Algorithm

2.3.2 Hyperbolic One Step

Situations involving short characteristic heating times or systems existing at temperatures approaching absolute zero cause questionable results from the POS model. For these cases, it becomes necessary to model using a hyperbolic nonlinear differential equation that allows for a time delay to exist between the heat flux and the temperature gradient. This model describes the propagation of energy as a wave phenomena and introduces a relaxation time, τ_r and thermal wave propagation speed, v_t, a finite velocity for the thermal pulse.

The Hyperbolic One Step model expands upon the heat flux equation of the POS according to

$$q = -\tau_r \frac{\partial q}{\partial t} - K_t \nabla T \tag{2.12}$$

with inclusion of the relaxation time according to

$$\tau_r = \frac{K_t}{v_t^2 \rho c_p}. \tag{2.13}$$

Like the POS model, the HOS model describes the thermal transport in dielectric materials. The difference between the two models lies in the time period of interest. By treating tissue as a dielectric with similar thermal properties as water the expression for τ_r can be solved using the input parameters in "pre_txt"; $K_t = .58\ \frac{\mathrm{W}}{\mathrm{K \cdot m}}$, $\rho = 992.2\ \frac{\mathrm{kg}}{\mathrm{m}^3}$, $c_p = 41481.3\ \frac{\mathrm{J}}{\mathrm{kg \cdot K}}$ and $v_t = \frac{v_{sp}}{\sqrt{3}} = 856.78\ \frac{\mathrm{m}}{\mathrm{s}}$. The wave propagation speed in dielectrics can be approximated according to Joseph *et al.* [24] as the sonic

speed in water, v_s, divided by $\sqrt{3}$. This yields a value of $\tau_r = 1.8 \times 10^{-13}$ s.

According to Whalen [22], the value for τ_r ranges between 10^{-10} s for gasses and 10^{-14} s for metals. These low values for the relaxation time indicate that the HOS model should be used in experiments where the heating time is much less then nanoseconds. Additionally, this model provides a better description of systems that are of a spatial scale of nanometer magnitude. This research applies a 5 μs pulse, defined in "pre_txt" on Line 12, to a system with dimensions that are of several micrometers. This analysis was applied in determining which model was to be used in this research.

To illustrate this, Figure 2.4 shows a comparison of the POS to the HOS using a relative non-dimensional time scale related to the heating time, t and the relaxation time, τ_r by the ratio $\frac{t}{\tau_r}$ [22]. This is plotted with respect to the instantaneous transmittance, a comparison of the ratio of energy incident on a surface to that which is absorbed. The behavior of dielectrics at short time scales can be seen to be very different until around the relaxation time of the material. Examination of this figure indicates that any ratio of $\frac{t}{\tau_r} > 3$ allows for either model to be used, and the additions to the POS model that are included in the HOS model are not significant.

2.3.3 Parabolic One Step Model Verification

The Fortran thermal model has been well defined and benchmarked for each of the transport models by comparison of either analytical or experimental results to the numerical results of the simulation. Wahl [21] provides several analytical thought

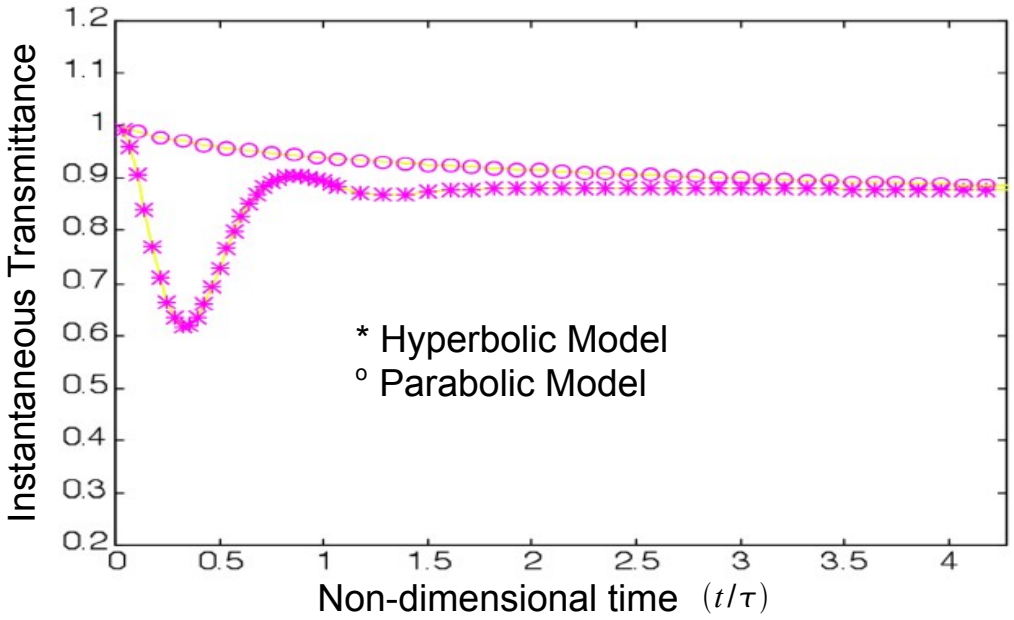

Figure 2.4: Comparison of the Instantaneous Transmittance Over Time of the POS and HOS Models.

experiments to validate the POS model. However physically unrealistic, they demonstrate the capability of the code according to solvable analytic situations. Whalen [22] utilizes a z-scan experiment to correlate results found by Sheik-Bahae [25]. Additionally, he and Kowalski [19, 20] extend this to include the HOS model with comparison to experimental results collected by Chen and Tien [26] and Paddock and Eesley [27]. The PTS and HTS models are proven by Kowalski [23] and Whalen [22] by comparison to experimental results obtained by Qiu and Tien [28].

This section will elaborate upon the methodology initially used by Wahl [21] to verify, analytically the POS model. Several experiments were conceived to test the capability of the code in situations involving linear optical materials with and without reflections

and thermal heat fluxes applied, the refraction model discussed in Section 2.6 and a nonlinear optical material with thermal fluxes applied. Each instance was solved analytically, then numerically through the Fortran thermal model and the results compared. Chosen for this report, are the simple cases of a linear optical medium with no heat flux applied, and a the linear optical medium with reflections. The necessary parameters are listed in Table 2.4.

These parameters are for a one dimensional case with an incident laser beam irradiated on the positive z face of the sample. The parameters used for comparison are temperatures at the $z = 0$ and $z = L$ surfaces, the surface reflection coefficient, Γ_I, the ratio of absorbed radiation, q''_{abs} to the incident radiation and the ratio of transmitted radiation, q''_{trans} to the incident radiation according to the following expressions:

$$\Gamma_I = \left[\frac{n - n_0}{n + n_0}\right]^2 \tag{2.14}$$

$$\frac{q''_{abs}}{q''_o} = (1 - \Gamma_I)\left[1 - e^{-\alpha L}\right] \tag{2.15}$$

$$\frac{q''_{trans}}{q''_o} = (1 - \Gamma_I)\, e^{-\alpha L} \tag{2.16}$$

where n is the material's index of refraction. From here on n is assumed to be the index of refraction and used as an indexing parameter representing a node number, or temporal coordinate, will be denoted as such.

T_0	0.0 K	Ambient Temperature
n_0	1.0	Index of Refraction in Air
q_0''	1000 $\frac{\mathrm{W}}{\mathrm{m}^2}$	Incident Heat Flux
h	8.0 $\frac{\mathrm{W}}{\mathrm{m}^2\mathrm{K}}$	Convective Coefficient
L	0.01 m	Length of Sample
K_t	0.6 $\frac{\mathrm{W}}{\mathrm{mK}}$	Thermal Conductivity
ρ	1000 $\frac{\mathrm{W}}{\mathrm{m}^2}$	Density
c_p	4000 $\frac{\mathrm{kJ}}{\mathrm{kgK}}$	Specific Heat
β	0.0 $\frac{\mathrm{m}^3}{\mathrm{K}}$	Coefficient of Isobaric Volume Expansion
$\bar{n}_1$	1.2	Material Linear Index of Refraction
$\bar{n}_2$	0.0	Material Nonlinear Index of Refraction
α_0	100 $\frac{1}{\mathrm{m}}$	Material Linear Absorption Coefficient
α_2	0 $\frac{\mathrm{m}}{\mathrm{W}}$	Material Nonlinear Absorption Coefficient

Table 2.4: Linear Optical Material POS Verification Parameters

The temperatures were found analytically using Equation 2.2 and Equation 2.23 from

Section 2.4. Following the temperature calculation, the values for the reflection coefficient, absorbed radiation and transmitted radiation were found using Equations 2.14-2.16. The values for these are found in Table 2.5 and correlate well to the numerical results after running the Fortran thermal analysis with the parameters input into "pre_txt" that are according to Table 2.4. All values were taken after a time of 8000 seconds.

Parameter	Analytical Value	Numerical Value
$T\left(z=0\right)$	78.25	78
$T\left(z=L\right)$	82.72	82
Γ_I	0.00826	0.0082
$\frac{q''_{abs}}{q''_0}$	0.626	0.628
$\frac{q''_{trans}}{q''_0}$	0.364	0.364

Table 2.5: Analytical versus Numerical Values for a Material with Linear Absorption with no Reflections

Using the parameters of Table 2.4 and the same approach described for the case with no reflections, with one added equation for the back reflected energy, $q''_B R$,

$$\frac{q''_{BR}}{q''_o} = \frac{q''_{abs}}{q''_o}\left(1-\Gamma_I\right)\left[1-e^{-\alpha L}\right] \tag{2.17}$$

the results for the linear optical medium with reflections are summarized in Table 2.6.

Parameter	Analytical Value	Numerical Value
$T\,(z=0)$	78.25	78
$T\,(z=L)$	82.72	81.5
Γ_I	0.00826	0.0082
$\frac{q''_{abs}}{q''_0}$	0.628	0.629
$\frac{q''_{trans}}{q''_0}$	0.361	0.361

Table 2.6: Analytical versus Numerical Values for a Material with Linear Absorption and Reflections

It can be seen that the back reflected heat flux alters the absorbed energy result slightly from that of Table 2.5 and has a calculated value of $\frac{q''_{BR}}{q''_0} = 0.001091$ which agrees with the numerical results.

2.4 Radiation Model

The main processor comprises the finite difference algorithm for the thermal transport model as well as the radiation model of this section, index of refraction model of Section 2.5 and the raytrace model of Section 2.6. It takes in values from "nlnpt0t.dat" which are defined by the pre-processor based on the values input into "pre_txt". Figure 2.5 shows this as a modification to Figure 2.1 where everything but the main processor is shaded out. The files that are created here are summarized in Table 2.7.

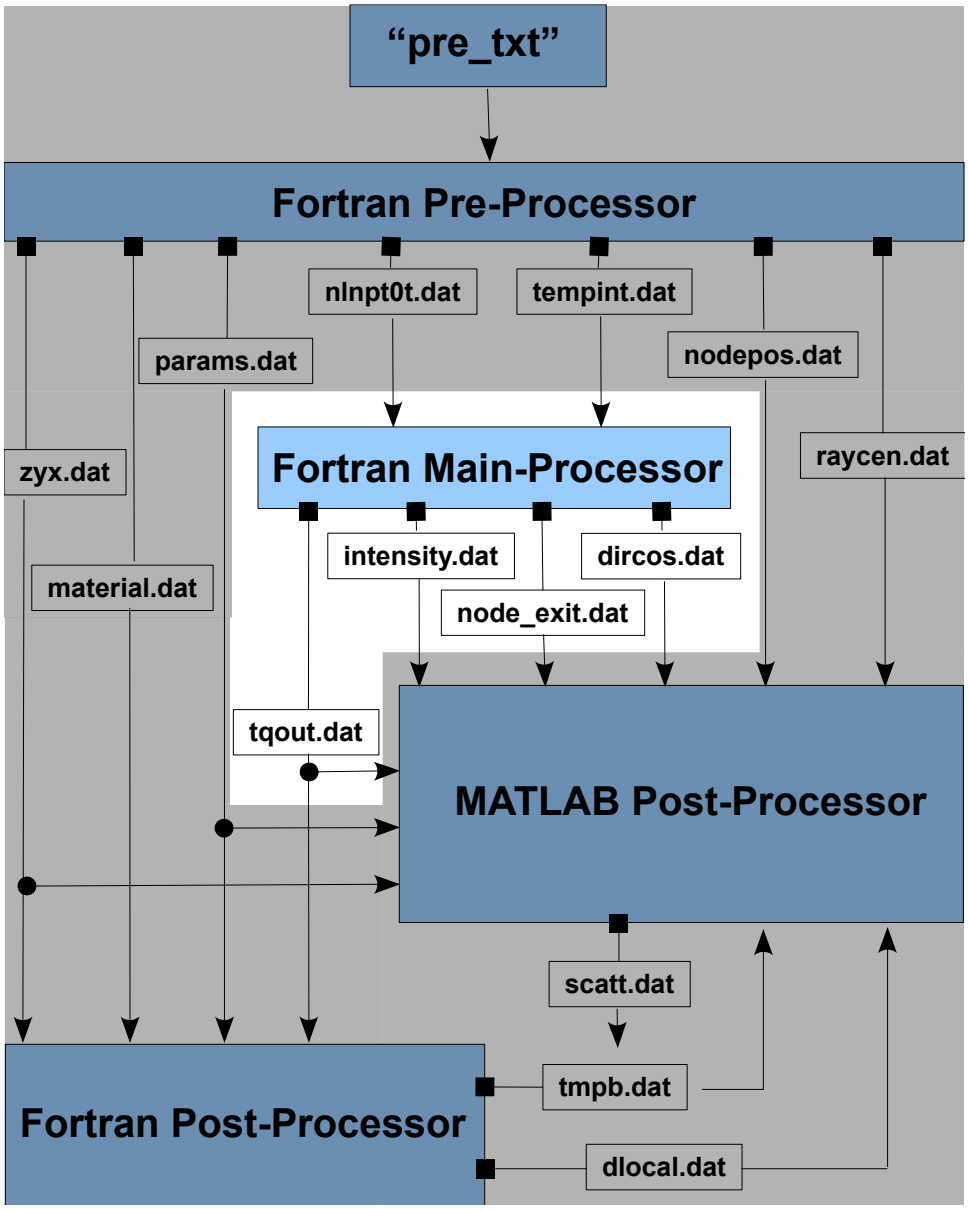

Figure 2.5: Flow Diagram of the Code with Emphasis on the Main-Processor.

"tqout.dat"	This file contains all the temperature data for each node at each time step. It is used in the Fortran and MATLAB post-processors.
"intensity.dat"	This file contains the irradiance values that each ray contributes upon each node. This is used in the MATLAB post-processor.
"node_exit.dat"	This file contains the ray nodal exit locations along each ray path and the OPL due to the heating at these locations. This is used in the MATLAB post-processor.
"dircos.dat"	This file contains the ray nodal exit direction cosines along each ray path and the PPL at these locations. This is used in the MATLAB post-processor.

Table 2.7: Output Files Generated by the Main-Processor.

The radiation model is an electromagnetic wave model that ties the thermal, nonlinear optical, and radiation transport models together. The radiation incident on the sample from the laser source affects the temperature distribution within the medium of the sample which in return affects the absorption, scattering and emission of the radiation by the temperature dependent radiation transport properties [22]. The model allows the user to select in "pre_txt" the type of laser profile, Line 1, column 7, as a plane wave, top hat, or spatial Gaussian as well as the temporal form, Line 15. For this research a spatial Gaussian (value = 0) was chosen with no temporal form. The beam profile irradiance is defined by

$$I(r,z) = I_0 \left(\frac{\omega_0}{\omega\left(z\right)} \right)^2 e^{-\left(\frac{2r}{\omega(z)}\right)^2}. \tag{2.18}$$

$$\omega(z) = \omega_0 \sqrt{1 + \left(\frac{z\lambda}{\pi\omega_0^2}\right)^2} \tag{2.19}$$

where $z_R = \frac{\pi\omega_0^2}{\lambda}$ is the Rayleigh length; the distance along the propagation direction on the beam from the waist location where beam radius is equal to ω_0, to where the area of the cross section is doubled. The function $w(z)$ is the radial distance at which the field amplitude and intensity are $\frac{1}{e}$ and $\frac{1}{e^2}$, respectively and is referred to as the spot size at some axial distance, z. This is the location of the *Optical Zone* mentioned in Section 1.1. The variable r is a radial distance from the beam center and z is the distance along the direction of propagation. Figure 2.6 shows the geometry of the beam. The parameters listed in Equation 2.18 are defined in Table 2.8 with their respective values and input line in "pre_txt". I_0 represents the irradiance $\left(\frac{\mathrm{W}}{\mathrm{m}^2}\right)$ at the waist, however, in "pre_txt", according to Table 2.8, the value input is the irradiance at the lens, I_g. From this the pre-processor calculates the irradiance at the sample face, then at the waist.

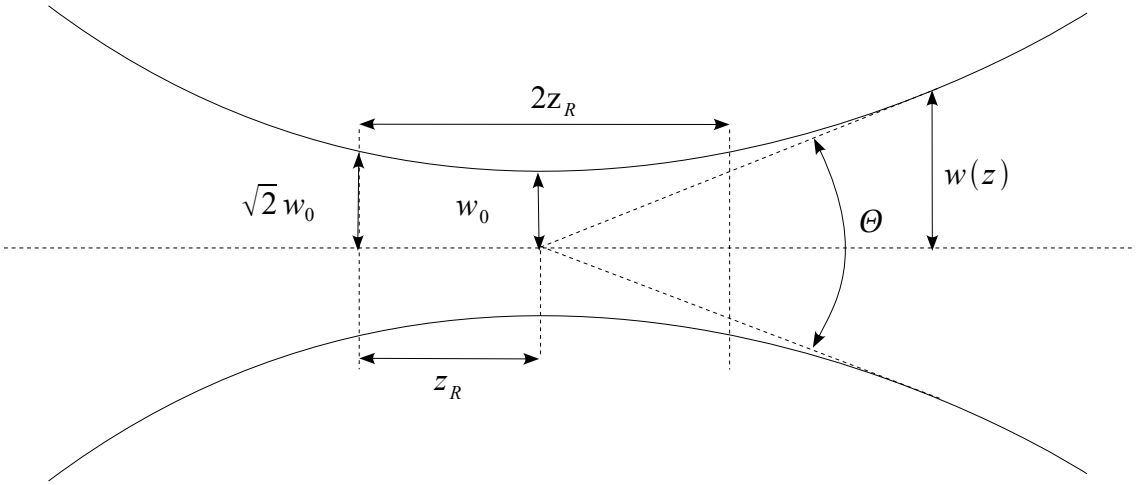

Figure 2.6: Geometry of the Gaussian beam.

Parameter	Value	Line, Column	Description
ω_0	3e-6 μm	24, 2	Radius at beam waist.
$\omega\,(f)$	2.545e-3 m	23, 1	Radius of spot size at focal length from waist.
λ	1.5e-6 μm	24, 3	Wavelength.
$zlsl$	15.7e-3 m	22, 1	Distance from lens to the sample.
f	15.99142e-3 m	23, 2	Focal length of lens.
I_g	$4908.73\frac{\mathrm{W}}{\mathrm{m}^2}$	24, 1	Irradiance at lens.
q_s''	$4908.73\frac{\mathrm{W}}{\mathrm{m}^2}$	19, 3	Surface Flux.
$r_{iz1}, r_{iy1}, r_{ix1}$	0.0, 14.11e-6 μm,14.11e-6 μm	21, 1-3	Maximum corner of irradiated area.
$r_{iz2}, r_{iy2}, r_{ix2}$	0.0, 5.88e-6 μm, 5.88e-6 μm	21, 4-6	Minimum corner of irradiated area.
c_z, c_y, c_x	0.0, 10e-6 μm, 10e-6 μm	22, 2-4	Beam center on sample.

Table 2.8: Gaussian Beam Parameters.

The radiation model, via the pre-processor, reads in from "pre_txt" the parameters describing the irradiated area. The irradiated area has rectangular geometry and is described in "pre_txt" by a center location, $c_x, c_y,$ and c_z, a corner nearest the point $(0, 0, 0)$ (*Minimum Corner*), $r_{iz2}, r_{iy2}, r_{ix2}$ as well as its diagonal (*Miaximum Corner*), $r_{iz1}, r_{iy1}, r_{ix1}$. For this research the irradiated area is centered on the $x - y$ face at $z = 0$ with corner locations per Table 2.8 to enclose 36 nodes symmetric about the center of the sample. For each of these nodes, the pre-processor defines a ray that is perpendicular to the beam wavefront and centered in x and y on the node upon which it is incident. The wavefront orientation can be determined by the radius of curvature,

$$R(z) = z\left[1 + \left(\frac{z_R}{z}\right)^2\right]. \tag{2.20}$$

Each of these rays is tracked separately through the sample and the thermal heating, optical phase change and reflection are calculated.

The electromagnetic energy transfer to a surface is

$$q''_{surf} = \int_{\Omega}\int_{A_p} I(r,z)\ \mathrm{d}A_p\,\mathrm{d}\Omega \tag{2.21}$$

where, for a plane surface, $\mathrm{d}\Omega = \sin\theta\,\mathrm{d}\phi$ and $\mathrm{d}A_p = \cos\theta\,\mathrm{d}A$, θ is the angle from the normal, ϕ is the angle of rotation about the normal and A is the area on the planar surface. This gives the expression for the energy transfer to a plane surface, according to Wahl [21], as

$$q''_{plane} = \int_0^{\frac{\pi}{2}}\int_0^{2\pi}\int_A I(r,z)\cos\theta\sin\theta\,\mathrm{d}A\,\mathrm{d}\phi\,\mathrm{d}\theta \tag{2.22}$$

The intensity is described by the radiative transport equation for an absorbing, scattering and emitting medium as

$$\partial I\left(r,z\right) = \partial I_{abs} + \partial I_{scatt_{out}} + \partial I_{scatt_{in}} + \partial I_{emitt} \tag{2.23a}$$

$$\partial I_{abs} = -\alpha_r I\left(r,z\right)\partial s \tag{2.23b}$$

$$\partial I_{scatt_{out}} = -\alpha_s I\left(r,z\right)\partial s \tag{2.23c}$$

$$\partial I_{emitt} = \alpha_r I_B \partial s \tag{2.23d}$$

$$\partial I_{scatt_{in}} = \frac{1}{4\pi}\int_{\Omega} \alpha_s I\left(r,z\right) P \partial\Omega \tag{2.23e}$$

where $I_B = \frac{\sigma_{sb}T^4}{\pi}$ is the black body emitted intensity, $\sigma = 5.67e{-}8\ \frac{\mathrm{W}}{\mathrm{m^2K^4}}$ is the Stefan-Boltzman constant, α_r is the linear absorption coefficient, α_s is the linear scattering coefficient, s is a surface and P describes the distribution of randomly scattering particles.

According to Kirchoff's law, the absorption at a single wavelength is equal to the emission at the same wavelength, $\alpha_\lambda = \varepsilon_\lambda$, where α_λ is the ratio of absorbed energy to absorbed black body energy and, similarly, ε_λ is the ratio of emitted energy to emitted black body energy. This results in

$$\partial I = -\left(\alpha_r + \alpha_s\right) I \partial s + \alpha_r I_b \partial s + \frac{1}{4\pi}\alpha_s I P \partial\Omega \tag{2.24}$$

Through this relationship and because the emitted intensity is much smaller then the laser intensity throughout the medium Equation 2.24 simplifies, according to Whalen [22], to

$$\frac{\partial I\left(r,z\right)}{\partial \ell} = -\left(\alpha_r + \alpha_s\right) I\left(r,z\right). \tag{2.25}$$

For the heating laser, the material is highly absorptive and the internal scattering, Equation 2.23e, contibution is negligible. Equation 2.25 is applied to each of the rays and the absorption and scattering intensities are calculated by assuming the sample comprises many layers, each with different index of refraction and absorption coefficient. These parameters are continuously updated for each time step according to the heating within each node which allows for a continuous change in index of refraction and absorption coefficient throughout the sample. The scattering is calculated by the reflections at each node-to-node interface. The absorbed energy in each node is determined by the ray's path length through the node which is determined by the refraction of the ray at each node interface as explained in Section 2.6.

The geometry of this is depicted in Figure 2.7. This figure is shown for rays one through six as the beam propagates through the sample along the z-axis. The vertical axis is the x-axis and due to the beam symmetry, this figure would appear the same for the y verse z plot. Ray one is the lower-most ray starting on the left side, $z = 0$, and the ray numbers increment along x sequentially to ray number six located at the sixth node from ray one. Here it is seen that the source beam converges to a spot near the center of the sample.

The figure also illustrates the node geometry and how each ray starts in the center of it's respective node within the irradiated area. The ray trace model is discussed in Section 2.6 which will elaborate upon the propagation of the rays.

The index of refraction of the material causes the incident rays to refract and will

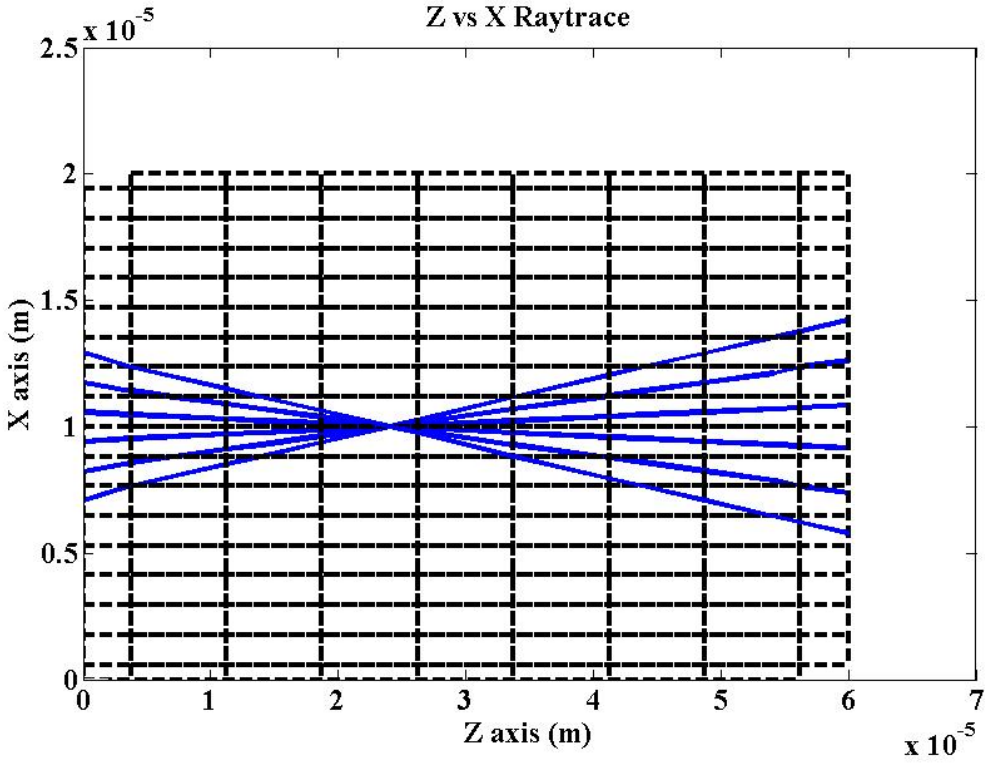

Figure 2.7: Geometry of Rays at $t = 0$ as They Propagate Through the Sample.

result in a focal point that is further into the sample then desired. To achieve a focal length of 16 mm in air, for a sample with index of refraction of 1.4, the focus must be modified in "pre_txt" to 15.99142e-3 m as seen in Tables 2.1 and 2.8. Figure 2.8 shows an example of this.

The parameter $zlsl$ is defined in "pre_txt" to be the distance from the lens to the sample, 15.97e-3 m, f is the desired focal length, 16 mm, and f_l is the corrected focal length determined by solving

$$f = n\,(f_l - zlsl) + zlsl \tag{2.26}$$

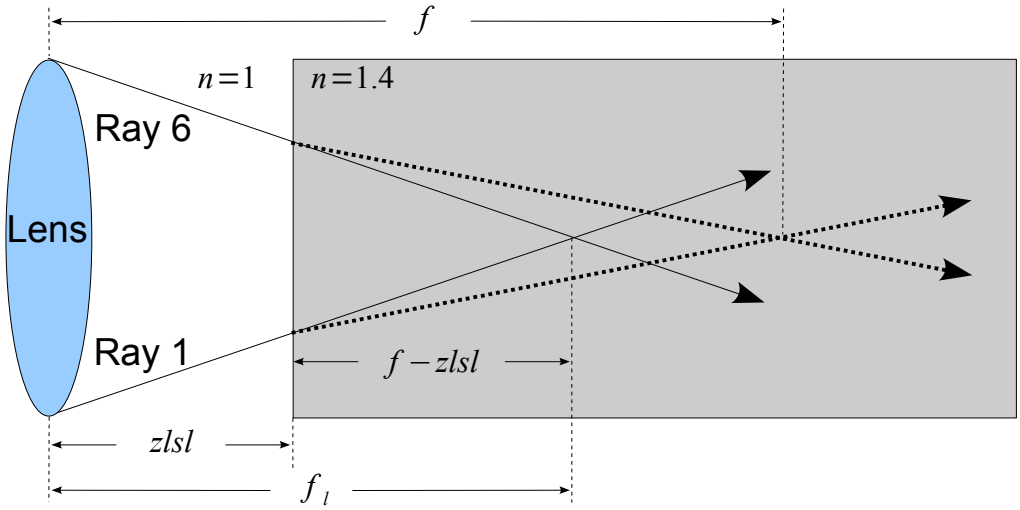

Figure 2.8: Ray Refraction at Meduim.

for f_l. The resultant value is f_l =15.99142e-3 m, as seen in Tables 2.1 and 2.8.

2.5 Index of Refraction

The index of refraction of a material is defined, in optics, by the ratio of the speed of light in a vacuum to that in a material according to

$$n = \frac{c}{v} = \sqrt{\frac{\epsilon\mu}{\epsilon_0\mu_0}} \tag{2.27}$$

where n is the index of refraction, c is the speed of light in vacuum, v is the speed of light in the material, ϵ is the permittivity of the material, μ is the permeability of the material and ϵ_0 and μ_0 are the permittivity and permeability of free space, respectively. In cases involving the short wavelengths associated with light, including

this research, the permeability of the material is equal to that of free space, $\mu = \mu_0$ [6]. The expression for the index of refraction is written in terms of the permittivity as

$$n = \sqrt{\frac{\epsilon}{\epsilon_0}}. \tag{2.28}$$

The index of refraction determines how the light entering the material, for this research, a Gaussian laser beam, bends as it crosses the boundary between one medium and another. This is described by Snell's law

$$\frac{\sin\theta_1}{\sin\theta_2} = \frac{n_2}{n_1} \tag{2.29}$$

where θ_1, n_1 are for medium 1 and θ_2, n_2 are for medium 2. Knowing the angle of incidence on a material and the index of refraction of each material the light traverses, the angle to which the light is refracted can be calculated with this relationship.

When a material undergoes changes to its temperature or pressure, the index of refraction of the material will change. This means that over time, with a heating source applied to the material, both the speed of light and the angle at which the incident rays of light are refracted at the interface between the two media will change. These changes are fundamental to obtaining an accurate optical phase calculation for scattering particles in a material; heating causes a change in refractive index which in return, causes a change in the OPL of the ray. The OPL comprises two parts; a displacement-dependent component that changes according to the nodal displacement due to the heating and an index–dependent component that changes as the index of refraction changes. These are discussed further in Sections 3.2.1 and 3.3, respectively.

It is critical to know how each ray is traveling through the tissue at each time step and how the OPL is affected. This will be discussed further in Chapter 3.

The formulation used for the calculation of the change in index of refraction over time under heating is based upon the Lorentz-Lorenz formula as denoted by

$$n = \sqrt{\frac{C_0 + v_{sp}}{v_{sp} - C_0}} \tag{2.30}$$

where v_{sp} is the specific volume and C_0 is according to Equation 2.32. The change in index of refraction is related to the temperature and pressure variations in the material according to Kowalski [23] by combining Equation 2.30 with the differential equation of state for liquids and solids

$$\mathrm{d}v_{sp} = \beta v_{sp}\,\mathrm{d}T - \kappa v_{sp}\,\mathrm{d}p \tag{2.31}$$

which relates the volumetric coefficient of expansion, β, with the isothermal compressibility factor, κ. Keeping the pressure, p, constant and solving Equation 2.31 for v_{sp} then combining it with

$$C_0 = v_0 \frac{n_0^2 - 1}{n_0^2 + 1} \tag{2.32}$$

where $v_0 = 1.00786 \times 10^{-3}\ \frac{\mathrm{m}^3}{\mathrm{kg}}$ is the parameter input into "pre_txt" , Line 8, column one, for the specific volume of water, yields

$$n = \sqrt{\frac{C_0 + v_0 e^{[\beta(T-T_0)]}}{v_0 e^{[\beta(T-T_0)]} - C_0}} \tag{2.33}$$

Similarly, if temperature is held constant Equation 2.30 becomes

$$n = \sqrt{\frac{C_0 + v_0 e^{[\kappa(p_0-p)]}}{v_0 e^{[\kappa(p_0-p)]} - C_0}}. \tag{2.34}$$

Solving Equation 2.31 for both temperature and pressure variations the final expression for the change in index of refraction is obtained as

$$n = \sqrt{\frac{C_0 + v_0 e^{[\beta(T-T_0)+\kappa(p_0-p)]}}{v_0 e^{[\beta(T-T_0)+\kappa(p_0-p)]} - C_0}}. \tag{2.35}$$

The value for β was chosen, for water, to be 207×10^{-6} $\frac{1}{\mathrm{K}}$, "pre_txt" Line 6, column two. Similarly, the value for κ, chosen for water to be 4.54×10^{-10} $\frac{1}{\mathrm{Pa}}$, can be found on Line 8, column 4 of "pre_txt". These values are tabulated from

$$\beta = \frac{1}{V}\left(\frac{\partial V}{\partial T}\right)_p \tag{2.36a}$$

$$\kappa = -\frac{1}{V}\left(\frac{\partial V}{\partial p}\right)_T \tag{2.36b}$$

where V is the volume.

The value for the index of refraction is updated as the main processor runs the predictor-corrector algorithm for each refraction step through the material.

2.6 Refraction and Raytrace Model

The refraction and raytrace model builds upon the radiation model of Section 2.4 by applying the calculation for the index of refraction due to heating, Section 2.5, through the wave model described by Maxwell's equations. Maxwell's equations are discussed in any introductory text, for example, the book *Advanced Engineering Electromagnetics* by C. A. Balanis [29], and are, for the general case

$$\nabla \times \mathbf{E} = \frac{\partial \mathbf{B}}{\partial t} \tag{2.37a}$$

$$\nabla \times \mathbf{H} = \frac{\partial \mathbf{D}}{\partial t} + \mathbf{J} \tag{2.37b}$$

$$\nabla \cdot \mathbf{D} = \rho_c \tag{2.37c}$$

$$\nabla \cdot \mathbf{B} = 0 \tag{2.37d}$$

where $\mathbf{E} = E(x, y, z, t)$ is the electric field, $\mathbf{H} = H(x, y, z, t)$ is the magnetic field, $\mathbf{D} = \epsilon \mathbf{E}$ is the electric displacement vector, $\mathbf{B} = \mu \mathbf{H}$ is the magnetic flux density, ρ_c is the charge density, assumed to be zero and $\mathbf{J}$ is the source-current density, also assumed to be zero. Maxwell's equations can be written in the harmonic form by substitution of $j\omega$ for the time derivative, $\frac{\partial}{\partial t}$, resulting in

$$\nabla \times \mathbf{E} = j\omega \mathbf{B} \tag{2.38a}$$

$$\nabla \times \mathbf{H} = j\omega \mathbf{D} \tag{2.38b}$$

where $j = \sqrt{-1}$.

As the rays enter each node from the air surrounding the sample at the irradiated surface, part of each ray's field amplitude is transmitted and part is reflected. The transmitted portion of the field is refracted due to the index of refraction defined in it's initial state in Table 2.1 and "pre_txt" on Line 10, column one. This value continuously changes for the duration of the simulation time on a node-by-node basis because of the non-uniform heating. The portion of reflected field is described by

$$\Gamma = \left[\frac{n_1 - n_0}{n_1 + n_0}\right] \tag{2.39}$$

which, in terms of the electric field, gives the relation

$$\mathbf{E_r} = \Gamma \mathbf{E_i} \tag{2.40}$$

where $\mathbf{E_r}$ is the reflected portion and $\mathbf{E_i}$ is the incident field on the surface interface. Maxwell's equations are solved for each node to obtain the reflection coefficient at the incident interface, then that value is used to calculate the respective intensity. This is outlined in matrix form by Kowalski *et al.* [20] and will be summarized here. For the n^{th} node the relationship is defined by

$$\mathbf{E_{n-1}} = \mathbf{E_n}\left[E_1 + jE_2\right] \tag{2.41a}$$

$$\mathbf{H_{n-1}} = \mathbf{H_n}\left[H_1 + jH_2\right] \tag{2.41b}$$

$$
\begin{aligned}
E_1 &= \cos\left(k_n N_n \Delta z_n \cos\theta_{c_n}\right) \\
E_2 &= b_n \sin\left(k_n N_n \Delta z_n \cos\theta_{c_n}\right) \\
H_1 &= \cos\left(k_n N_n \Delta z_n \cos\theta_{c_n}\right) \\
H_2 &= \frac{\sin\left(k_n N_n \Delta z_n \cos\theta_{c_n}\right)}{b_n} \\
b_n &= \frac{N_n \cos\theta_{c_n}}{\mu_n c},\ for\ TE \\
b_n &= \frac{N_n}{\cos\theta_{c_n}\mu_n c},\ for\ TM \\
N_n &= n + j\kappa_{ext} \\
k_n &= \frac{2\pi}{\lambda}\sqrt{\epsilon_n \mu_n}
\end{aligned}
$$

where κ_{ext} is the extinction coefficient, $k = \frac{2\pi}{\lambda}$ is the wave number, θ_{c_n} is the complex angle of incidence, TE is the transverse electric mode defined as having electric field only in the directions transverse to the surface and TM is the transverse magnetic mode defined as having magnetic field only in the directions transverse to the surface. It should be noted that the subscript, n, refers to an arbitrary node and should be differentiated from the index of refraction. This subscript notation will be used from here on unless indicated otherwise. By defining the parameters b_{inc} to be b_n evaluated with the properties of the adjacent material at the incident interface of the node volume, b_{exit} to be b_n evaluated with the properties of the adjacent material at the exit interface of the node volume [20], the calculation for the reflection coefficient can be made according to

$$\Gamma_n = \frac{b_{inc}\left(E_1 + b_{exit}E_2\right) - \left(b_{exit}H_1 + H_2\right)}{b_{inc}\left(E_1 + b_{exit}E_2\right) + \left(b_{exit}H_1 + H_2\right)} \tag{2.42}$$

From this value, the reflected irradiance can be calculated as

$$\Gamma_{I,n} = \left|\Gamma_n\right|^2 . \tag{2.43}$$

Following this calculation, application of the radiative transport equation, Equation 2.25, yields the transmitted irradiance by taking the scattered radiation to be the reflected irradiance.

The code allows for the internal reflections to be switched off using Line 18 of "pre_txt", and for this research they were. The heating duration is small and the sample is homogeneous throughout so that change over time due to the laser's absorption causes negligible reflection between nodes and at the surfaces is 0.0278. This is an acceptable loss for the purpose of this research when weighed against the cost of potential error in post-processing analysis by accounting for these reflections and managing the resultant additional data from these calculations. The code allows for five reflection settings as shown in Appendix A for no reflections, surface only reflections, incident surface only reflections, internal reflections and all reflections. Using the reflection switch to account for reflections within the system is more desirable with samples comprising multiple layers of different material properties.

As the rays propagate through the sample each node interface is treated as a new layer with it's own absorption and index of refraction, calculated per Section 2.5. This allows the computational model to be extended to cases with multiple layers

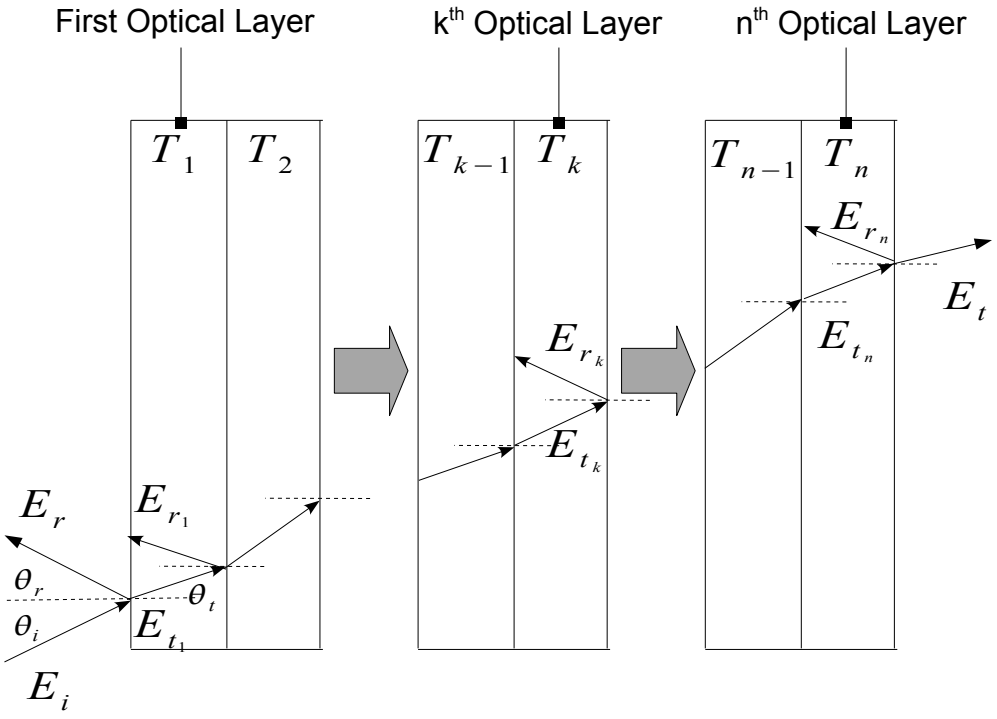

Figure 2.9: Example of a Multilayer System with Incident, Reflected and Transmitted Fields for Layers with Different Temperatures.

with different properties. The ray is traced until it emerges at the back plane of the sample and continues into free space. This is shown in Figure 2.9. E_i is the incident field, E_r is the reflected field, where additional subscripts represent the respective layer, E_t is the transmitted field with the same subscript notation, $\theta_i, \theta_r, \theta_t$ are the angles of incidence, reflection and transmission, respectively and T represents the temperature in each layer.

When the index of refraction is a smoothly varying function, it is useful to calculate the ray's trajectories by the ray equation [6]

$$\frac{\partial}{\partial \ell}\left[n\left(\mathbf{r}\right)\frac{\partial \mathbf{r}}{\partial \ell}\right] = \nabla n\left(\mathbf{r}\right) \tag{2.44}$$

.

This equation can then be expanded using the product rule for differentiation as

$$n\left(\mathbf{r}\right)\frac{\partial^2 \mathbf{r}}{d\ell^2} = \nabla n\left(\mathbf{r}\right) - \frac{\partial \mathbf{r}}{\ell}\frac{\partial n\left(\mathbf{r}\right)}{\partial \ell}. \tag{2.45}$$

Where $\mathbf{r} = \hat{i}x + \hat{j}y + \hat{k}z$ is the position vector, and ℓ is the length along the ray. The equation can be reduced to six scaler differential equations that can be solved numerically using Equation 2.6. This solution gives the complete information regarding each ray's position and direction throughout the system, which allows for a calculation of the ray's path length through the system.

This solution is obtained for small steps the ray takes through the system. These steps are much smaller then the node sizes to preserve accuracy in the numerical model. The total path length change of the ray is obtained by integrating along the ray, which becomes the change in OPL due to the change of index of refraction from the heating. Numerically, this translates to summing the values obtained at each step through the system by Equation 2.45.

$$\Delta L = OPL = \int_{\ell} n \, \mathrm{d}\ell \tag{2.46}$$

This is discussed in detail in Chapter 3 since the OPL is a component in the optical phase calculation of the scattering particles. The step size is defined in "pre_txt" on

Line 27 and is referred to as the refractive step. If a refractive step size is defined that is not small enough then the pre-processor takes the square root of smallest node length in z and defines that as the refractive step length. The smaller the refractive step is, the more accurately the ray is traced through the system, but smaller steps cause more iterations of the refraction and raytrace model which requires more processor usage and longer run times on the computer.

2.7 Boundary Conditions

The boundary conditions chosen for this research represent a convective condition and are applied only in the z direction at $z = 0$ and $z = L_z$, where L_z is the $z = 60$ μm face of the sample. This section will provide a brief description of the methodology used to determined the numbers seen in Table 2.1; Line 28, columns one and two of "pre_txt".

The system defined assumes the $x - y$ plane to be semi-infinite. This means that for all $z = 0$,

$$\left(\frac{\partial T}{\partial x}\right)_{x=0} = \left(\frac{\partial T}{\partial y}\right)_{y=0} = 0 \tag{2.47a}$$

$$\left(\frac{\partial T}{\partial x}\right)_{x=L_x} = \left(\frac{\partial T}{\partial y}\right)_{y=L_y} = 0 \tag{2.47b}$$

The irradiated area is located in the center of the system and over the 5 μs pulse duration, essentially, no temperature change is seen along the $\pm x$ or $\pm y$ faces. Figure 2.10 shows the temperature gradient at the layer of the sample where the focus

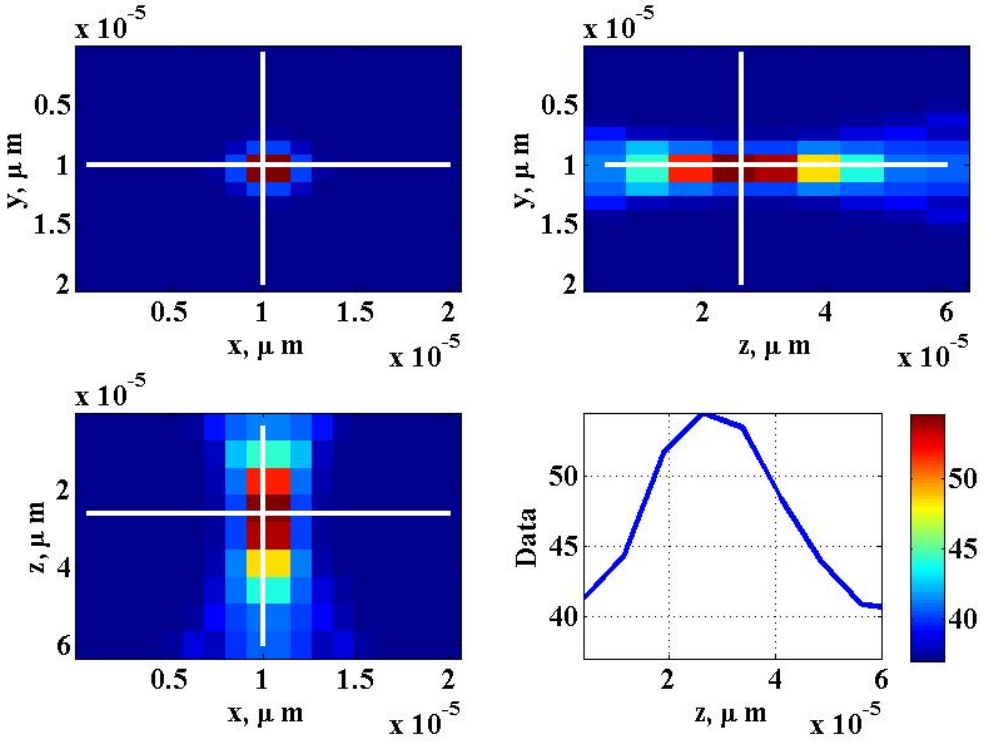

Figure 2.10: Temperature Gradient for $z \approx 26$ μm at $t = 5$ μs.

is located, $z \approx 26$ μm for the last time step when $t = 5$ μs.

It can be seen from this figure that the heating remains concentrated to a small area around the center of the system and that the $\pm x$ and $\pm y$ faces remain at the initial ambient temperature, 37 °C.

In the z direction, however, this is not true. Figure 2.10 shows that there is heating at the $z = 0$ face and the $z = L_z$ face where L_z =60 μm.

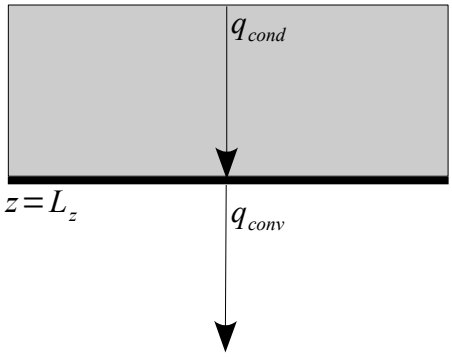

Figure 2.11: Conduction and Convection at the $z = L_z$ Surface.

This requires boundary conditions on the z-faces. To establish these boundary conditions, considerations must be taken regarding the geometry of the system. Because of the small size of the sample 20 μm×20 μm×60 μm and the short heating time, $t = 5$ μs, the heating is of a convection nature. Referencing Figure 2.11 it can be seen that

$$q_{cond} = q_{conv} \tag{2.48}$$

where q_{cond} is the energy conducted and q_{conv} is the energy convected at the $z = L_z$ face. The reason for choosing this orientation is to preserve the positive sign on q_{cond}. This is represented by the modification to Equation 2.10,

$$\left.\frac{\partial T}{\partial z}\right|_{z=L_z} = -\frac{h}{K_t}\left(T_{Lz} - T_0\right) \tag{2.49}$$

Because this is a small system that is convective, but near the conductive limit, h can be computed from the relationship below for the Nusselt Number, Nu,

$$Nu = \frac{h\Delta}{K_{air}} = 2, \tag{2.50}$$

where Δ is the characteristic length, K_{air} is the conductivity of air and 2 is known to be a reasonable value for a system that is convective near the conduction limit. For this system, $\Delta = 2w(z) = 10.22$ μm, the spot size at the surface according to Equation 2.19 where $z \approx 26$ μm and $K_{air} \approx 0.024$ $\frac{\mathrm{W}}{\mathrm{m \cdot K}}$. The value for $h_{z=0}$ is 4695.67 $\frac{\mathrm{W}}{\mathrm{m^2 \cdot K}}$.

Applying a spherical conduction at the $z = L_z$ face using the material's conductivity, K_t, according to

$$h_{z_L} = \frac{K_t}{\Delta} \tag{2.51}$$

yields a value for h_{z_L} of 56739.32 $\frac{\mathrm{W}}{\mathrm{m^2 \cdot K}}$. Inputting both of these into "pre_txt" on Line 28 and running the Fortran pre-processor and main processor produces the temperature gradient shown in Figure 2.12.

It can be seen that the temperature at the $z = 0$ and $z = L_z$ boundaries are the same as in Figure 2.10. Any values greater than the previously calculated limits would be unreasonable and unrealistic, and since no change in temperature at the z boundaries is observed, it is justified to choose any value less then these limit values for the $z = 0$ and $z = L_z$ boundaries as can be seen by Line 28 of "pre_txt".

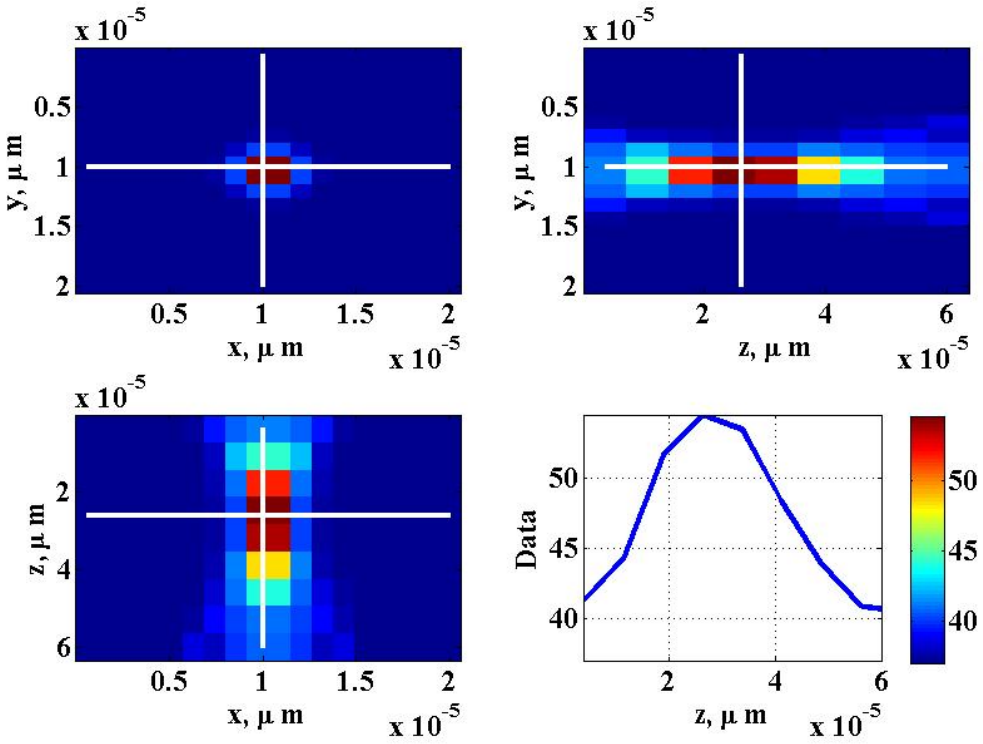

Figure 2.12: Temperature Gradient for $z \approx 26$ μm at $t = 5\mu$ s. Boundary condition at $z = 0$ is 4695.67 $\frac{\mathrm{W}}{\mathrm{m}^2 \cdot \mathrm{K}}$ and at $z = L_z$ is 56739.32 $\frac{\mathrm{W}}{\mathrm{m}^2 \cdot \mathrm{K}}$.

Chapter 3

Phase Amplitude Analysis

The post–processor comprises two stages. The first stage is the thermal stress and local displacement calculation discussed in Section 3.1. The second stage is the calculation of the optical phase and amplitude covered in Section 3.3. Figure 3.1 depicts the flow of the code into the post–processor as a modification to Figure 2.1 with everything except the post–processor shaded out. Additionally, the output files generated in the post–processor are listed in Table 3.1. For this analysis, as can be seen in the figure, both Fortran and MATLAB were used for post–processing.

The thermal stress calculation was an existing Fortran code developed to accompany the main processor. Using the stresses calculated by the code, further calculations could be made for the displacement within each node volume based on Hooke's law, Sections 3.1.1, 3.1.2 and 3.1.3. Additional MATLAB code was developed to calculate the integrated displacement, sum of local displacements, along the x, y and z directions for each node in the system.

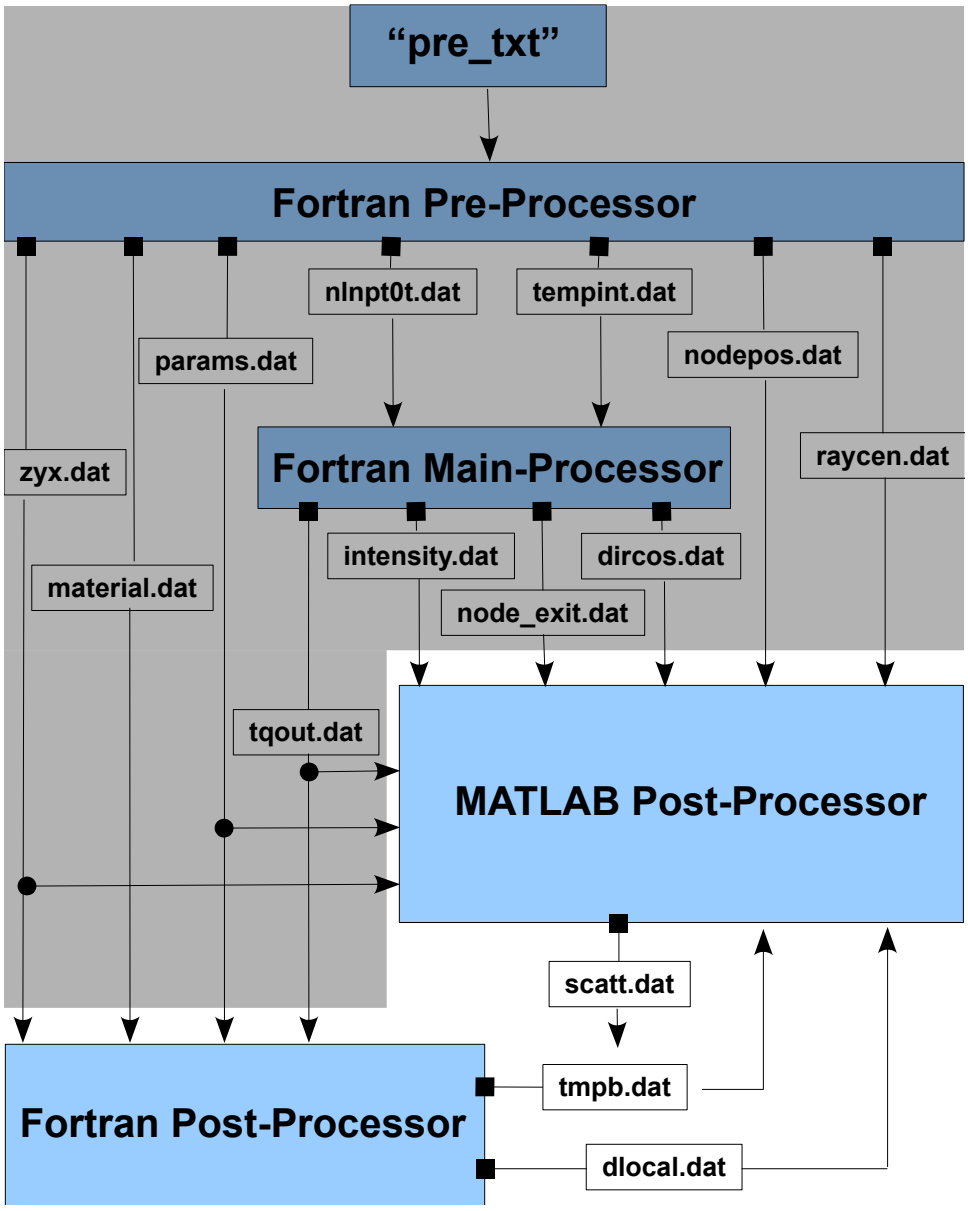

Figure 3.1: Flow Diagram of the Code with Emphasis on the Post–Processor.

"tmpb.dat"	This file contains all the temperature data for each node at one time step of interest. It is used in the Fortran and MATLAB post–processors.
"dlocal.dat"	This file contains the displacements for each node based on the thermal stress analysis performed by the Fortran post–processor. It is used in the MATLAB post–processor.
"scatt.dat"	This file contains the scattering particles locations for subsequent runs of the MATLAB post–processor.

Table 3.1: Output Files Generated by the Post–processor.

Once the integrated displacement was calculated several interpolation algorithms were developed to calculate the displacement, OPL and physical path length (PPL) at randomly placed scattering particles within each node volume through which the source beam passes. These parameters were then used to calculate the optical phase due to the displacement, the optical phase due to the temperature dependent index of refraction and the total optical phase due to both phenomena. These are discussed in Section 3.3 and the results are discussed in Chapter 4.

3.1 Thermal Stress and Displacement

The first stage of the post–processing analysis is performed through using a thermal stress code written in Fortran. The code calculates the normal and shear stresses applied on each node for each coordinate direction. Using the normal stresses, and application of Hooke's law, the thermal displacements can be found locally for each node in the system. This is discussed in the following sections.

The second stage uses MATLAB to import a file created by the Fortran post–processor, 'dlocal.dat', to apply an algorithm, discussed in Section 3.1.3, to calculate the displacement of each node. The file, 'dlocal.dat' contains the displacement due to the temperature and stress found locally at each node and the MATLAB script is used to calculate a global displacement; an integration along each coordinate axes.

3.1.1 Discussion of Thermal Stress and the Young's Modulus

The effect of non–uniform heating, such as that observed in the sample studied by this research, introduces stresses into the material, for this case, tissue. Each node that the source beam traverses is heated by the absorbed energy of the source by Equation 2.25. The absorption coefficient, α_r , of the material is found on Line 6 of "pre_txt", shown in Table 2.1 with a value 1759 $\frac{\mathrm{W}}{\mathrm{m}^2}$ for tissue at 1500 nm [30], [31] and [32].

The tissue starts in an initial state (undeformed) as a rectangular cube of dimensions 20 μm x 20 μm x 60 μm with 18 x 18 x 9 nodes and a temperature of 37 °C. When the laser is turned on and focused near the center, the nodes at the focus begin to heat more rapidly due the the larger amount of energy there. With the laser source stationary, over time, the heat slowly diffuses to the surrounding nodes outside of the beam path. These also start to heat, but at a slower rate. The heating of each node causes a local expansion to occur. This expansion within the nodes near the focus is restrained by the cooler nodes surrounding the focus, and the still cooler nodes towards the surface of the tissue which is still at 37 °C.

The pulse time of the laser source is short enough so that the surface never reaches

a temperature above 37 °C and thus the heating produces negligible expansion at this location. This situation introduces stresses into the more central nodes as they try to expand and are restrained by the surface nodes. The surface nodes act as a compressive force opposing the expansion force of the central nodes. If the source pulse duration were increased, the tissue would deform from it's cubic geometry and the surfaces would become more parabolic as the heated region at the center expanded outward.

The general state of stress is defined by normal stresses, σ_x, σ_y and σ_z which act on a plane normal to the axis given by the subscript and shear stresses, $\tau_{xy}, \tau_{xz}, \tau_{yx}, \tau_{yz}, \tau_{zx}$ and τ_{zy}. The shear stresses act upon a plane normal to the first subscript in the direction of the second subscript. For static equilibrium,

$$\tau_{xy} = \tau_{yx} \qquad \tau_{xz} = \tau_{zx} \qquad \tau_{yz} = \tau_{zy}$$

which results in a complete definition of stress [33],

$$\sigma = \begin{Bmatrix} \sigma_x & \sigma_y & \sigma_z \\ \\ \tau_{xy} & \tau_{xz} & \tau_{yz} \end{Bmatrix}. \tag{3.1}$$

Similarly, the strain of a material, represented by ε, can be described as

$$\varepsilon = \left\{ \begin{array}{ccc} & & \\ \varepsilon_x & \varepsilon_y & \varepsilon_z \\ & & \\ & & \\ \gamma_{xy} & \gamma_{xz} & \gamma_{yz} \end{array} \right\} \tag{3.2}$$

where γ represents the shear strains which hold the same subscript notation as the shear stresses. The strain is defined as the ratio of the change in length over the total length, $\frac{\Delta L}{L}$, of a material under stress.

In the elastic region, where only small displacements are observed, the relationship between stress and the strain that is produced is linear and proportional to the Young's Modulus of the material, E_m. The Young's Modulus is a measure of the elasticity of the material and is often referred to as the elastic modulus. It is defined by

$$E_m = \frac{\sigma}{\varepsilon}. \tag{3.3}$$

Young's Modulus is found experimentally and varies for tissue depending on the location of the sample, the type of sample, muscle contraction [34] and the age of the person from which the sample was measured [35]. The common method employed is ultrasound indentation, however, accurate numerical estimation has been proven a valid method for determining the elasticity of tissue. The expression to predict the Young's Modulus, according to rigorous mathematical formulation performed by Hayes *et al.* [36] is

$$E_m = \frac{(1-\nu^2)\,F_i}{2a\kappa_s\left(\nu, \frac{a}{h}\right)w} \tag{3.4}$$

where F_i is the indentation force, a is the radius of the indentation tool, w is the indentation depth, h is the thickness of the tissue and κ_s is a scaling factor that depends on the aspect ratio $\frac{a}{h}$ and the Poisson's ratio, ν. Poisson's ratio is the compressibility factor of the tissue according to

$$\nu = \frac{\varepsilon_{trans}}{\varepsilon_{axial}}. \tag{3.5}$$

The Poisson ratio varies from 0 to 0.5 for different materials where 0 is a completely compressible material and 0.5 is incompressible. Tissue tends towards the incompressible limit and is normally in a range from 0.3 to 0.5 [37]. From the values reasonable for Poisson's ratio, the Young's Modulus can be evaluated according to Equation 3.4. Experimental values for Young's Modulus were found to be between 14.0 $\pm$ 5.0 and 58.8 $\pm$ 1.7 kPa [34], and the theoretical mid–range value was estimated at 34.307 kPa [38]. The latter value is what was used in this research and input into "pre_txt" on Line 8, parameter 6 as seen in Table 2.1. Poisson's ratio, "pre_txt" Line 6, parameter 3, was chosen to be representative of a near incompressible material and was set to 0.495. This value was based upon results found via a Finite Element Method (FEM) analysis by Palmeri *et al.* [39].

3.1.2 Thermal Stress Calculation

The thermal stress post–processor, developed by Kowalski [23, 40], uses a finite difference method on the computational three dimensional grid of nodes to calculate the thermal stress at each node center location using the thermoelastic potential. The stress distribution of the system is resultant only of the thermal stress since the isothermal mechanical stress at the boundaries is zero. The justification for this arises from the irradiated area being much smaller then the dimensions of the system.

Before this analysis can be executed, an intermediate post–processing step must be performed to acquire the appropriate temperatures at each node volume for the corresponding time step of interest. This requires a separate script that divides an output file, 'tqout.dat', produced by the main processor that contains temperature data for all nodes at all time steps, into a smaller file, 'tmpb.dat'. This smaller temperature file contains the nodal temperatures for only the time step of interest. It limits the efficiency of the post–processing as each time step to be analyzed must be run separately through these two post–processors. Once this new file is created the thermal stress post–processor can be executed to produce the normal and shear stresses and thermal displacements for each node. The thermal displacements will be discussed in 3.1.3.

To calculate the thermal stress, a thermoelastic potential is created, according to Timoshenko [41]

$$\nabla^2 \Psi = \frac{1+\nu}{1-\nu} \alpha T\left(x, y, z, t\right) \tag{3.6}$$

which has the solution

$$\Psi = -\frac{(1+\nu)\,\alpha}{4\pi\,(1-\nu)} \iiint T\,(\xi,\eta,\zeta)\,\frac{1}{r'}\,\mathrm{d}\xi\,\mathrm{d}\eta\,\mathrm{d}\zeta \tag{3.7}$$

where $T\,(\xi,\eta,\zeta)$ is the temperature at a point ξ,η,ζ where there is an element of volume $\mathrm{d}\xi$, $\mathrm{d}\eta$, $\mathrm{d}\zeta$ and r' is the distance between this point and a point x,y,z according to

$$r' = \left[(x-\xi)^2 + (y-\eta)^2 + (z-\zeta)^2\right]^{\frac{1}{2}}. \tag{3.8}$$

The limits of integration are the dimensions of the model; for instance, for the z direction the integration would be from $z = 0$ to $z = 60$ μm. The integration of Equation 3.7 is performed numerically using the three dimensional nodal system previously defined. Equation 3.7 is reduced to a summation of integrals over the node volume of interest then repeated for each node in the system. Each integral is approximated by assuming the temperature to be constant throughout the entire node volume and equal to the calculated node temperature found in the file 'tmpb.dat'. The expression for this is:

$$\Psi\,(x_i,y_i,z_i) = -\alpha\left(\frac{1+\nu}{1-\nu}\right)\sum_N T_N\,(\xi_N,\eta_N,\zeta_N)\,\frac{1}{r'_{N,i}}\Delta\xi_N\Delta\eta_N\Delta\zeta_N \tag{3.9}$$

$$r'_{N,i} = r' = \left[(x_i-\xi_N)^2 + (y_i-\eta_N)^2 + (z_i-\zeta_N)^2\right]^{\frac{1}{2}}. \tag{3.10}$$

For the case where $N = i$, $r'_{N,i}$ goes to zero and Equation 3.9 becomes infinite. The singular point is the result of the numerical integration and can be eliminated by approximating the volume of the node as a sphere [23]. The sphere is assumed to have constant temperature and an effective radius of

$$r_{eff} = \left[\left(\frac{3\pi}{4} \right) V_i \right]^{\frac{1}{3}} \tag{3.11}$$

where V_i is the node volume and the resultant numerical potential for the node volume is

$$\Psi \left(x_i, y_i, z_i \right) = \frac{4\pi}{3} r_{eff}^2 T_N \left(\xi_N, \eta_N, \zeta_N \right); \qquad N = i. \tag{3.12}$$

It is important to understand the model geometry for the calculation of V_i. As discussed in Section 2.2, the volume of a node is dependent on the location of the node within the model geometry. Nodes located at a corner have volumes equal to one eighth of the expected node volume given by $\Delta x \times \Delta y \times \Delta z$. Nodes located at an edge, at interfaces of two surfaces, have volumes equal to one quarter of this expected volume, and nodes located on the surface have volumes equal to one half of this. The reason for this was explained in Section 2.2.

The normal thermal stresses are related to the elastic potential, [23, 41], according to

$$\sigma_x = -\frac{E_m}{1+\nu}\left[\frac{\partial^2\Psi}{\partial y^2} + \frac{\partial^2\Psi}{\partial z^2}\right] \tag{3.13a}$$

$$\sigma_y = -\frac{E_m}{1+\nu}\left[\frac{\partial^2\Psi}{\partial x^2} + \frac{\partial^2\Psi}{\partial z^2}\right] \tag{3.13b}$$

$$\sigma_z = -\frac{E_m}{1+\nu}\left[\frac{\partial^2\Psi}{\partial y^2} + \frac{\partial^2\Psi}{\partial x^2}\right]. \tag{3.13c}$$

Similarly, the shear stresses are found according to

$$\tau_{xy} = -\frac{E_m}{1+\nu}\left[\frac{\partial^2\Psi}{\partial x \partial y}\right] \tag{3.14a}$$

$$\tau_{xz} = -\frac{E_m}{1+\nu}\left[\frac{\partial^2\Psi}{\partial x \partial z}\right] \tag{3.14b}$$

$$\tau_{yz} = -\frac{E_m}{1+\nu}\left[\frac{\partial^2\Psi}{\partial y \partial z}\right] \tag{3.14c}$$

where the subscript notation is according to Section 3.1.1. A finite difference method is employed using Equations 3.13, 3.14 in the post–processor to calculate the stress at each node in the model. Each partial derivative in the above expressions is put into it's discretized form through application of Equation 2.6 and then is performed for each node volume.

Once the stresses are calculated, they are saved to files 'nstress.dat' and 'sstress.dat' for any further post–processing analysis. The values for the normal stresses are then applied by Hooke's law to calculate the thermal displacement which will be discussed in 3.1.3.

3.1.3 Thermal Displacement

The thermal displacement is handled in two parts using both languages, Fortran and MATLAB:

1. The local displacement within each node from the temperature of the node and the normal stresses introduced into the node is calculated by the Fortran post–processor for thermal stress.

2. The global displacement as the integrated local displacement along each of the coordinate axes from (0,0,0) to the node of interest is calculated in MATLAB from the results of the Fortran post–processor for thermal stress.

Hooke's law provides a relationship between the stress and strain on a material. This concept applies similarly to thermally induced stress and strain as well as that which is achieved by direct mechanical means. The Hooke's Stress/Strain Module is that seen in Equation 3.3 as a general case. In three dimensions, for linearly elastic, homogeneous and isotropic materials, Equation 3.3 becomes

$$\varepsilon_x = \frac{\sigma_x - \nu\left(\sigma_y + \sigma_z\right)}{E_m}; \quad \gamma_{xy} = \frac{2\tau_{xy}\left(1+\nu\right)}{E_m} \tag{3.15a}$$

$$\varepsilon_y = \frac{\sigma_x - \nu\left(\sigma_z + \sigma_z\right)}{E_m}; \quad \gamma_{xz} = \frac{2\tau_{xz}\left(1+\nu\right)}{E_m} \tag{3.15b}$$

$$\varepsilon_z = \frac{\sigma_y - \nu\left(\sigma_z + \sigma_z\right)}{E_m}; \quad \gamma_{yz} = \frac{2\tau_{yz}\left(1+\nu\right)}{E_m}, \tag{3.15c}$$

where $\sigma_x, \sigma_y \; and \; \sigma_z$ are functions of x, y and z. A change in temperature applied to an unconstrained, three dimensional elastic element, such as tissue, causes an expansion

or contraction of the element. The free (unconstrained) thermal expansion in return produces normal strains according to

$$\varepsilon = \alpha \Delta T \tag{3.16}$$

where ΔT is the change in temperature, for this case, between the initial temperature, $T_0 = 37\,^{\circ}\mathrm{C}$ and the current nodal temperature from 'tmpb.dat'. Using Equation 3.15 and superposition the expression for the total strain can be found:

$$\varepsilon_x = \frac{\sigma_x - \nu\left(\sigma_y + \sigma_z\right)}{E_m} + \alpha \Delta T \tag{3.17a}$$

$$\varepsilon_y = \frac{\sigma_x - \nu\left(\sigma_z + \sigma_z\right)}{E_m} + \alpha \Delta T \tag{3.17b}$$

$$\varepsilon_z = \frac{\sigma_y - \nu\left(\sigma_z + \sigma_z\right)}{E_m} + \alpha \Delta T. \tag{3.17c}$$

According to the definition of strain,

$$\varepsilon = \frac{\Delta L}{L}, \tag{3.18}$$

the model can be broken down into three similar relationships

$$\varepsilon_x = \frac{\delta x}{\Delta x}, \quad \varepsilon_y = \frac{\delta y}{\Delta y}, \quad \varepsilon_z = \frac{\delta z}{\Delta z} \tag{3.19}$$

where δx represents the change in length of a node in the x–direction, Δx, the length of the node in the x–direction, and similarly for y and z. Substituting Equation 3.19 into Equation 3.17 produces the thermal displacement relationship dependent on the temperature, stresses and node geometry.

$$\delta x = \frac{\sigma_x - \nu\left(\sigma_y + \sigma_z\right)}{E_m}\Delta x + \alpha \Delta T \Delta x \tag{3.20a}$$

$$\delta y = \frac{\sigma_x - \nu\left(\sigma_z + \sigma_z\right)}{E_m}\Delta y + \alpha \Delta T \Delta y \tag{3.20b}$$

$$\delta z = \frac{\sigma_y - \nu\left(\sigma_z + \sigma_z\right)}{E_m}\Delta z + \alpha \Delta T \Delta z. \tag{3.20c}$$

As the temperatures are read from 'tmpb.dat' into the thermal stress post–processor, the $\alpha\Delta T$ is calculated for each node. The post–processor then performs the finite difference algorithm to calculate the thermal stresses according to Equations 3.13 and 3.14. Once complete, the superposition of displacements is calculated according to Equation 3.20 for each node to get each local displacement. Each $\alpha\Delta T$ is written to the file 'dlocal.dat' in sequential order for the respective time step of interest, then each local displacement is written. Once this is complete, the file can then be called from the MATLAB script to calculate the global displacement which is needed for the optical phase calculation for each randomly placed scattering particle. The full capability of the post–processing MATLAB script will be explained in Section 3.3, however, the portion devoted to calculating the global displacement is described here.

The data stored in 'dlocal.dat' is read into MATLAB and stored appropriately as arrays of size 1 x 2917, the total number of nodes including an ambient node (Node 1), for each coordinate direction. The algorithm accesses each array index starting

at index 2 and computes the cumulative sum along x, starting with nodes 2–19, since the node numbering is by x–direction, then y–direction, then z–direction. The volume is best visualized as rows of 18 nodes in the x–direction with 18 rows along the y–direction. Each $x - y$ grid comprises a slice in the z–direction and 324 nodes. To move from one y–row to another, 18 nodes must be added to the previous row's adjacent node and to move along z–slices, $18 \times 18 = 324$ nodes must be added to adjacent node on the previous slice. Define:

$$d = 2 + nx\,(j-1) + nx \cdot ny\,(k-1)\,, \quad e = k - nx\,(q-1)\,, \quad f = k - nx \cdot ny\,(p-1)$$

where nx, ny, nz are the node numbers in the x, y and z–directions, 18, 18 and 9, respectively, j increments along the y–rows, k is an iteration counter and increments from 1 to 29161 within the nested for–loops, q increments from 2 to 19 and p from 1 to k. Let dd increment from d to $d + nx - 1$, which represents the row of x–nodes. The reason for subtracting from k in the expression for e and f is because the node numbering starts at the last z–slice, the slice in z at z =60 μm. This algorithm is built into a nested for–loop that is four levels deep. The resultant summations are, according to Equation 3.21,

$$u_n = \sum_{dd} \delta x \tag{3.21a}$$

$$v_n = \sum_{e} \delta y \tag{3.21b}$$

$$w_n = \sum_{f} \delta z \tag{3.21c}$$

where n represents the node of interest, u_n, v_n and w_n are the global displacements for x, y and z at node n from the sum of the previous adjacent nodes starting at Node 2.

In formulation of the thermoelastic potential it is necessary to define the u_n, v_n and w_n parameters according to

$$u = \frac{\partial \Psi}{\partial x}, \quad v = \frac{\partial \Psi}{\partial y}, \quad w = \frac{\partial \Psi}{\partial z} \tag{3.22}$$

which satisfies Equation 3.7, as well as the general expression for stress illustrated by [41], which has been omitted for brevity.

3.2 Coherent Detection

Optical imaging presents difficulty in obtaining optical phase information from a sample. In photothermal microscopy, obtaining the optical phase information is essential to improve contrast and depth limited by out–of–plane scatter by tagging light from

the focus of the heating laser. To achieve this goal, this research applies the principles from Optical Quadrature, Section 3.2.1, with Doppler Laser Radar and Coherent Detection, 3.2.2, to measure the coherent superposition of the back scattered light waves.

The relationship of the field parameters of Maxwell's equations, $\mathbf{E}, \mathbf{D}, \mathbf{B}$ and $\mathbf{H}$ are linear, $\mathbf{D} = n^2\epsilon_0\mathbf{E}$ and at optical frequencies, $\mathbf{B} = \mu_0\mathbf{H}$ [6]. This results in the homogeneous wave equation

$$\nabla^2\mathbf{E} = \epsilon\mu\frac{\partial^2\mathbf{E}}{\partial^2 t} \tag{3.23}$$

being linear and $\mu = \mu_0$. Because of this linearity, linear superposition is possible. Linear superposition enables the product of any scaler and any solution of Equation 3.23 to be a solution as well as any sum of any solution to be a solution. A simple example of this is shown in Figure 3.2.

In this figure, a wave is incident from the left on a dielectric interface, represented by gray lines, from the left at 45 degrees. Some of the wave will be reflected downward and some will be transmitted through the interface with field, E_1. Similarly, another wave, represented by dashed black lines, is incident from above. Some will be reflected to the right as E_2 and some transmitted downward. This example does not show the refraction of the waves at the boundary. At the right boundary, the two waves are added with resultant field [6]

$$E = E_1 + E_2. \tag{3.24}$$

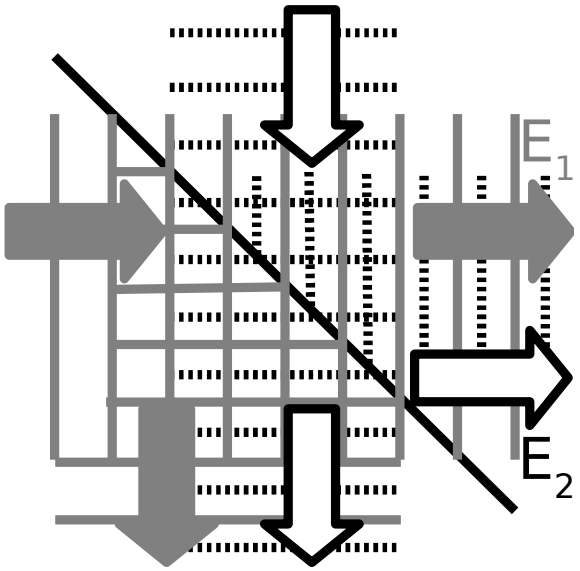

Figure 3.2: Coherent Addition of two Waves Incident on a 45 Degree Dielectric Interface.

The downward waves produce a similar result when they combine.

This example presents a significant challenge when the two waves are from different sources, and instead, it is common in most optical systems that use coherent addition to apply the approach in Figure 3.3. This assumes the same source is used to derive both beams. The source beam is split into two paths, one that sees mirror M1 and beamsplitter BS2, and the other that sees BS1, M1 and BS2 before both are recombined at BS2, called the recombining beamsplitter.

This configuration is referred to as the Mach–Zehnder Interferometer [13, 14] and will be discussed in Section 3.2.1. The Mach–Zehnder Interferometer, a conceptually simplistic model, will be expanded to Optical Quadrature Detection which can be applied to the Doppler Laser Radar in Section 3.2.2. The Doppler laser radar concept

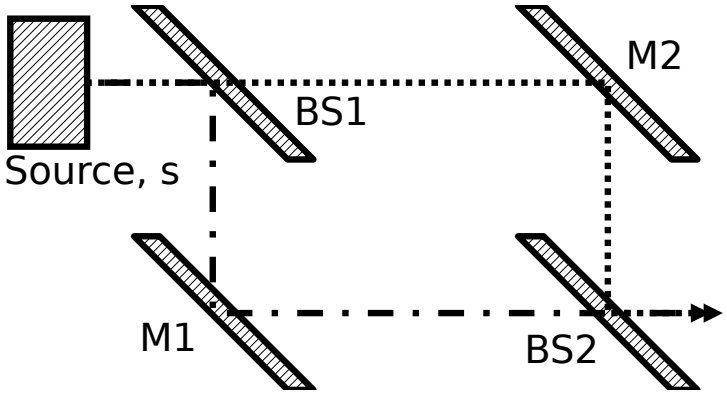

Figure 3.3: Coherent Addition of two Waves from the Same Source.

is implemented in the coherent confocal microscope to measure optical phase.

3.2.1 Optical Quadrature

The Mach–Zehnder Interferometer [13, 14] provides a useful tool for measuring the index of refraction of a material, or a material's length with known index of refraction. It also serves a good starting point for understanding coherent confocal microscopy. If a transparent, or partially transparent material with index of refraction, $n > 1$, were placed between M1 and BS2 according to Figure 3.4, it would cause the light wave to travel more slowly so that when the light recombines with the other wave its relative optical phase will have been affected by the material and this change can be measured.

In optics it is impossible to measure the electric field directly; only energy or power can be detected and then converted to electrical current that can be measured by a computer. The power on the detector, of known area A, relates to the the magnitude of the Poynting vector, or irradiance [6], and thus the electric field by

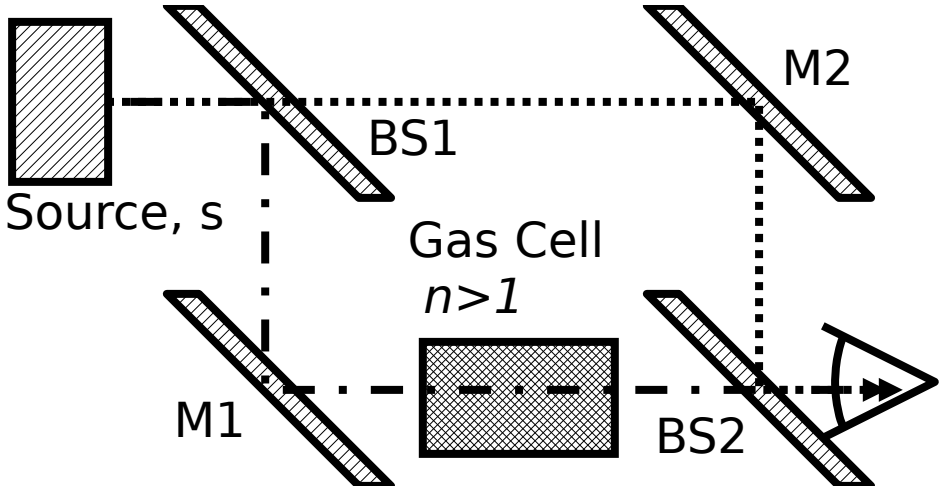

Figure 3.4: The Mach–Zhender Interferometer.

$$I = \frac{P}{A} = \frac{|E|^2}{\eta} = \frac{EE^*}{\eta} \tag{3.25}$$

where η is the impedance of the medium according to

$$\eta = \frac{|\mathbf{E}|}{|\mathbf{H}|} = \frac{1}{n}\sqrt{\frac{\mu_0}{\epsilon_0}} = \sqrt{\frac{\mu_0}{\epsilon}} = \frac{\eta_0}{n} \tag{3.26}$$

where η_0 is the impedance of free space.

Applying Equation 3.25 to the fields summed in Equation 3.24,

$$I = \frac{(E_1^* + E_2^*)\,(E_1 + E_2)}{\eta} \tag{3.27}$$

and expanding Equation 3.27, results in the most useful equation for the irradiance from these two beams in Equation 3.28 [6],

$$I = \frac{E_1^* E_1 + E_2^* E_2 + E_1^* E_2 + E_1 E_2^*}{\eta}. \tag{3.28}$$

The first two terms are frequently referred to as the DC terms and only vary when the incident light field amplitude varies. The latter two terms are called the mixing terms according to

$$I_{mix} = \frac{E_1 E_2^*}{\eta} \; ; \qquad I_{mix}^* = \frac{E_1^* E_2}{\eta} \tag{3.29}$$

and have complex amplitudes dependent on the amplitudes of both fields and their relative optical phases. These expressions relate to the outputs of an RF mixer when the inputs have different frequencies, and are integral to the laser radar.

Looking at the magnitudes of the mixing terms,

$$|I_{mix}| = |I_{mix}^*| = \sqrt{I_1 I_2} \tag{3.30}$$

where I_{mix} is complex and is always added to I_{mix}^* so that their imaginary parts cancel and their real parts add according to

$$I = I_1 + I_2 + 2\sqrt{I_1 I_2}\cos\left(\psi_2 - \psi_1\right) \tag{3.31}$$

where $\psi = \frac{2\pi}{\lambda} n\ell$.

If the change in optical path length due to the material between M1 and BS2 with

$n > 1$ is

$$\Delta OPL = \delta\left(n\ell\right) \tag{3.32}$$

where ℓ is the length of the material, the resultant optical phase change will be, by use of the product rule of differentiation,

$$\delta\psi_1 = k\Delta OPL = 2\pi\frac{\Delta OPL}{\lambda} \approx \frac{2\pi\ell}{\lambda}\delta n + \frac{2\pi n}{\lambda}\delta\ell. \tag{3.33}$$

A second–order term, $\frac{2\pi}{\lambda}\left(\delta n\delta\ell\right)$ that is added to the right–hand side of Equation 3.33, will also be produced when this difference is taken. As the limit approaches zero the second–order term becomes smaller much faster then the two first–order terms and can be neglected. This second–order term will not be included in this research for this reason.

The optical phase changes by 2π for each optical path length change of a wavelength. When $\psi_2 - \psi_1 = 0$, the calculation of optical phase from irradiance becomes problematic because $\frac{d}{d\psi}\cos\psi = 0$. However, when $\psi_2 - \psi_1 = \frac{\pi}{2}$, which is called the quadrature point, $\left|\frac{d}{d\psi}\cos\psi\right| = 1$, and the sensitivity of the measurement is maximized [6]. When $I_1 = I_2 = \frac{I}{2}$, and the beams are from the same source,

$$\frac{\delta I}{\delta\left(n\ell\right)} = \frac{2\pi}{\lambda}I \tag{3.34a}$$

$$\delta\left(n\ell\right) = \frac{\lambda}{2\pi}\frac{\delta I}{I}. \tag{3.34b}$$

Finally, combining Equations 3.34b and 3.33 the interferometer can detect small changes in the index of refraction or length of the material.

$$\delta\left(n\ell\right) = \frac{\lambda}{2\pi}\frac{\delta I}{I} = \ell\delta n + n\delta\ell \tag{3.35}$$

The right–hand side of this equation is fundamental for the calculation of optical phase for the scattering particles. The term $\ell\delta n$ represents the change in OPL due to the index of refraction change within the medium and the term $n\delta\ell$ represents the change in OPL due to the displacement of the medium. The application of Equation 3.35 is discussed in Section 3.3.

The Mach–Zehnder Interferometer [13, 14] is a good starting point for making measurements of the small changes in the index of refraction of a material, and thus, the optical phase. However, limitations do arise because of the cosine term in Equation 3.31. The cosine function is an even function and its inverse will produce two phases with the same irradiance within each cycle. The need to maintain the quadrature point condition, $\psi_2 - \psi_1 = \frac{\pi}{2}$ proves difficult. Additionally, it becomes difficult to determine whether the measured variations in irradiance are the result of variations in the optical phase or in I_1.

These ambiguities can be resolved through alteration of the interferometric technique to one which incorporates both the cosine and sine terms to maximize the sensitivity at $\psi_2 - \psi_1 = \frac{\pi}{2}, \pi, \frac{3\pi}{2}, 2\pi$. Having both the sine and cosine terms is equivalent to having the complex value of I_{mix}. This approach, shown in Figure 3.5, is referred to as optical quadrature detection. It works through implementation of an optical equivalent of an electronic quadrature mixer in order to detect both channels

simultaneously [6]. This method of interferometry has been implemented into microscopy by Warger *et al.* [42] to combine conventional bright field microscopy with an interferometric quadrature detection in order to obtain both amplitude and optical phase information from an image [3]. It has also been proposed for use in laser radar [43] which will be discussed in Section 3.2.2.

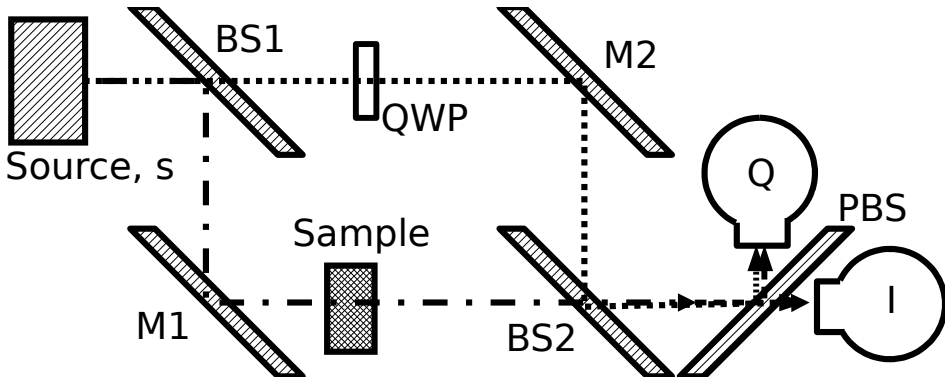

Figure 3.5: Optical Quadrature Detection.

Comparing Figures 3.4 and 3.5, it can be seen that the optical quadrature detection method uses a Mach–Zehnder Interferometer [13, 14] with two additions: a quarter wave plate, QWP, and a polarizing beam splitter, PBS and an additional detector. The incident light is linearly polarized at 45 degrees to the plane of the paper. The quarter wave plate in the reference path, with one axis taken to be in the plane of the paper, converts the reference beam to circular polarization. Generally, it is assumed that the sample does not affect the polarization, however, if suspected, a polarizer could be placed after the sample to correct for this. The purpose of the PBS is to separate the horizontally and vertically polarized components of the beams. The **I** detector collects the horizontal component, the cosine component, and the **Q** detector collects the vertical component, the sine component. The result is a vertical

component that has, in complex notation, been multiplied by a factor of $e^{j\frac{\pi}{2}} = j$ [6].

3.2.2 Doppler Laser Radar

Optical quadrature detection improves upon the techniques employed by the Mach–Zehnder Interferometer [13, 14] to resolve the ambiguities encountered that relate to the cosine term in Equation 3.31 for transmission through a sample. An alternative modification that can be applied to the Mach–Zehnder, for epi-illumination geometries, is to treat the coherent detection system as a laser radar shown Figure 3.6 . This system is designed to observe light that is reflected from an object to measure its distance or velocity, and is referred to as a Doppler Laser Radar.

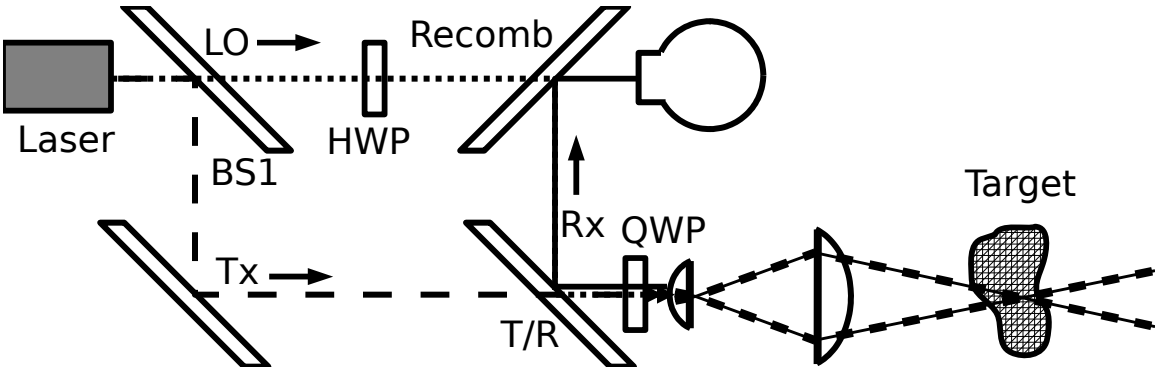

Figure 3.6: Doppler Laser Radar.

In Figure 3.6 some new terminology is used. The reference beam is now referred to as the local oscillator, LO, the transmitter path is designated T_x and the receiver path is R_x. Additional components were added, such as, the half wave plate, HWP, QWP after T/R and before the sample, and lenses following the QWP. BS2 is now called the recombining beamsplitter, Recomb, and the detector is moved here to capture mixed

LO and reflected signal from the target. The T/R beamsplitter, in conjunction with the QWP, allows for a maximum amount of light to be transmitted through the beamsplitter and also reflects as much as possible from the reflection off the target, thus the designation T/R; T=transmitted, R=reflected.

In analyzing laser radar, it is easier to think in terms of power [6],

$$P_{LO} = P_0 R_{BS1} T_{Recomb} \tag{3.36a}$$

$$P_t = P_0 R_{BS1} T_{T/R} \tag{3.36b}$$

$$P_{sig} = P_t F R_{T/R} R_{Recomb} \tag{3.36c}$$

where P_{LO} is the power of the local oscillator, P_t is the power delivered to the target, P_{sig} is the received power at the detector and F is according to

$$F = \frac{\pi D^2}{4z^2} \times \rho_{diff}(\pi) \times e^{-2\mu_{ext} z} \tag{3.37}$$

where $\frac{\pi D^2}{4z^2}$ represents the fraction of energy collected in an aperture of diameter D at a distance z, $\rho_{diff}(\pi)$ is the diffuse reflectance of the target in the backward (π) direction and μ_{ext} is the extinction coefficient. The factor of 2 applied to μ_{ext} accounts for the round–trip through the tissue.

The optical phase of the signal relative to the LO is

$$\psi = \frac{2\pi}{\lambda}(2z - z_0) \tag{3.38}$$

where z is the distance from the laser radar to the target and z_0 is the distance difference within the interferometer. Again, the factor of 2 accounts for the round–trip to the target.

The received signal power from a laser radar may be difficult to detect and can reside within the femtowatt region. One advantage of the coherent detection provided by the Mach–Zehnder, and thus the laser radar, is that by mixing with a reference beam, with power in the milliwatt region, achieves a detectable signal of a nanowatt magnitude. This is the result of multiplication of the signal with the LO as summarized by Table 3.2 [6] where the nomenclature P_1 and P_2 is used to distinguish the power in each arm of the interferometer.

Signal (P_1)	10^{-15}	Watts
Reference (P_2)	10^{-3}	Watts
Detected	10^{-9}	Watts

Table 3.2: Relative Power Level Magnitudes of Laser Radar.

The most common use for the laser radar is to measure the velocity of a moving object. When there is relative motion between two platforms, the frequency of light that is transmitted between them is shifted according to the Doppler frequency, f_d, shown in Equation 1.7, but repeated here for the general case [44],

$$2\pi f_d = \mathbf{k} \cdot \mathbf{v} \tag{3.39}$$

where $\mathbf{k}$ is the original propagation vector of the light and $\mathbf{v}$ is the velocity vector between the source and the detector. The Doppler frequency for laser radar is, in terms of the parallel velocity component, $v_{parallel}$,

$$f_{DR} = 2\frac{v_{parallel}}{\lambda} \tag{3.40}$$

where the factor of 2 accounts for a shift between the source and target as well as the return shift from the target to the source. The deficiency of this Doppler Laser Radar system resides in its inability to distinguish a positive from negative parallel velocity component despite offering precision accuracy in the measurement of the magnitude [6]. It is because of this deficiency that a Quadrature Doppler Laser Radar has been proposed by Hogenboom *et al.* [43] which applies the techniques described by DiMarzio *et al.* [45] for a coherent mixing, or heterodyne, laser radar system that can discern between the positive and negative velocities of the target.

The analysis performed by DiMarzio *et al.* [45] for the signal–to–noise ratio equations for a heterodyne laser radar system applies a back–propagated local oscillator, BPLO, that is a virtual beam from the target that produces the same wavefront as the actual local oscillator at the detector [45]. The development of this methodology begins with the Fresnel–Kirchoff integral for the scalar field, E,

$$E\left(x_1, y_1, z_1\right) = \frac{jk}{4\pi} \iint E\left(x, y, z\right) \frac{e^{jkr}}{r} \left(\hat{n} \cdot \hat{r} - \hat{n} \cdot \hat{r'}\right) \mathrm{d}A \tag{3.41}$$

where the subscripts (x_1, y_1, z_1) represent the unknown field that needs to be calculated, (x, y, z) represent the known field and

$$r = \sqrt{(x - x_1)^2 + (y - y_1)^2 + (z - z_1)^2} \tag{3.42}$$

This is shown in Figure 3.7. The surface, A, is extended to infinity everywhere except at the flat region defined as the plane $z = 0$ so that $E \to 0$. The field, E, arises from a point source at r' located to the left of the surface [6].

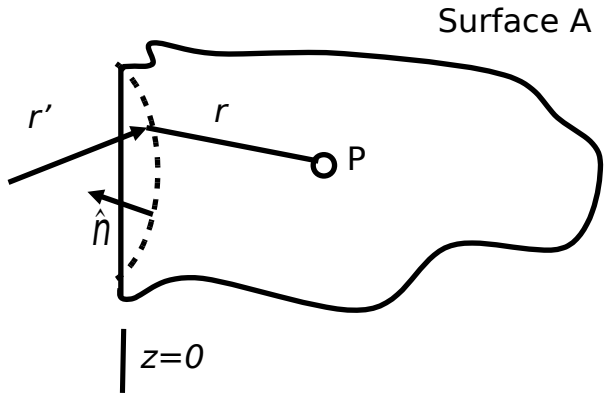

Figure 3.7: Geometry for the Fresnel Integral.

The term $\left(\hat{n} \cdot \hat{r} - \hat{n} \cdot \hat{r'}\right)$ is called the obliquity factor and is a refinement on of Huygen's approach to diffraction that requires the existence of a forward and backward wave. Since $\hat{n} \cdot \hat{r}$ and $\hat{n} \cdot \hat{r'}$ represent the cosines of two angles, for forward propagation along the z direction, this angle can be assumed to be zero simplifying to [6]

$$\left(\hat{n} \cdot \hat{r} - \hat{n} \cdot \hat{r'}\right) = 2. \tag{3.43}$$

Equation 3.41 can be simplified to a general paraxial form where, in the denominator, $r \approx z_1$ because near the axis all the transverse coordinates are small compared to z_1.

This cannot be assumed for the r term in the exponential numerator because small variations in z_1 will result in large changes to the optical phase. Thus,

$$E\left(x_1, y_1, z_1\right) = \frac{jk}{2\pi z_1} \iint E\left(x, y, 0\right) e^{jkr} \, \mathrm{d}A \tag{3.44}$$

$$r = \sqrt{\left(x - x_1\right)^2 + \left(y - y_1\right)^2 + z_1^2}. \tag{3.45}$$

This expression can be further simplified by writing r as

$$r = z_1 \sqrt{\left(\frac{x - x_1}{z_1}\right)^2 + \left(\frac{y - y_1}{z_1}\right)^2 + 1}, \tag{3.46}$$

and through use of Taylor's series, where $(x - x_1) \ll z_1$ and $(y - y_1) \ll z_1$, a first order approximation can be found for the r term in the exponential,

$$r \approx z_1 \left[1 + \frac{\left(x - x_1\right)^2}{2z_1} + \frac{\left(y - y_1\right)^2}{2z_1}\right], \tag{3.47}$$

$$r \approx z_1 + \frac{\left(x - x_1\right)^2}{2z_1} + \frac{\left(y - y_1\right)^2}{2z_1}. \tag{3.48}$$

This results in an easily solvable paraxial form of the Fresnel–Kirchoff integral where the e^{jkz_1} term can be pulled out of the integrand,

$$E\left(x, y, z\right) = \frac{jke^{jkz_1}}{2\pi z_1} \iint E\left(x_1, y_1, 0\right) e^{jk\frac{\left(x - x_1\right)^2}{2z_1} + \frac{\left(y - y_1\right)^2}{2z_1}} \, \mathrm{d}x \, \mathrm{d}y. \tag{3.49}$$

To analyze the BPLO, first, the transmitted beam must be defined through application of Equation 3.49, where $r_1 = \frac{(x-x_1)^2}{2z_1} + \frac{(y-y_1)^2}{2z_1}$ and $C = \frac{jke^{jkz_1}}{2\pi z_1}$,

$$E_t(x,y,z) = C \iint E_t(x_1,y_1,0)\, e^{jkr_1}\, \mathrm{d}x\, \mathrm{d}y. \tag{3.50}$$

This transmitted beam, denoted by the subscript 1 on the spatial and radial terms, will travel to the sample according to Figure 3.6 and be scattered by the particles within the sample. Of this scattered beam, some will be reflected back to the detector. The transmitted beam has finite width and will encompass many particles at once, resulting in a reflected field that is the sum of the individual fields of these particles according to the expression for a signal beam, denoted by the subscript 2 on the spatial and radial terms,

$$E_s(x_2,y_2,z_2) = \sum_p E_t(x,y,z)\, \frac{e^{jkr_2}}{r_2} s_p \tag{3.51}$$

where s_p is a scattering parameter that can be complex and the subscript p represents the scattering particles, each with a unique field, $E_t(x,y,z)$. By the paraxial approximation of Equation 3.48, r_2 can be written as

$$r_2 \approx z_2 + \frac{(x-x_2)^2}{2z_2} + \frac{(y-y_2)^2}{2z_2}. \tag{3.52}$$

The power that falls on the detector from the mixing of the transmitted signal beam and BPLO is

$$P_{mix}\left(x_2, y_2, z_2\right) = \iint \sum_p E_t\left(x, y, z\right) \frac{e^{jkr_2}}{r_2} s_p E^*_{LO}\left(x_2, y_2, 0\right)\, \mathrm{d}x_2\, \mathrm{d}y_2 \tag{3.53}$$

Because the integration is performed over x_2 and y_2 at the detector, Equation 3.53 can be rearranged as

$$P_{mix}\left(x_2, y_2, z_2\right) = \sum_p s_p E_t\left(x, y, z\right) \iint E^*_{LO}\left(x_2, y_2, 0\right) \frac{e^{jkr_2}}{r_2}\, \mathrm{d}x_2\, \mathrm{d}y_2 \tag{3.54}$$

Applying the techniques of DiMarzio *et al.* [45], this expression can be written as

$$P_{mix}\left(x_2, y_2, z_2\right) = C_1 \sum_p s_p E_t\left(x, y, z\right) E^*_{LO}\left(x, y, z\right) \tag{3.55}$$

$$C_1 = \frac{jke^{jkr_2}}{2\pi r_2} \tag{3.56}$$

which holds the form of

$$E_t E^*_{LO} = A_s e^{j2kOPL} = A_s e^{j\frac{4\pi OPL}{\lambda}} \tag{3.57}$$

where A_s is the amplitude of a scattering particle. The expression for the BPLO,

$$E^*_{LO}\left(x, y, z\right) = C_2 \iint E^*_{LO}\left(x_2, y_2, 0\right) e^{jkr_2}\, \mathrm{d}x_2\, \mathrm{d}y_2 \tag{3.58}$$

is identical to the expression for the transmitted field in Equation 3.50 where $C =$

$\frac{jke^{jkz_2}}{2\pi z_2}$. By use of reciprocity, the signal can be determined and the summation performed last.

The signal from any group of scattering particles reflected back to the detector from the sample can be written as

$$S = \sum_p A_p e^{j\frac{4\pi OPL_p}{\lambda}}. \tag{3.59}$$

Optical detection depends on the conversion of power falling on the detector to electrical current over some period of time called the current responsivity [6],

$$\rho_i = \frac{i}{P} = \gamma_{eff}\frac{\mathrm{e}}{\hbar f_o} \tag{3.60}$$

where γ_{eff} is the quantum efficiency, f_o is the optical frequency, $\hbar$ is Planck's constant, $6.626068 \times 10^{-34}\frac{\mathrm{m^2kg}}{\mathrm{s}}$, e is the electron charge, 1.602×10^{-19}C, i is the current and P is the power. Because $f = \frac{c}{\lambda}$, so that $hf \sim e$ and γ_{eff} is the probability that an incident photon will result in a measured electron and is, close to 1 $\frac{\mathrm{A}}{\mathrm{W}}$. For the wavlength commonly used in confocal microscopy, 830 nm, this results in $\rho_i = 0.6629\ \frac{\mathrm{A}}{\mathrm{W}}$. Thus, the current produced at the detector is according to

$$i = \rho_i P = 0.6629\ \frac{\mathrm{A}}{\mathrm{W}} \cdot |S|^2 \approx \left|\sum_p S_p\right|^2 \tag{3.61}$$

where $S_p = A_p e^{j\frac{4\pi OPL_p}{\lambda}}$. By expanding the right–hand side of Equation 3.61, the following can be derived, by defining q as a particle different then particle p and

$S_q = A_q e^{j\frac{4\pi OPL_q}{\lambda}}$,

$$i = \sum_p S_p \sum_q S_q^* = \sum_p |S_p|^2 + \sum_q \sum_{p \neq q} S_p S_q^*. \tag{3.62}$$

If the expectation values are calculated for the second term of Equation 3.62 and their real and imaginary parts are plotted, the expectation value of the sum will tend toward zero. This reduces Equation 3.62 to Equation 3.63 where the expected current will be the result of only the sum of the S_p signals.

$$i_{exp} = 0.6629 \ \frac{\mathrm{A}}{\mathrm{W}} \sum |S_p|^2 \tag{3.63}$$

The following sections apply this technique in the post–processing optical phase analysis. Equation 3.35 defines the total optical phase change for each scattering particle and is broken into two sections for anlysis. Section 3.3.2.2 covers the refractive–index–dependent element of the optical phase, $\ell\delta n$, and Section 3.3.2.1 covers the displacement–dependent element of the optical phase, $n\delta\ell$.

3.3 Development

The MATLAB post processor was designed to take the output files from the Fortran pre–processor, main processor and post–processor as shown in Figure 3.1. There are several scripts that comprise the MATLAB post–processor and they are summarized in Table 3.3. Each will be discussed in detail in the appropriate section to follow.

"ptm.m"	This is the main processor that handles the import of all the files shown in Figure 3.1 and controls the sequencing of the analysis.
"location.m"	This file locates the nodes that each rays traverses based on the exit locations of the rays through the system. From this data, scattering particles are randomly assigned positions within the nodes.
"dispinterp.dat"	This file executes a linear interpolation algorithm on the local displacements calculated by the Fortran post–processor. This interpolation is performed for each scattering particle position.
"phase.m"	The file executes a linear interpolation of the OPL due to the index of refraction change, PPL and directions cosines based upon the exit locations of each ray through the system. This interpolation is performed for each scattering particle position.

Table 3.3: MATLAB Post–processor Files.

The functional stages of the MATLAB post–processor can be broken up into 2 major sections,

1. The Displacement Interpolation. Section 3.3.1 discusses how the integrated displacements are calculated through integration of the linear interpolation of the local displacements of each node volume.

2. The Phase Interpolation. Section 3.3.2 discusses the linear interpolation techniques applied to the OPL due to the index of refraction change, PPL and direction cosines which are then combined with the interpolated displacement values to calculate the optical phase. This is performed in two steps:

   (a) The Refractive Index Dependent Phase, Section 3.3.2.2. This is the optical

phase change from the $\ell\delta n$ term of Equation 3.35.

(b) The Displacement–Dependent Phase, Section 3.3.2.1. This is the optical phase change from the $n\delta\ell$ term of Equation 3.35.

Once each part of Equation 3.35 is obtained, Equation 3.59 can be applied to calculate the optical phase contribution from the change in index of refraction and the optical phase contribution from the change in displacement. These can further be combined to obtain the total optical phase change at the focal point.

The MATLAB post–processor allows for multiple runs at different time steps to be performed. An initial run must commence at time step 1 before any subsequent runs are made. This is hard–coded into "ptm.m" once the user indicates the current run is an initial run. Following this, any time step can be analyzed in any order as long as data files have been generated for each desired time step from the Fortran post–processor. The data files are 'tmpb.dat" and "dlocal.dat". These need to be organized in a separate folder named "Time Step" in the working directory. Within this folder each set of data is stored in a separate folder named "t_X" where "X" is the appropriate time step. The remainder of the files shown in Figure 3.1 are kept in the working directory.

Each subsequent run only reads in the new data for that specific time step contained in the files 'tmpb.dat" and "dlocal.dat". This approach minimizes the execution time for subsequent runs.

3.3.1 Displacement Interpolation

The file "dispint.m" is called from the main processor of the MATLAB post–processor, "ptm.m" to calculate the linear interpolation to the scattering particle's position from the local displacements calculated by the Fortran post–processor. Once this is performed, the data is passed into the file "phase.m" where the integration is performed along each spatial direction to compute the cumulative sum for each respective node from the starting point, $(0, 0, 0)$. The algorithm for this is described in Section 3.1.3 through Equation 3.21.

The local displacement at each node is found at the center location of the node. This differs from the index–dependent OPL, PPL and the direction cosines which are calculated at each ray exit position of each node. Because of this, the displacement interpolation is handled by a separate algorithm, however, the ray exit positions are critical in determining which nodes the rays pass through and subsequently which nodes contain scattering particles.

Each ray's exit position is contained in the file "node_exit.dat" along with its refractive–index–dependent OPL at each exit. An exit is considered as any point the ray exits the node, whether at the back or one of the sides of the node. This causes an unpredictable number of segments to each ray despite the fixed number of nodes along the z direction, $n_z = 9$. To accommodate this uncertainty, within the file is a number printed before each set of data that relates to the number of steps the ray took through the sample which in return, correlates to the number of exit positions. The MATLAB code handles this and organizes the data according to the ray number, the number of exit positions and the time step in a three–dimensional array.

Once the data is read for each ray, each exit position and each time step, the location algorithm determinest for each exit position which node the ray traversed and keeps the data with similar organization. Following this, all the scattering particle positions are created and stored in a separate file, "scatt.dat", so that subsequent runs of the processor can use the same scattering particle locations.

Using the location information along each ray's path, the interpolation algorithm can determine which adjacent node to use for the interpolation. The file "zyx.dat" contains, for each node, all the adjacent nodes stored according to Table 2.3. For each node along the ray's path through the system the algorithm determines the closest node to the scattering particle from the adjacent nodes. This is done by calculating the distance to each adjacent node center from the scattering particle according to

$$r_{dist} = \sqrt{(p_x - x_n)^2 + (p_y - y_n)^2 + (p_z - z_n)^2} \tag{3.64}$$

where a scattering particle's coordinate position is $p(x, y, z)$ and the subscript n represents the node of interest adjacent to the node containing the scattering particle. Each scattering particle is represented by a position vector, $\mathbf{p} = p(x, y, z)$.

There are at most six adjacent nodes to each node of interest; there are less at surfaces, edges and corners. The algorithm determines the minimum r_{dist} value and performs the interpolation for u_n, v_n and w_n according to

$$u(p_x) = u(c_{1_x}) + [u(c_{2_x}) - u(c_{1_x})] \frac{(p_x - c_{1_x}) \cdot (c_{2_x} - c_{1_x})}{|c_{2_x} - c_{1_x}|} \tag{3.65a}$$

$$v(p_y) = v(c_{1_y}) + [v(c_{2_y}) - v(c_{1_y})] \frac{(p_y - c_{1_y}) \cdot (c_{2_y} - c_{1_y})}{|r_{y_{out}} - c_{1_y}|} \tag{3.65b}$$

$$w(p_z) = w(c_{1_z}) + [w(c_{2_z}) - w(c_{1_z})] \frac{(p_z - c_{1_z}) \cdot (c_{2_z} - c_{1_z})}{|r_{z_{out}} - c_{1_z}|} \tag{3.65c}$$

where $\mathbf{c_1} = c_1(x, y, z)$ are the x, y and z values at the center of the node of interest, n_1, and $\mathbf{c_2} = c_2(x, y, z)$ are the x, y and z values at the center of the adjacent node, n_2, closest to the scattering particle. Figure 3.8 shows this.

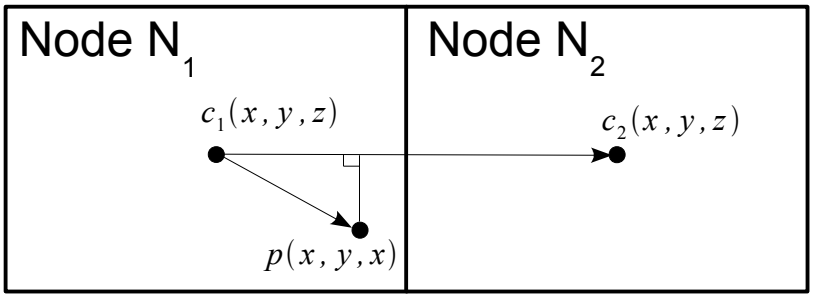

Figure 3.8: Geometry for Equation 3.65, the Displacement Interpolation.

The value $u(c_{1_x})$ represents the displacement in x at point c_1 of Node N_1, the value $u(c_{2_x})$ represents the displacement in x at point c_2 of Node N_2 and the value $u(p_x)$ represents the displacement in x at point scattering particle. The same is true for the v and w terms with respect to y and z. The nomenclature, N, will be used herin to indicate an arbitrary node.

This equation projects point p onto the vector connecting the node centers. This

interpolated displacement value of point p lies between the displacements values at $\mathbf{c_1}$ and $\mathbf{c_2}$ for each coordinate direction.

Once this local interpolation for the displacement at each scattering particle is found, the values are passed into "phase.m" where the integrated displacements are calculated according to Equation 3.21. For the x direction this is the sum of local displacements at the centers of each node along x before the node of interest starting at plane containing the point $(0, 0, 0)$. After the summation is performed, the interpolated displacement value is added to it. This value will be used for the $n\delta\ell$, the displacement–dependent optical phase, calculation discussed in Section 3.3.2.1.

3.3.2 Phase Interpolation

The calculation for the optical phase of each randomly scattering particle is performed through a linear interpolation similar to the one discussed in Section 3.3.1. The interpolation acts on the two parts of the right–hand side of Equation 3.35, $n\delta\ell$ and $\ell\delta n$. These are broken up into the following two sections, Section 3.3.2.1 for $n\delta\ell$ and Section 3.3.2.2 for $\ell\delta n$.

The displacement component, $n\delta\ell$, interpolation was already discussed in the previous section. This section will modify Equation 3.65 to interpolate between the OPL due to the index of refraction change, PPL and the direction cosines at the exit position and each scattering particle. This OPL and the PPL will be used to calculate $\ell\delta n$ and the direction cosines will be used to calculate $n\delta\ell$ along with the displacements.

Once each component of Equation 3.35 is determined, the optical phase at each particle can be calculated according to

$$\psi = \frac{2 \cdot 2\pi}{\lambda} \left[n\delta\ell + \ell\delta n \right]. \tag{3.66}$$

where the first factor of 2 accounts for the return trip. The optical phase amplitude can be found through modification of Equation 3.59, and for the wavelength chosen for the imaging analysis of this research, 830 nm,

$$S = \sum_p A_p e^{j\psi} = \sum_p A_p e^{j\frac{4\pi(n\delta\ell + \ell\delta n)}{\lambda}} \tag{3.67}$$

where the sum is performed over a large number of scattering particles at a particular depth.

3.3.2.1 Displacement–Dependent Optical Phase

The displacement–dependent component to the OPL, $n\delta\ell$ is found by calculating the displacement of the sample at each scattering particle location and the direction each is moving relative to the starting position. This requires an additional piece of information from the Fortran processor; the direction cosines.

The direction cosines are printed to the file "dircos.dat" for the x, y and z directions. These are found at the ray exit positions and need to be interpolated to each scattering particle location. The equation for performing this interpolation is similar to that of Equation 3.65,

$$\hat{\chi}\left(\mathbf{p}\right) = \hat{\chi}\left(\mathbf{r}_{n_1}\right) + \left[\hat{\chi}\left(\mathbf{r}_{n_2}\right) - \hat{\chi}\left(\mathbf{r}_{n_1}\right)\right] \frac{\left(\mathbf{p} - \mathbf{r}_{n_1}\right) \cdot \left(\mathbf{r}_{n_2} - \mathbf{r}_{n_1}\right)}{\left|\mathbf{r}_{n_2} - \mathbf{r}_{n_1}\right|} \tag{3.68}$$

where $\mathbf{r}_{n_1}$ is the position vector at the entrance location of the ray within the node of interest, $\mathbf{r}_{n_2}$ is the exit location of the ray within the same node and $\hat{\chi} = \chi(x, y, z)$. The subscript, n represents the node of interest's entrance, n_1 or exit, n_2. Because the Fortran post–processor produces information at the node exits, it is important to think of the entrance into node N as the exit from node N-1. This is shown in Figure 3.9 and differs from the the displacement interpolation because the values for the direction cosines are known at the entrance and exit as they are calculated along the ray's path through the system.

Direction Cosine term for x, y and z.

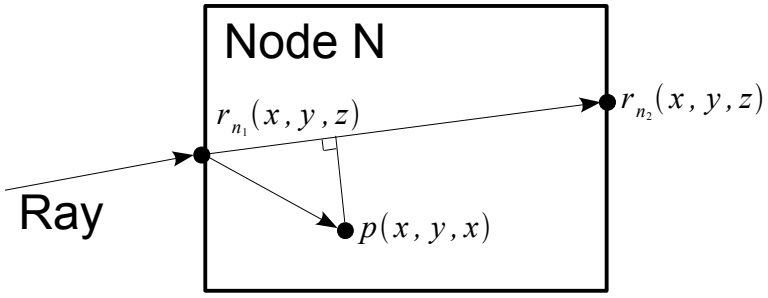

Figure 3.9: Geometry for Equation 3.68, the Direction Cosine, OPL Due to the Change in Index of Refraction and PPL Interpolation.

The incident beam produces 36 rays which are tracked by the raytrace model and are refracted according the the index of refraction changes over time. There is a high probability that multiple rays will travel through the same node, each contributing to the heating of the node which in turn affects the change in index of refraction causing the path length of the ray to change with it's direction through the node. It is assumed that the scattering particles undergo the same displacement changes as the rays and it becomes desirable to pair the scatterers with the nearest ray for the

interpolation.

The MATLAB post processor keeps track of which nodes each ray traverses, but more importantly which rays pass through each node and which entrance and exit positions are associated to each ray. An algorithm was developed locate the closest ray by calculating the distance from each particle to each ray within the same node at the initial time step, then use this information for analysis at subsequent time steps. This ensures that there is no deformation of the system due to the heating and induced stresses resultant from the heating. The governing equation is

$$\mathbf{r}_{dist} = \frac{|(\mathbf{r}_{n_2} - \mathbf{r}_{n_1}) \times (\mathbf{r}_{n_1} - \mathbf{p})|}{|\mathbf{r}_{n_2} - \mathbf{r}_{n_1}|} \tag{3.69}$$

where $\times$ is the cross product of the two vectors.

Once the nearest ray is located for each scattering particle, and the direction cosine for each coordinate direction is calculated, the value for $n\delta\ell$ can be found according to

$$n\delta\ell_{\|} = n\delta\ell \cdot \hat{\chi} = n_0 \left[\Delta x \chi_x + \Delta y \chi_y + \Delta y \chi_y\right] \tag{3.70}$$

where $\cdot$ is the dot product and $n_0 = 1.4$ is the initial index of refraction.

3.3.2.2 Refractive–Index–Dependent Optical Phase

The component of the OPL that is dependent on the index of refraction, $\ell\delta n$, is calculated at each scattering particle in a similar manner to the direction cosines

interpolation. The values that are used for the interpolation are calculated by the Fortran processor and are stored in the file "node_exit.dat".

Section 2.6 indicates that as each ray propagates through a node, the path of the ray is broken into many steps much smaller then the node length in the direction of propagation. For each of these steps, values for the ray's change in OPL due to changes to the refractive index are calculated. When the ray emerges from the node, these values are summed to give a total OPL change for that ray within the respective node. This summation is captured in the file "node_exit.dat", and used for the linear interpolation to the scattering particle.

The equation for this interpolation modifies Equation 3.68,

$$\mathbf{OPL}\left(\mathbf{p}\right) = \mathbf{OPL}\left(\mathbf{r}_{n_1}\right) + \left[\mathbf{OPL}\left(\mathbf{r}_{n_2}\right) - \mathbf{OPL}\left(\mathbf{r}_{n_1}\right)\right] \frac{\left(\mathbf{p} - \mathbf{r}_{n_1}\right) \cdot \left(\mathbf{r}_{n_2} - \mathbf{r}_{n_1}\right)}{\left|\mathbf{r}_{n_2} - \mathbf{r}_{n_1}\right|} \tag{3.71}$$

where **OPL** is a function of x, y and z and the geometry is according to Figure 3.9. The interpolated change in refractive–index–dependent OPL at each scattering location demands the definitions of $\mathbf{r}_{n_1}$ and $\mathbf{r}_{n_2}$ be the same as for the direction cosines. Once each scattering particle is associated to the nearest ray all calculations are taken from that respective ray for all any subsequent runs at different time steps.

Applying the same methodology, the PPL, stored in "dircos.dat", is calculated according to

$$\mathbf{PPL}\left(\mathbf{p}\right) = \mathbf{PPL}\left(\mathbf{r}_{n_1}\right) + \left[\mathbf{PPL}\left(\mathbf{r}_{n_2}\right) - \mathbf{PPL}\left(\mathbf{r}_{n_1}\right)\right] \frac{\left(\mathbf{p} - \mathbf{r}_{n_1}\right) \cdot \left(\mathbf{r}_{n_2} - \mathbf{r}_{n_1}\right)}{\left|\mathbf{r}_{n_2} - \mathbf{r}_{n_1}\right|} \tag{3.72}$$

The PPL, or physical path length, represents the length of the ray as if it were traveling through free space. Assuming the system is undeformed, not affected by the heating, the physical length from the ray's entrance to its exit summed over the small spatial steps through each node would represent the PPL.

The Fortran processor assumes no deformation to the sample, but tracks each ray's entrance angle as if there were deformation from the heating and induced stresses. This is represented by the direction cosines. The angle at which the ray enters will change over time as the index of refraction changes and will start to change at later time steps throughout the sample. The non–uniform heating present causes a greater change in the index of refraction near the focus then at either of the axial extrema. This can be seen in Figures 3.10 and 3.11. Figure 3.10 shows the path for ray 1 at the initial time step, $t = 25$ ns, and the final time step, $t = 5$ μs at the focus, $z = 26$ μm. Over this time period, there is a temperature change of approximately 18 °C that drives this process. Figure 3.11 shows the same, but at $z = L_z = 60$ μm. The temperature change here is less which results in less of a change in the directions cosines.

The change in OPL calculated at each node exit determines how much this physical path length changes within each node. After each value is interpolated to the scattering particle, the total OPL of each ray within each node is,

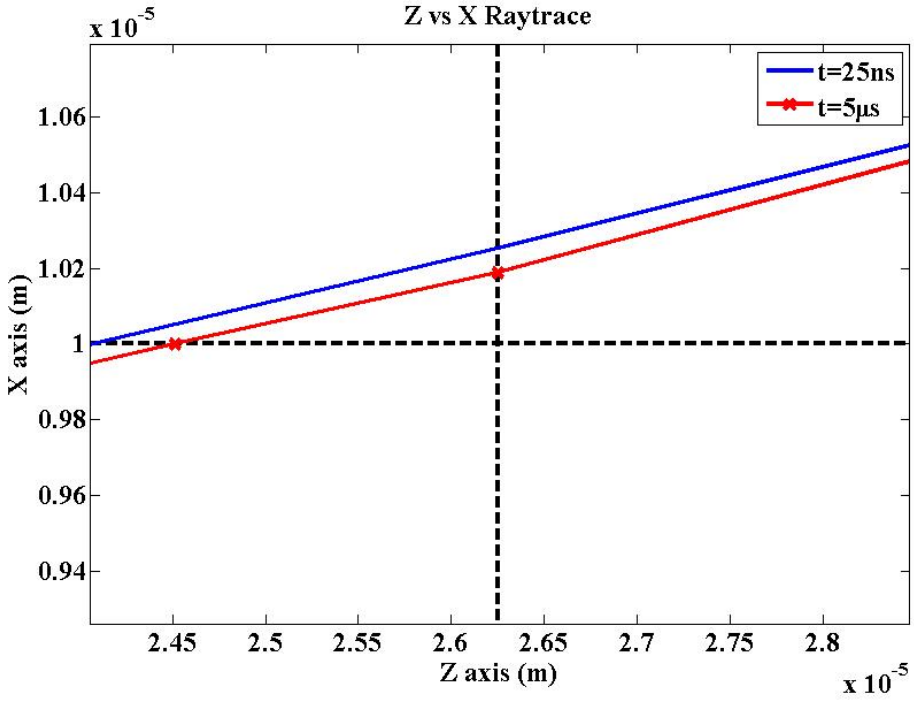

Figure 3.10: Ray 1 Path Through the System at $t = 25$ ns, and $t = 5$ μs at the Focus.

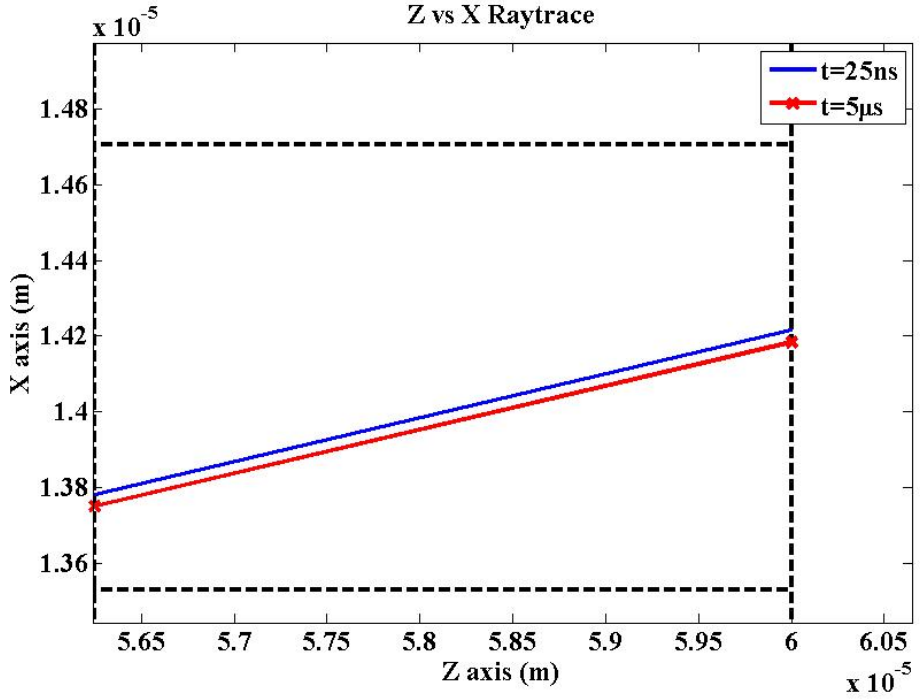

Figure 3.11: Ray 1 Path Through the System at $t = 25$ ns, and $t = 5$ μs for $z = L_z = 60$ μm

$$OPL = \Delta OPL + PPL. \tag{3.73}$$

Once the total OPL for the index–dependent component is obtained it can be combined with the displacement–dependent component, Equation 3.70 according to Equation 3.67 to get the optical phase amplitudes of the scattering particles.

The MATLAB post–processor distributes the scattering particles according to beam concentration within the sample. This simulates the expected response of the physical system; there are a greater number of scattering particles contributing to the optical phase amplitude near the focus. To model changing irradiance, scattering particles become more sparse as the axial distance increases away from the focus. Consequently,

the spatial distance between scattering particles also increases.

The results of this optical phase analysis will be discussed in Chapter 4. The summation of scattering particles over each slice of z, a slice consisting of the $x-y$ nodal grid at each nodal position along z, 9 in total, will be taken. The two components of the OPL will be analyzed separately to determine the effect each has on the optical phase measurement.

Chapter 4

Results

The techniques developed for this research employ a rigorous optical, thermal and mechanical computational analysis to demonstrate the use of Photothermal Microscopy to acquire information about the optical phase of scattering particles thus improving the contrast and depth of imaging limited by out–of–plane scatter. Several observations were made to validate the effectiveness of the photothermal microscope as a useful tool for biological imaging of human skin:

1. The results compare well with theoretical and analytical expectations.
2. The Photothermal Microscope operates within safe limits for *in vivo* imaging.
3. The optical path length is enough to be measured within the heating pulse duration defined.
4. The change in the index of refraction due to the photothermal process is significant.

5. The displacement of the scattering particles is localized.

6. The change in the index of refraction is not localized and requires a differential optical phase measurement.

The comparison of the computational results to that of the theoretical assumptions is discussed in Section 4.1. The safety analysis performed for the defined operational parameters of the photothermal microscope is compared to the American National Standards Institute's (ANSI) Standard for the Safe use of Lasers, Z–136.1 [46] in Section 4.2. Section 4.3 discusses the optical phase analysis of the two components of the optical path length, $n\delta\ell$ and $\ell\delta n$. Finally, Section 4.4 discusses the localization of the $n\delta\ell$ component of the optical phase measurement and the non–localization of the $\ell\delta n$ component of the optical phase measurement. This observation requires that a differential measurement be taken into account for large optical phase change in the refractive–index–dependent optical phase term.

4.1 Comparison to Theoretical Assumptions.

The expectation of the temperature rise within a node volume under the Fourier Conduction Law is according to Figure 4.1. This figure is for a general case using the Lumped Capacitance Parameter analytical solution to Equation 2.1 for the differential energy balance in a material. The material is a cube of 1 mm and satifies the lumped capacitances assumptions. The parameters used to generate this figure are listed in Table 4.1 under the "Theoretical" column. For comparison, the parameters used in the computational analysis, found in Table 2.1 from "pre_txt" are listed under the column labeled "Computational".

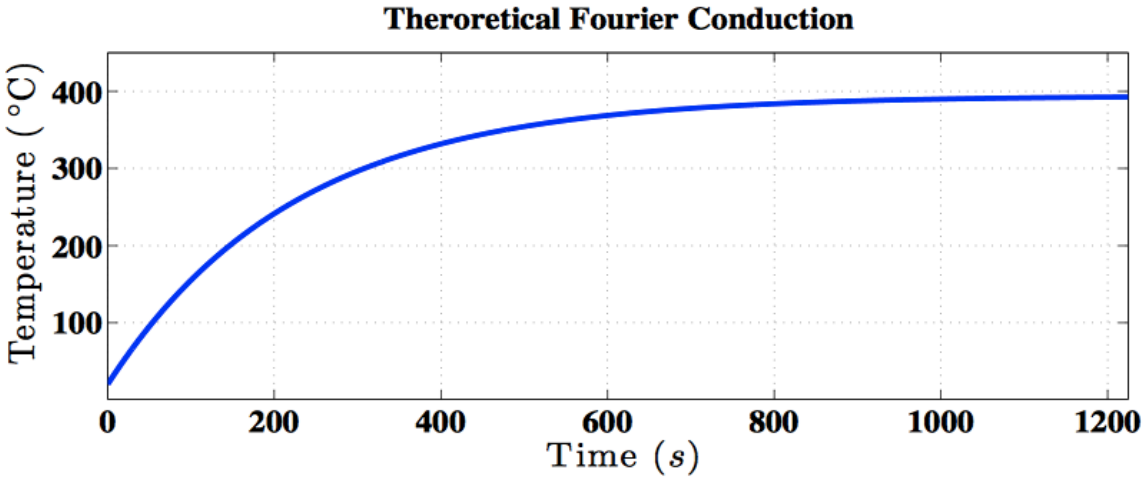

Figure 4.1: Theoretical Temperature Profile for the Fourier Conduction Law.

Theoretical	Computational	Parameter
5000 $\frac{\mathrm{W}}{\mathrm{m}^2}$	4908.73 $\frac{\mathrm{W}}{\mathrm{m}^2}$	Surface Heat Flux.
2500 $\frac{\mathrm{kg}}{\mathrm{m}^3}$	992.2 $\frac{\mathrm{kg}}{\mathrm{m}^3}$	Density.
1250 $\frac{\mathrm{kJ}}{\mathrm{kg}\cdot\mathrm{K}}$	4181.3 $\frac{\mathrm{kJ}}{\mathrm{kg}\cdot\mathrm{K}}$	Specific Heat.
1.4 $\frac{\mathrm{W}}{\mathrm{m}^2\cdot\mathrm{K}}$	.58 $\frac{\mathrm{W}}{\mathrm{m}^2\cdot\mathrm{K}}$	Thermal Conductivity.
7.0 $\frac{W}{\mathrm{m}^2\mathrm{K}}$	7.0 $\frac{W}{\mathrm{m}^2\mathrm{K}}$	Heat Transfer Coefficient.
1.0mm	20 μm×20 μm×60 μm	Length of Cube.
37 °C	37 °C	Ambient Temperature.
1225 s	5 μs	Pulse Duration.

Table 4.1: Parameters for the Theoretical Fourier Conduction Law Comparison.

It can be seen from Figure 4.1 that an initial steep temperature gradient is present, and then, after a long time period, the temperature rise is saturated and the temperature reaches a steady state asymptote. This saturation region is undesirable for this research because at this time the displacement and index of refraction within the material no longer change, or are negligible.

Thermal confinement is discussed in Section 1.1 according to Equation 1.4. By defining an *Axial Optical Zone* to be 2 times the Rayleigh length, z_R, and a *Transverse Optical Zone* to be $2\omega_0$, the beam diameter at the focus, the pulse duration must be less then 10 ms to prevent axial confinement and 300 μs to prevent confinement in the transverse directions. In this research diffusion is present, but only within the *Optical Zone* defined above, and can be see in Figure 2.10.

The other consideration is to ensure that the pulse duration isn't too short allowing for stress confinement, which is desirable for PTA, but not for this research. Stress confinement is also discussed in Section 1.1 and according to Equation 1.5 requires that the pulse duration is greater then 44 ns for to prevent confinement axially and 7 ns to prevent confinement in the transverse directions. The 5 μs pulse duration used for this research is greater then the limits for stress confinement, thus the material is not constrained by this condition.

The temperature gradient for four selected node volumes over the entire pulse duration is shown in Figure 4.2A. The chosen node volumes are node 478 located on the second z–slice layer in the center of the $x-y$ plane, node 1774 located at the focus, node 1756 located adjacent in the $+y$–direction to node 1774 and node 2746 located on the last, ninth, z–slice on the back face of the sample, also centered on the $x-y$ plane. Nodes 478, 1774 and 2746 were chosen to show the direct absorption effects before, at

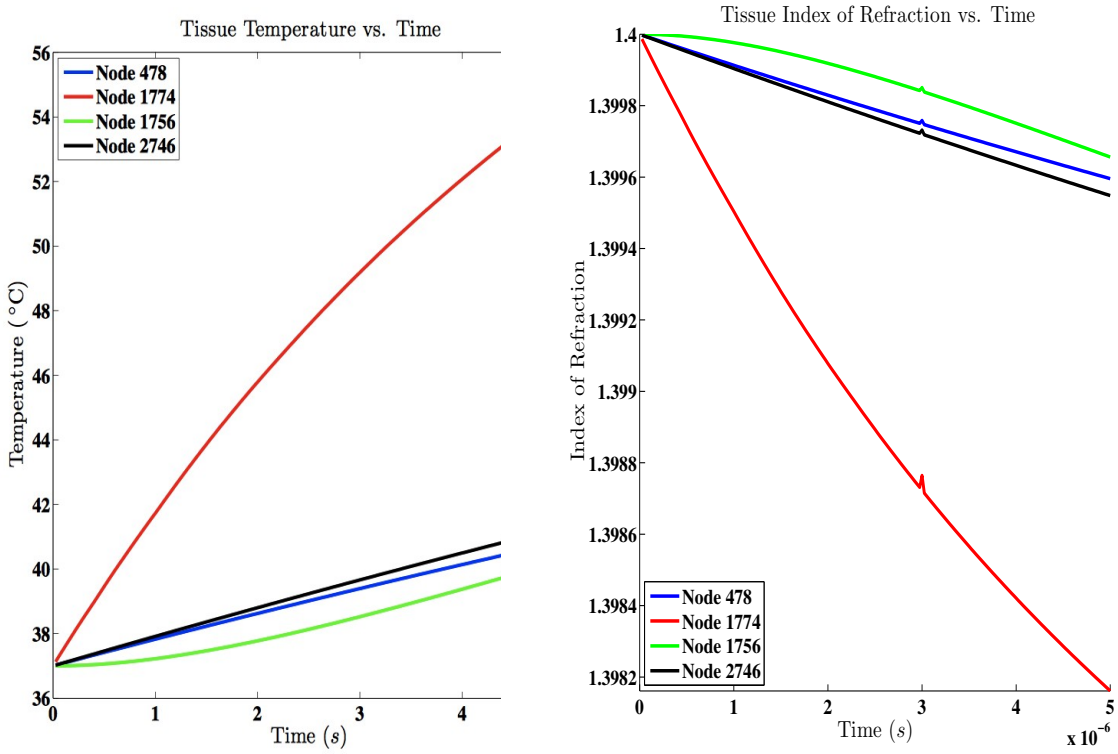

Figure 4.2: (A) Computational Temperature Gradient Over Time for Tissue. (B) Computational Index of Refraction Over Time for Tissue.

and after the focus. Node 1756 was chosen because it is out of the beam path and its absorption is due to diffusion over time. The results agree with the theoretical model of Figure 4.1 and with expected results for the temperature gradient due to the heat diffusion.

The same nodes used for the temperature gradient comparison were also used to evaluate the change in the refractive index of the model. This can be seen in Figure 4.2B. The relationship seen between the temperature gradient and the change in the index of refraction shows a good agreement with theoretical expectations.

4.2 Operational Parameters.

The computational model was performed with the parameters shown in Table 2.1. The Fortran pre–processor requires an irradiance at the objective lens of the system. This value, seen in Line 23, column 1, is 4908.73 $\frac{\mathrm{W}}{\mathrm{m}^2}$. The radius at the surface of the sample, $\sim$ 30 μm from the focus, by Equation 2.19, is 5.11 μm. This gives an irradiated area at the surface of the sample of 8.203×10^{-11} m^2 or 8.203×10^{-7}cm^2.

The ANSI standard for lasers, Z–136.1 [46] requires for pulse durations between 10 ns and 10 s for wavelength's between 1500 nm and 1800 nm a maximum of 1.0 $\frac{\mathrm{J}}{\mathrm{cm}^2}$ at the surface of the skin. For this research, an irradiance of 4908.73 $\frac{\mathrm{W}}{\mathrm{m}^2}$ at the lens with diameter, 2.543×10^{-5} m gives a power of 50 mW. With a pulse duration of 5 μs this produces a 2.5×10^{-7} J of energy at the surface. The resultant energy per irradiated area is 0.357 $\frac{\mathrm{J}}{\mathrm{cm}^2}$, which is well within the limit imposed by the ANSI standard.

The research conducted by Rajadhyaksha *et al.* [10] employs a confocal microscope for *in vivo* imaging. This microscope has received FDA approval and is in limited use in medical research hospitals. The power output is approximately 30 mW and the laser is continuous wave with a dwell–time on each pixel around 300 ns at a wavelength of 830 nm. By the ANSI standard, for comparison, the safe limit for a this laser is 0.0468 $\frac{\mathrm{J}}{\mathrm{cm}^2}$, and the actual energy per area is 0.0321 $\frac{\mathrm{J}}{\mathrm{cm}^2}$. This comparison shows a great potential for the Photothermal Microscope.

4.3 Optical Path Length Measurement.

The optical path length is measured as two separate components, the displacement–dependent component, $n\delta\ell$, and the refractive–index–dependent component, $\ell\delta n$. The formulation of these is discussed in Section 3.2.2, and the computational analysis is discussed in Section 3.3. The results are presented for the wavelength common to the confocal microscope, 830 nm. Examination of Equation 3.67 shows that the value of the term in the exponent is inversly proportional to the wavelength of the imaging laser. By decreasing this wavelength, the strength of this complex amplitude will increase. However, at lower wavelengths, skin becomes more diffusive and intruduces potential degradation to the signal.

As the sample heats, it expands. The non-uniform nature of the system due to the energy of the laser being focused near the center of the sample axially as well as in the transverse plane causes the index of refraction to change according to Figure 4.2B. As the sample undergoes thermoelastic expansion, the location of the scattering particles will change causing a displacement. The combination of these two parameters accounts for the total change to the optical path length. This research handles both parameters separately for each scattering particle through similar interpolative analyses.

The sample is divided into 9 nodes along the z–axis which corresponds to 9 $x-y$ planes, or 9 slices along the z–axis. The particles are distributed differently according to location along the axis to model the changing irradiance from the source beam. Each parameter of the OPL is input into the right–hand side of Equation 3.57 to

calculate the optical phase of each scattering particle. Once this calculation is performed, the optical complex amplitudes obtained are summed according to z–slice by Equation 3.67 and the resultant values are stored in separate arrays for each component of the OPL.

The expectation when plotting each component, $n\delta\ell$ and $\ell\delta n$, in the real versus imaginary plane is that over time, the optical phase values will inscribe a circle about the origin. However, if the OPL change is greater then one wavelength between any two consecutive time steps, this method of visualization and analysis will not be valid. Essentially, the sum of the optical phase amplitudes for a particular z–slice will have seemingly random positions on the real versus imaginary plane at each time step and no information about the optical phase can be determined. Figure 4.3 shows the real versus imaginary component of the optical phase amplitude for the displacement–dependent optical phase component.

Each slice along the axial direction is plotted in this figure. The cyan curve represents the focus which can be seen to offer the greatest signal amplitude. At slices away from the focus the simulated received signal amplitude has degraded proportionate to the distance from the focus; the microscope is most sensitive to measurements at the focus.

The similar plot for the refractive–index–dependent component of the optical phase was omitted from this paper since, within a respective time step, the change in this parameter for a particular scattering particle could be several wavelengths. Instead, the techniques discussed in Section 4.4 to unwrap the optical phase information will be presented.

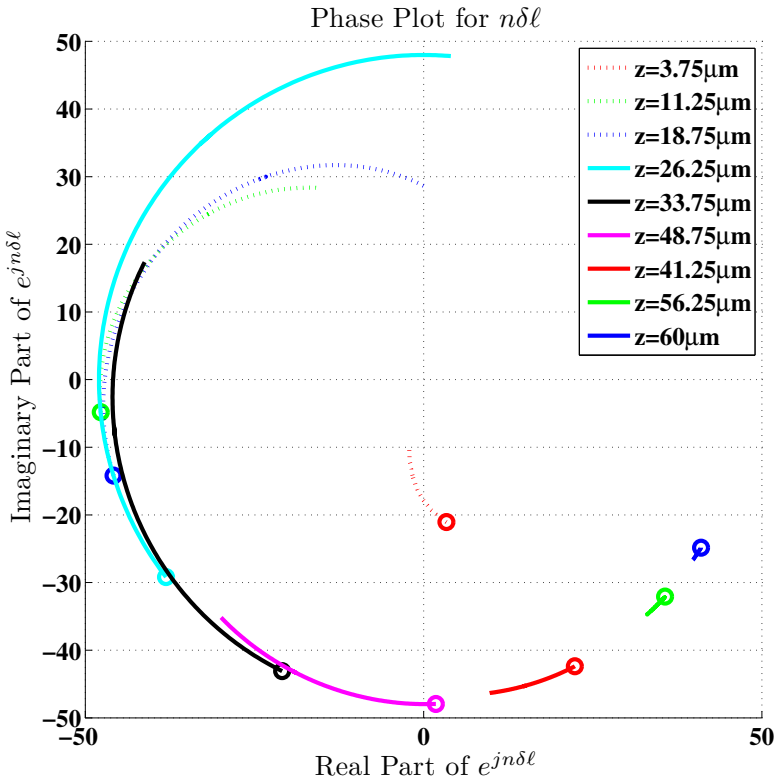

Figure 4.3: Real vs. Imaginary Plot for the $n\delta\ell$ Component of the Optical Phase.

4.4 Localization Discussion.

To handle the problem with the refractive–index–dependent OPL change of multiple wavelengths, a technique which unwraps the phase information must be employed. This technique is a plot of radians versus time. Figure 4.4 shows the plot for the displacement–dependent component, $n\delta\ell$ for comparative purposes. It can be seen that at the focus, cyan curve, the greatest change is occurring and over all time the the sum of optical phase amplitudes from the displacement–dependent component of

the scattering particles only changes by a fraction of the wavelength.

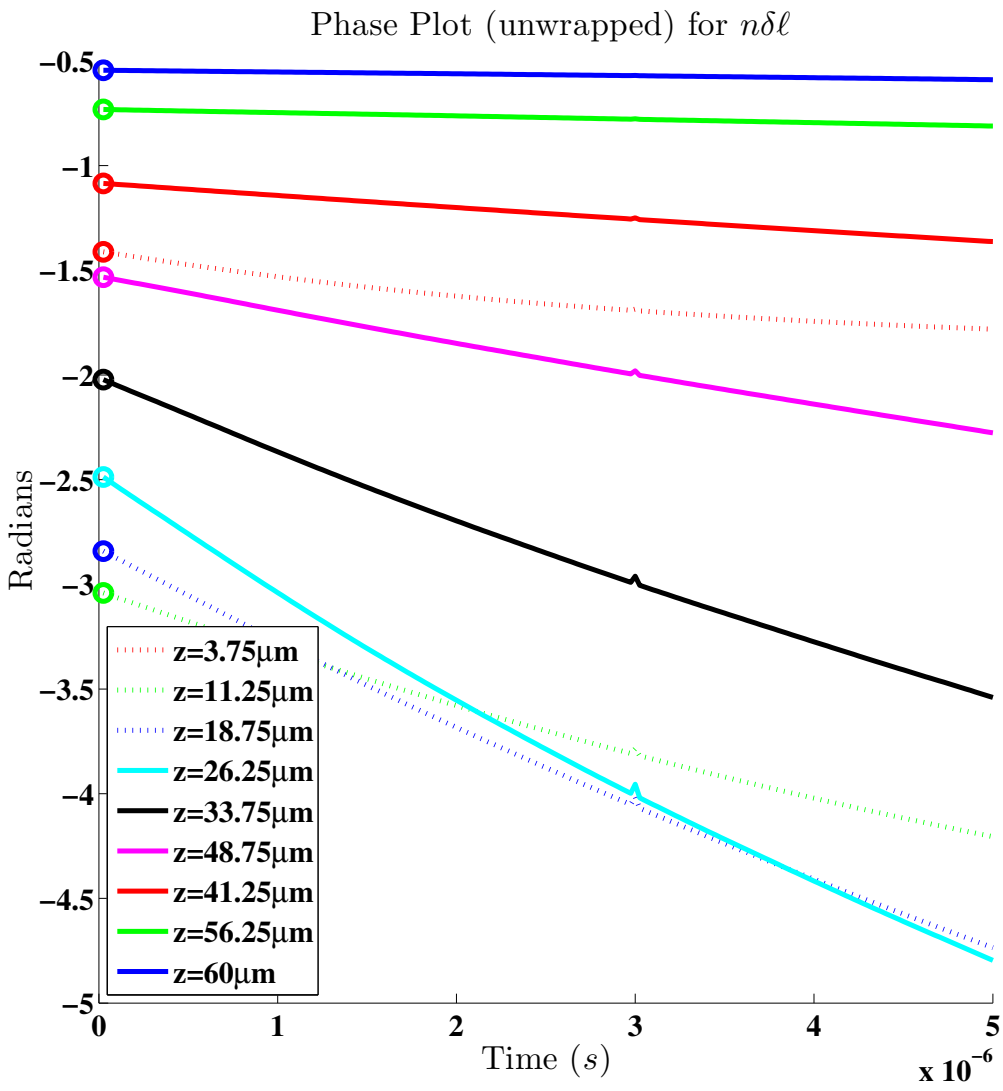

Figure 4.4: Plot of the Unwrapped $n\delta\ell$ Component of the Optical Phase.

The refractive–index–dependent component of the optical phase is plotted in Figure 4.5. Here, it is observed that greatest change to the OPL is from the particles past the focus near the back side of the system. In fact, the cyan curve shows little change in comparison and the slices before the focus, at the entrance to the system,

have almost no change to their OPL from the index of refraction change.

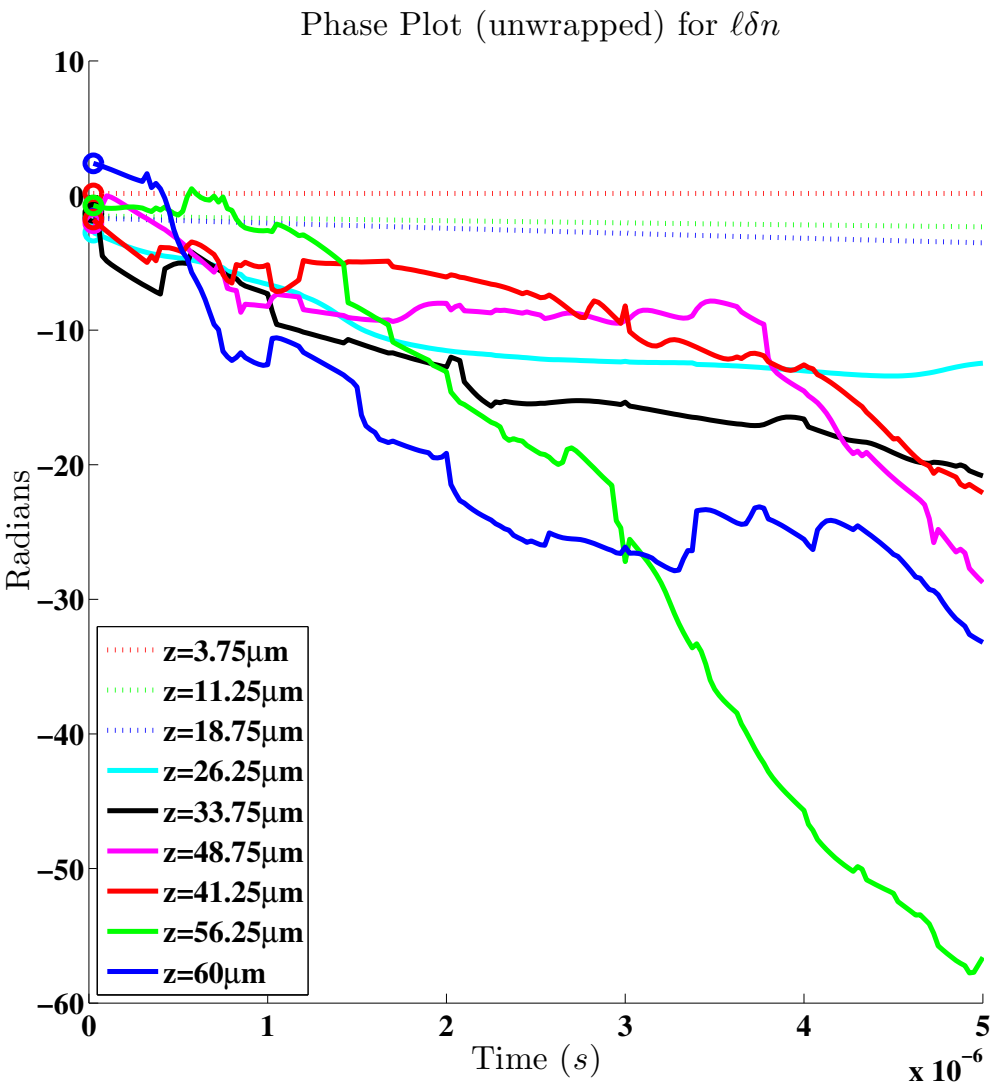

Figure 4.5: Plot of the Unwrapped $\ell\delta n$ Component of the Optical Phase.

These results show that the displacement–dependent component of the optical phase is localized; changes to the displacement are greatest near the focus and will provide the strongest measurement. Conversely, the magnitude of the displacement becomes lower away from the focus. The refractive–index–dependent component of the optical

phase, in contrast, is not localized. The index of refraction is an integration over the path of the ray dependent on contributions from each node volume the ray traverses. Consequently, this contributes an increasingly greater amount as the ray traverses the system and over time, this value continues to increase and changes to the OPL of several wavelengths occur.

To account for the lack of localization of the refractive–index–dependent component of the optical phase, a differential optical phase measurement is needed. Comparing the optical phase values at adjacent slices will provide information as to magnitude of contribution from the smaller but more local $n\delta\ell$ term.

Chapter 5

Conclusions and Future Research

Imaging of biological tissue requires good contrast and resolution of the image to be maintained at suitable penetration depths. The out–of–plane scatter by particles located outside the focal plane inhibits this contrast and resolution in turbid media, such as human skin. The temporal change in the coherent sum of scattered field amplitudes makes it possible to reject the clutter produced in measurements at deep penetration depths by the light backscattered from particles outside the focal plane. This will enhance the capabilities of the confocal microscope to image deeper while maintaining its high resolution.

This research demonstrates through, accurate computational modeling, the potential for a Photothermal Microscope to measure the displacement of scattering particles from the thermoelastic expansion of the tissue. The model provides rigorous quantitative estimates of displacement, and also demonstrates the importance of accounting for heat–induced changes in the refractive index. These heat induced changes cause a loss of localization of the refractive–index–dependent component of the optical phase

and will require a differential measurement of the optical phase to be made.

Imaging tissue *in vivo* by use of lasers poses potential safety risks. The Photothermal Microscope has been shown to operate within the specification imposed upon lasers for skin exposure. Thus, further work needs to be performed to develop the Photothermal Microscope and produce *in vitro*, and eventually *in vivo* imaging of tissue.

The next steps toward the development of the Photothermal Microscope would include modeling of different samples, modeling with different numerical aperture values for the objective lens and modeling at different imaging wavelengths. An increase in the numerical aperture will result in better axial and transverse resolution. A decrease in the wavelength of the imaging laser would produce greater complex amplitude in the signal, but a potentially weaker absorption in the skin. This numerical modeling would provide an optimized design for the Photothermal Microscope thus allowing for construction of an operational instrument.

Once the operational Photothermal Microscope has been constructed testing could begin on skin phantoms, and then excised skin. The results of the experiment could then be compared to the computational results of the modeling as well as compared with the confocal microscope. This will allow for testing on healthy skin *in vivo* and eventually skin containing cancerous tumors.

The numerical analysis presented in this research provides a method for characterizing skin by making use of the mechanical and thermal properties. This characterization of skin is instrumental to advancing the theoretical concept of non–invasive *in vivo* imaging of human skin through Photothermal Microscopy.

Appendix A

Pre-processor File Definitions

This section describes, line–by–line, the inputs into "pre_txt". The values chosen for this research are displayed with each appropriate line and column. The format used in "pre_txt" with appropriate nomenclature is shown followed by the values input into "pre_txt" for this research. Each parameter is explained in a table following the appropriate line. The nomenclature is according to the variables used in the Fortran pre–processor script.

'Line 1:',nfmodel,model,izflg,ifdex,iramp,ibflg,ibmg

'Line 1:',0,1,1,0,0,0,0,0

nfmodel	Fourier or Non-Fourier model: 1 = Fourier; 0 = Non-Fourier.
model	Thermal Transport Model: 0 = Thermal Analysis Only; 1 = One Step Model; 2 = Two Step Model.
izflg	Nonlinear Optical Problem: 1 = Nonlinear Optical Problem.
ifdex	Type of Nonlinear Optical Mechanism: 0 = Optical Mechanism, $n(T, I)$ and $\alpha(I)$; 1 = Temperature-Dependent Optical Mechanism; 2 = Steady State Saturable Absorber Optical Mechanism.
iramp	Temporal Form of Heat Input: 0 = Square Wave; 1 = Trapezoid Pulse; 2 = Nucear Explosion Pulse; 3 = Gaussian Pulse.
ibflg	Transient or Steady State Optical Properties: 0 = Steady State; 1 = Transient.
ibmg	Input Beam Type: 0 = Spatial Gaussian; 1 = Top Hat Profile; 2 = Plane Wave.

'Line 2:',convg

'Line 2:',0.01

convg	Convergence Criterion for the Euler Predictor–Corrector.

'Line 3:',jctn

'Line 3:',1

jctn	Number of Constant Temperature, Ambient, Nodes.

'Line 4:',nb

'Line 4:',1

nb	Number Material Blocks.

'Line 5:',dzmin,nymin,dxmin

'Line 5:',6.4e-06,1.1e-6,1.1e-6

dzmin	Suggest the Node Spacing in the z direction.
dymin	Suggest the Node Spacing in the y direction.
dxmin	Suggest the Node Spacing in the x direction.

'Line 5a:',dzmin,nymin,dxmin

'Line 5a:',0.0.,0.0.,0.0

dzmin	Input Velocity in the z direction.
dymin	Input Velocity in the y direction.
dxmin	Input Velocity in the x direction.

Repeat Lines 6–11 for Each Material Block Indicated in Line 4

'Line 6:',dns,sc,rk,qvl,ar,abr

'Line 6:',992.2,4181.3,0.58,0.0,1759,0.0

dns	Density.
sc	Specific Heat.
rk	Thermal Conductivity.
qvl	Internal heat Generation
ar	Linear Absorption Coefficient.
abr	Nonlinear Absorption Coefficient.

'Line 7:',dimz(i,1),dimy(i,1),dimx(i,1),dimz(i,2),dimy(i,2),dimx(i,2)

'Line 7:',60e-6,20e-6,20e-6,0.0,0.0,0.0

dimz(i,1), dimy(i,1), dimx(i,1)	Maximum z, y and x Block Corners for the ith Material Block.
dimz(i,2), dimy(i,2), dimx(i,2)	Maximum z, y and x Block Corners for the ith Material Block.

'Line 8:',vo,bi0,prot,akpa,alnep,yungs

'Line 8:',1.00786e-3,207e-6,0.495,4.54e-10,1e-4,34307

vo	Specific Volume.
bi0	Volumetric Coefficient of Expansion.
prot	Poisson's Ratio..
akpa	Isothermal Compressibility.
alnep	Linear Coefficient of Expansion.
yungs	Young's Modulus.

'Line 9:',dndt

'Line 9:',0.0

dndt	Rate of Change of Index of Refraction. This is zero if bi0 is used.

'Line 10:',rio,znr

'Line 10:',1.4,3.4e-37

rio	Linear Indx of Refraction.
znr	Nonlinear Index of Refraction.

'Line 11:',cco

'Line 11:',660

cco	Speed of Sound in Material.

'Line 12:',prd,ncyl

'Line 12:',5.001e-6,1

prd	Pulse Duration.
ncyl	Number of Pulse Cycles.

'Line 13:',ftim,cktim0

'Line 13:',5.001e-6,2.5e-8

ftim	Final Simulation Time.
cktim0	Time Step Increment.

'Line 14:',igpt,ispt

'Line 14:',1.0,1.0

igpt	Generation–Time-Dependent Parameter.
ispt	Surface–Time–Dependent Parameter.

'Line 15:',ramp,plat,tffst

'Line 15:',0.0,0.0,0.0

ramp	Time of Ramp for Gaussian Pulse.
plat	Plateau Time for Gaussian Pulse.
tffst	Offset Time for Gaussian Pulse.

'Line 16:',dtime

'Line 16:',1e-9s

dtime	Initial Time Step of Simulation.

'Line 17:',cut

'Line 17:',0.10

cut	Cutoff Value for the Ray Reflection.

'Line 18:',ireflon

'Line 18:',0

ireflon	Type of Reflections for Simulation: 0 = No Reflections; 1 = Surface Reflections Only; 2 = Internal Reflections Only; 3 = All Reflections On; 4 = Incident Surface Reflections Only.

'Line 19:',n0,q0,q00

'Line 19:',1,0.0,4908.73

n0	Normalization Type: 1 = Normalize With Ray Flux; 2 = Normalize With Surface Flux.
q0	Characteristic for Ray Flux.
q00	Characteristic for Surface Flux.

'Line 20:',na

'Line 20:',1

na	Number of Irradiated Areas.

'Line 21:',riz1,riy1,rix1,riz2,riy2,rix2

'Line 21:',0.0,14.11e-6,14.11e-6,0.0,5.88e-6,5.88e-6

riz1, riy1, rix1	Maximum z, y and x Corners of the Irradiated Area.
riz2, riy2, rix2	Minimum z, y and x Corners of the Irradiated Area.

'Line 22:',zlsl,cz,cy,cx

'Line 22:',15.97e-03,0.0,10e-6,10e-6

zlsl	Distance From the Sample to the Input Lens.
cz, cy, cx	Center z, y and x Locations of the Irradiated Area.

'Line 23:',rl,fl

'Line 23:',2.545e-3,15.99142e-3

rl	Beam Radius at the Input Lens.
fl	Focal Length of the Input Lens, Corrected for the Refraction in the Sample.

'Line 24:',zig,waist,zlambda

'Line 24:',4908.73,2.14286e-6,1.5e-6

zig	Irradiance of the Source Beam at the Input Lens.
waist	Spot Size at the Focus of the Source Beam.
zlambda	Wavelength of the Source Beam.

'Line 25:',az,ay,ax

'Line 25:',1.0,0.0,0.0

az, ay, ax	Direction Cosines for the Incident Irradiance on the Sample in the z, y and x Directions.

'Line 26:',ppar,pperp

'Line 26:',0.5,0.5

ppar	Parallel Polarization Component of the Incident Field.
pperp	Perpendicular Polarization Component of the Incident Field.

'Line 27:',dss

'Line 27:',2.5e-04

dss	Refraction Step.

'Line 28:',b(1),b(2),b(3)

'Line 28:',7.0,7.0,0.0

b(1), b(2), b(3)	Convective Heat Transfer Coefficients for the $+z, -z$ and $+y$ directions.

'Line 29:',b(4),b(5),b(6)

'Line 29:',0.0,0.0,0.0

b(4), b(5), b(6)	Convective Heat Transfer Coefficients for the $-y, +x$ and $-x$ directions.

'Line 30:',q(1),q(2),q(3)

'Line 30:',0.0,0.0,0.0

q(1), q(2), q(3)	Surface Heat Flux Values for the $+z, -z$ and $+y$ directions.

'Line 31:',q(4),q(5),q(6)

'Line 31:',0.0,0.0,0.0

q(4), q(5), q(6)	Surface Heat Flux Values for the $-y, +x$ and $-x$ directions.

'Line 32:',ict(i)

'Line 32:',1

icti	Node numbers of constant temperature.

'Line 33:',pult

'Line 33:',1.0

pult	Fraction of Period: 1 = On, 0 = Off.

'Line 34:',tiamb,riamb

'Line 34:',37.0,1.0

tiamb	Value of the Ambient Temperature.
riamb	Value of the Ambient Node's Index of Refraction.

'Line 35:',tp

'Line 35:',37.0

tp	Initial Temperature of System.

'Line 36:',lnum,dn,bmi

'Line 36:',0,0

dn	Initial Value for the Active Layer Concentration.
bmi	Initial Value for the Excited State Population.

'Line 37:',nytypeszs,jdir

'Line 37:',0,1,

nytypeszs	Computation Type for Z-Scan Analysis: 0 = All Rays at One Time, 1 = One Ray at a Time.
jdir	Parameter Not Used.

The following parameters describe a far-field computation of the Gaussian beam performed as a separate post-processor analysis. This was used to initially set up the parameters of the Gaussian Beam. Considerations were taken toward defining the power in the beam such that solutions were possible in the far-field.

'Line 38:',za,ra,rbm

'Line 38:',0.25,3.979e-2

za	Distance From the Focal Plane of the Input Beam to a Detector Aperture. Parameter Not Used for this Research.
ra	Radius of the Detector Aperture. Parameter Not Used for this Research.
rbm	Beam Radius at Detector Aperture. Parameter Not Used for this Research.

'Line 39:',nra,nsp,nfl

'Line 39:',30,20,1

nra	Number of Radial Divisions of the Detector Aperture.
nsp	Number of Terms in the Gaussian Decomposition.
nfl	Number of Files to be Read.

'Line 40:',sa

'Line 40:',1.0

sa	Aperture Size Normalization Parameter.

'Line 41:',tmelt,cfrc,cfk,cfe,rkset,hfsn

'Line 41:',90000.,1.0,1.0,1.0,0.03,1.0

tmelt	Melting Temperature of the System. A Pre-Defined Cut-Off Temperature Value in K.
cfrc	Ratio of Liquid to Solid Product of Specific Heat Times Density.
cfk	Ratio of Liquid to Solid Thermal Conductivity.
cfe	Ratio of Liquid to Solid Index of Refraction.
rkset	Sets a "No Change" to Thermal Conductivity.
hfsn	Heat of Fusion.

Bibliography

[1] I. Eliyahu and C.A. DiMarzio. Opto-photo-thermo-elastic displacement detection using coherent confocal microscope. *Proceedings of SPIE*, 7177, 717729:1–12, 2009.

[2] Jason M. Kellicker, Gregory J. Kowalski, and Charles A. DiMarzio. Computational Model of Photothermal Microscopy in Tissue. Publication pending, 2010.

[3] Igal Eliyahu. Opto-Phote-Thermo-Elastic Displacement Detection, Using Coherent Confocal Microscope. Master's thesis, Northeastern University, 2009.

[4] Alexander G. Bell. Upon the production of sound by radiant energy. *Journal of Science*, 1880.

[5] X. Wang, Y. Pang, G. Ku, X. Xie, G. Stoica, and LV Wang. Non-invasive laser-induced photoacoustic tomography for structural and functional imaging of the brain *in vivo*. *Nat. Biotechnol*, 21(7):803–806, 2003.

[6] Charles A. DiMarzio. *Optics for Engineers*. CRC Press, 2010. In Press.

[7] William C. Warger, Charles A. DiMarzio, and Milind Rajadhyaksha. Confocal microscopy. In David A. Boas, Constantinos Pitris, and Nimmi Ramanujam,

editors, *Handbook of Biomedical Optics*. CRC Press, Boca Raton, FL, Publication Pending.

[8] M. Minsky. Microscopy Apparatus, 1957. United States Patent 3013467.

[9] R.H. Webb. Confocal optical microscopy. *Reports on Progress in Physics*, 59:427, 1996.

[10] M. Rajadhyaksha, S. González, J.M. Zavislan, R.R. Anderson, and R.H. Webb. In Vivo Confocal Scanning Laser Microscopy of Human Skin II: Advances in Instrumentation and Comparison With Histology1. *Journal of Investigative Dermatology*, 113(3):293–303, 1999.

[11] P.J. Dwyer, C.A. DiMarzio, J.M. Zavislan, W.J. Fox, and M. Rajadhyaksha. Confocal reflectance theta line scanning microscope for imaging human skin in vivo. *Optics letters*, 31(7):942–944, 2006.

[12] P.J. Dwyer, C.A. DiMarzio, and M. Rajadhyaksha. Confocal theta line-scanning microscope for imaging human tissues. *microscope*, 18:20, 2007.

[13] Ludwig Mach. Uber einen Interferenzrefraktor. *Z. Instrumentenkunde*, 12:89–93, 1892.

[14] Ludwig Zehnder. Ein neuer Interferenzrefraktor. *Z. Instrumentenkunde*, 11:275–285, 1891.

[15] B.P. Payne, V. Venugopalan, B.B. Mikić, and N.S. Nishioka. Optoacoustic tomography using time-resolved interferometric detection of surface displacement. *Journal of Biomedical Optics*, 8:273, 2003.

[16] A. Nieva, M. Bouchard, and C.A. DiMarzio. Opto-acoustic signal detection with a coherent confocal microscope setup. In *Proceedings of SPIE*, volume 5697, page 313, 2005.

[17] G.J. Kowalski, E.H. Wahl, and J.F. Roach. Numerical Simulation of Thermal Effects in Nonlinear Optical Materials. In *MATERIALS RESEARCH SOCIETY SYMPOSIUM PROCEEDINGS*, volume 374, pages 15–32. MATERIALS RESEARCH SOCIETY, 1995.

[18] G.J. Kowalski. Numerical simulation of transient thermoreflectance of thin films in the picosecond regime. In *Proceedings of SPIE*, volume 2855, pages 138–146, 1996.

[19] G.J. Kowalski and R.A. Whalen. Microscale heat transfer effects under high incident heat flux conditions. *Proceedings of SPIE*, 3151:18–26, 2009.

[20] G.J. Kowalski and R.A. Whalen. Numerical simulation of a saturable absorbing material in the femtosecond regime. In *Proceedings of SPIE*, volume 3146, pages 81–89, 1997.

[21] Edward Harmon Wahl. Modeling of Thermal Effects on Nonlinear Optical Media. Master's thesis, Northeastern University, 1992.

[22] Richard A. Whalen. *Numerical Modeling of Microscale Heat Transfer Effects in Thermally Stimulated Nonlinear Optical Media.* PhD thesis, Northeastern University, 1999.

[23] G.J. Kowalski. Development of a Unified NLSRM Algorithm. Final Report, 1999.

[24] D.D. Joseph and L. Preziosi. Heat waves. *Reviews of Modern Physics*, 61(1):41–73, 1989.

[25] M. Sheik-Bahae, A.A. Said, T.H. Wei, D.J. Hagan, and EW Van Stryland. Sensitive measurement of optical nonlinearities using a single beam. *IEEE Journal of Quantum Electronics*, 26(4):760–769, 1990.

[26] G. Chen and CL Tien. Internal reflection effects on transient photothermal reflectance. *Journal of Applied Physics*, 73:3461, 1993.

[27] C.A. Paddock and G.L. Eesley. Transient thermoreflectance from metal films. *Optics letters*, 11(5):273, 1986.

[28] TQ Qiu and CL Tien. Heat transfer mechanisms during short-pulse laser heating of metals. *Journal of heat transfer*, 115(4):835–841, 1993.

[29] C.A. Balanis. *Advanced engineering electromagnetics.* Wiley, 1989.

[30] T.L. Troy and S.N. Thennadil. Optical properties of human skin in the near infrared wavelength range of 1000 to 2200 nm. *Journal of Biomedical Optics*, 6:167, 2001.

[31] A. Roggan, M. Friebel, K. Dörschel, A. Hahn, and G. Müller. Optical properties of circulating human blood in the wavelength range 400–2500 nm. *Journal of biomedical optics*, 4:36, 1999.

[32] W.F. Cheong, S.A. Prahl, and A.J. Welch. A review of the optical properties of biological tissues. *IEEE journal of quantum electronics*, 26(12):2166–2185, 1990.

[33] Engineer's Toolbox. Hooke's Stress and Strain Calculation. ETBX, 2008.

[34] Y.P Zheng and Arthur F.T. Mak. Extraction of Effective Young's Modulus of Skin and Subcutaneous Tissues from Manual Indentation Data. *IEEE Proceedings*, 19:2246–2249, 1997.

[35] PG Agache, C. Monneur, JL Leveque, and J. Rigal. Mechanical properties and Young's modulus of human skin in vivo. *Archives of Dermatological Research*, 269(3):221–232, 1980.

[36] WC Hayes, LM Keer, G. Herrmann, and LF Mockros. A mathematical analysis for indentation tests of articular cartilage. *Journal of biomechanics*, 5(5):541–551, 1972.

[37] A.P.C. Choi and YP Zheng. Estimation of Young's modulus and Poisson's ratio of soft tissue from indentation using two different-sized indentors: finite element analysis of the finite deformation effect. *Medical and Biological Engineering and Computing*, 43(2):258–264, 2005.

[38] S. Balocco, O. Basset, G. Courbebaisse, E. Boni, P. Tortoli, and C. Cachard. Noninvasive Young's modulus evaluation of tissues surrounding pulsatile vessels using ultrasound doppler measurement. *IEEE Transactions on Ultrasonics, Ferroelectrics and Frequency Control*, 54(6):1265–1271, 2007.

[39] ML Palmeri, AC Sharma, RR Bouchard, RW Nightingale, and KR Nightingale. A finite-element method model of soft tissue response to impulsive acoustic radiation force. *IEEE Transactions on Ultrasonics, Ferroelectrics and Frequency Control*, 52(10):1699–1712, 2005.

[40] G.J. Kowalski. Application of the NLSRM Algorithm as a Design Tool. Final Report, 1999.

[41] Timonshenko S.P. and J.N. Goodier. *Theory of Elasticity*. McGraw-Hill, 1970.

[42] II Warger, C. William, and C.A. DiMarzio. Computational signal-to-noise ratio analysis for optical quadrature microscopy. *Optics Express*, 17(4):2400–2422, 2009.

[43] D.O. Hogenboom and C.A. DiMarzio. Quadrature detection of a Doppler signal. *Applied optics*, 37(13):2569–2572, 1998.

[44] Christian Doppler. Uber das farbige Licht der Doppelsterne und einiger anderer Gestirne des Himmels: Abn. konigl. bohm. *Borrosch & Andre*, 2:465–482, 1842.

[45] C.A. DiMarzio and S.C. Lindberg. Signal-to-noise-ratio equations for a heterodyne laser radar. *Applied Optics*, 31(21):4240–4246, 1992.

[46] Laser Institute of America. *ANSI Standard Z136.1 (2007) American National Standard for the Safe Use of Lasers*, 2007.